2023

Optimal Design of Special High Torque Density Electric Machines based on Electromagnetic FEA

Murat G. Kesgin
University of Kentucky, kesgin.mrt@gmail.com
Digital Object Identifier: https://doi.org/10.13023/etd.2023.190

Recommended Citation

Kesgin, Murat G., "Optimal Design of Special High Torque Density Electric Machines based on Electromagnetic FEA" (2023). *Theses and Dissertations--Electrical and Computer Engineering*. 193.
https://uknowledge.uky.edu/ece_etds/193

STUDENT AGREEMENT:

I represent that my thesis or dissertation and abstract are my original work. Proper attribution has been given to all outside sources. I understand that I am solely responsible for obtaining any needed copyright permissions. I have obtained needed written permission statement(s) from the owner(s) of each third-party copyrighted matter to be included in my work, allowing electronic distribution (if such use is not permitted by the fair use doctrine) which will be submitted to UKnowledge as Additional File.

I hereby grant to The University of Kentucky and its agents the irrevocable, non-exclusive, and royalty-free license to archive and make accessible my work in whole or in part in all forms of media, now or hereafter known. I agree that the document mentioned above may be made available immediately for worldwide access unless an embargo applies.

I retain all other ownership rights to the copyright of my work. I also retain the right to use in future works (such as articles or books) all or part of my work. I understand that I am free to register the copyright to my work.

REVIEW, APPROVAL AND ACCEPTANCE

The document mentioned above has been reviewed and accepted by the student’s advisor, on behalf of the advisory committee, and by the Director of Graduate Studies (DGS), on behalf of the program; we verify that this is the final, approved version of the student’s thesis including all changes required by the advisory committee. The undersigned agree to abide by the statements above.

Murat G. Kesgin, Student

Dr. Dan M. Ionel, Major Professor

Dr. Daniel L. Lau, Director of Graduate Studies

Optimal Design of Special High Torque Density Electric Machines based on Electromagnetic FEA

DISSERTATION

A dissertation submitted in partial fulfillment of the requirements for the
degree of Doctor of Philosophy in the College of Engineering at the
University of Kentucky

By

Murat Gurhan Kesgin

Lexington, Kentucky

Director: Dr. Dan M. Ionel, Professor and L. Stanley Pigman Chair in Power

Lexington, Kentucky 2023

ABSTRACT OF DISSERTATION

OPTIMAL DESIGN OF SPECIAL HIGH TORQUE DENSITY ELECTRIC MACHINES BASED ON ELECTROMAGNETIC FEA

Electric machines with high torque density are essential for many low-speed direct-drive systems, such as wind turbines, electric vehicles, and industrial automation. Permanent magnet (PM) machines that incorporate a magnetic gearing effect are particularly useful for these applications due to their potential for achieving extremely high torque density. However, when the number of rotor polarities is increased, there is a corresponding need to increase the number of stator slots and coils proportionally. This can result in manufacturing challenges. A new topology of an axial-flux vernier-type machine of MAGNUS type has been presented to address the mentioned limitation. These machines can attain high electrical frequency using only a few stator coils and teeth, which can simplify construction and manufacturing under certain conditions. Additionally, the inclusion of auxiliary small teeth within the stator main teeth can generate a noteworthy increase in output torque, making it a unique characteristic of this motor. By analyzing the operating principle of the proposed VTFM PM machine, possible pole-slot combinations have been derived. The process of designing an electric machine is complicated and involves several variables and factors that must be balanced by the designer, such as efficiency, cost, and performance requirements. To achieve a successful design, it is crucial to employ multi-objective optimization. Using a 3D FEA model can consider the impact of magnetic saturation, leakage flux, and end effects, which are not accounted for in 2D. Optimization using a 3D parametric model can offer a more precise analysis. Validating the machine's performance requires prototyping a model and testing it under different operating conditions, such as speed and load, which is a crucial step. This approach provides valuable insights into the machine's behavior, allowing the identification of any areas for improvement or weaknesses. A large-scale multi-objective optimization study has been conducted for an axial-flux vernier-type PM machine with 3-dimensional (3D) finite element analysis (FEA) to minimize the material cost and maximize the electromagnetic efficiency. A detailed study for torque contribution has indicated that auxiliary teeth on each stator main teeth amplify net torque production. A prototype of optimal design has been built and tested.

KEYWORDS: Axial flux permanent magnet, electric machines, high-torque density, optimization, 3D finite element analysis, high-power density, prototyping.

Author's signature: Murat G. Kesgin

Date: May 8, 2023

Optimal Design of Special High Torque Density Electric Machines based on Electromagnetic FEA

By
Murat Gurhan Kesgin

Director of Thesis: Dr. Dan M. Ionel

Director of Graduate Studies: Dr. Daniel L. Lau

Date: May 8, 2023

To Bedia and Mustafa...

ACKNOWLEDGEMENTS

First and foremost, I would like to extend my heartfelt gratitude to my Ph.D. supervisor, Professor Dan M. Ionel, Ph.D., FIEEE, L. Stanley Pigman Chair in Power, for his immense knowledge, unwavering encouragement and support, which have enabled me to pursue my goals since I became a member of the SPARK Laboratory in the ECE Department at the University of Kentucky. I am deeply grateful to him for placing his trust in me and encouraging me to strive for further progress and accomplishments. Under his mentorship, I gained valuable experience working both independently and as a member and leader of a team. I learned the importance of remaining receptive to a constantly evolving world and being prepared to embrace novel ideas. Through his guidance, I also gained an understanding of the crucial role that coordination and communication play in achieving success. I am appreciative of his continuous guidance, planning, discussions, and review throughout every phase of my research and dissertation. I am immensely thankful to Professor Ionel for establishing the SPARK group with a welcoming and supportive atmosphere.

I would also like to express my sincere thanks to all my professors, and especially to my Ph.D. Committee members, Professors Yuan Liao, Cai-Cheng Lu, Joseph Sottile, and external examiner Professor Sean C. Bailey.

I am grateful to my postdoctoral mentors, Dr. Vandana Rallabandi and Dr. Peng Han, for their exceptional guidance and mentorship, which have greatly contributed to my development and progress. I would like to express my appreciation to all of my talented and dedicated colleagues in the SPARK Lab and postdoc Dr. Abdullah Al Hadi for their invaluable collaboration and friendship.

At ANSYS, Dr. Ping Zhou and Mr. Mark Solveson provided expert advice and technical insights for which I am very grateful. I am also very thankful to my mentors during my internship at Ansys Inc. namely, Dr. Bo He, Dr. Ozgur Tuncer, and the software R&D teams. I would like to express my appreciation to Dr. Madhav Manjrekar and Dr. Somasundaram Essakiappan at QM Power Inc. for sharing their knowledge and expertise

I express my gratitude for the support provided by The support of the National Science Foundation (NSF), award no. 1809876, and Vehicle Technologies Office, U.S. Department of Energy, under award no. DEEE0008871 is also gratefully acknowledged. My great appreciation is also due for the support over the years of Ansys Inc., QM Power Inc, University of Kentucky, and the L. Stanley Pigman endowment.

I am filled with profound gratitude towards my mother, Ayten and father, Bayram, as well as my brother, Fatih, and sister, Fazilet. Their unwavering encouragement, immense love, and constant support have been instrumental in helping me reach where I am today. Without their selfless sacrifices and ceaseless dedication, I could not have achieved my current level of success.

Last, but not least, my most special gratitude goes to my wife, Bedia, for accompanying me through my PhD years with her unwavering support, and love and for being an amazing mother to our son, Mustafa.

Murat G. Kesgin
April, 2023

Contents

List of Tables

List of Figures

Chapter 1 Introduction

1.1 Background

The global demand for electric energy has been increasing rapidly, with a significant proportion being consumed by electric machines used in various applications, such as electrified transportation systems, industrial automation, robotics, and air conditioners. Electric motor-driven systems consume 68% of the total electricity worldwide. In many parts of the world, environmental concerns regarding the use of fossil fuels to generate electricity have intensified the need to design electric motors that are more efficient. The trend towards the electrification of transportation is expected to further increase global energy consumption. The increasing numbers of electric vehicles and more electric aircraft being developed will also boost the energy consumption ratio of electric machines.

Apart from their operation, the manufacturing of electric machines also has an impact on the environment. The main components of electric machines are the winding, stator and rotor core, and possibly permanent magnets. Copper is usually the preferred material for the windings, while laminated steel is used for the cores. The use of magnets made of rare earth elements has become increasingly popular due to their high efficiency, power, and torque density. However, the increasing demand for these magnets in the electric vehicle industry and wind generators has led to concerns regarding material costs. This has prompted researchers to focus mainly on the following topics in the electric machine design process:

- Developing new machine topologies to meet diverse application requirements.
- Improving the material properties of laminated steels, permanent magnets (PMs), insulation materials, and conductors.
- Conducting systematic design optimization and comparisons of electric machines.
- Performing multi-physics analysis of electric machine and drive systems.

The electrification of transportation has garnered increasing attention over the past two decades. In addition to environmental concerns, fuel efficiency and lower cost per distance have led to increased popularity of electric vehicles. One of the main barriers to wider adoption of electric vehicles was their limited driving range, but this has been improved with enhanced battery technologies. Different types of electric motors are preferred in electric vehicles, such as DC motors, induction motors, permanent magnet brushless motors, and switched reluctance motors. Among these, permanent magnet synchronous machines have dominated the market due to their wide torque-speed range with high torque and power density.

Literature reviews *on specific topics are distributed throughout this dissertation and included in each chapter.*

1.2 Research Objectives and Original Contributions

Research Objectives

Electric machines with high torque density play a crucial role in various electromechanical systems, including wind turbines, electric vehicles, and industrial automation systems. In low-speed applications, high-polarity permanent magnet (PM) machines can increase torque density and efficiency by reducing the flux per pole linked by the stator winding. This reduction allows for the use of more compact magnetic parts and shorter end-turn volume. However, increasing the number of rotor polarities necessitates a proportional increase in the number of stator slots and coils, which can make manufacturing difficult.

To address this limitation, a new topology of an axial-flux vernier-type machine called the MAGNUS motor has been introduced in this study. These machines can achieve high electrical frequency with very few stator coils and teeth, simplifying construction and manufacturing under certain conditions. Additionally, the inclusion of auxiliary small teeth in the stator main teeth yields a significant increase in output torque, which is a unique feature of this motor. The analysis of the operating principle of the proposed VTFM PM machine can lead to the derivation of feasible pole-slot combinations.

Designing an electric machine is inherently complex, with many factors and variables. And a designer must balance the competing factors of efficiency and cost along with performance requirements. Multi-objective optimization is an absolute necessity for the successful design of electric machines. The use of 3D FEA model allows for the consideration of the effects of magnetic saturation, leakage flux, and end effects that are not accounted for in 2D. An optimization using a 3D parametric model can provide a more accurate analysis. Prototyping a model and testing it under different speed, load, and operating conditions is a crucial step to validate the performance of the machine. This approach can provide valuable insights into the behavior of the machine and help to identify any weaknesses or areas for improvement.

Original Contributions

The major contributions of the dissertation are summarized as:

- Developed a procedure of optimizing an electric machine based on finite element analyses and employing differential evolution. The method has been demonstrated on an axial flux permanent magnet machine (Chapter 2).

- The axial-flux vernier type machines of the MAGNUS type motor of new topology has been introduced. Its working principle has been analyzed and feasible slot-pole combinations for 2-phase and 3-phase versions have been established. Which these topologies demonstrate a high level of demagnetizing fault tolerance due to their lack of coupling between phases (Chapter 3).

- A new topology of an axial-flux vernier type machine of the MAGNUS type has been proposed, the operating principle has been analyzed, and feasible slot-pole combinations for 2-phase and 3-phase designs have been established. Designs of this type have a high level of fault tolerance to PM demagnetization due to the lack of coupling between phases. A detailed study for torque contribution has indicated that auxiliary teeth on each stator main teeth amplify net torque production (Chapter 3).

- For a MAGNUS machine, a large-scale multi-objective optimization study has been conducted with 3-dimensional (3D) finite element analysis (FEA) to minimize the material cost and maximize the electromagnetic efficiency. A prototype of optimal design has been built and tested (Chapter 3).
- A new topology of a double salient machine has been proposed to achieve high volumetric power density. Comprehensive design optimization at a large scale has been conducted with maximum efficiency and power factor. The optimal design can achieve the 50 kW/L target with advanced winding and cooling techniques. (Chapter 4)
- Comprehensive design optimization at a large scale has been conducted with maximum efficiency and power factor. The optimal design can achieve the 50 kW/L target with advanced winding and cooling techniques (Chapter 4).

1.3 Dissertation Outline

Following the introduction, Chapter 2 provides an overview of the development of electric machine processes, with a focus on sizing equations based on motor performance, finite element analysis (FEA), and optimization of electric machine. It also discusses the use of FEA to simulate and analyze electric machines, allowing designers to optimize their designs for better performance and efficiency. In Chapter 3, the focus shifts to the introduction of a new topology of axial-flux vernier type machine of MAGNUS type motor. This chapter establishes the working principle and feasible slot-pole combinations for 2-phase and 3-phase versions of the machine. It also presents a large-scale optimization study based on three-dimensional (3-D) finite element analysis (FEA) for a MAGNUS AF machine with two special stators and one spoke-type PM rotor. The chapter concludes with a discussion of the prototyping process for the MAGNUS motor. In Chapter 4, it is proposed a special double salient machine with a high volumetric power density of 50kW/L. The construction and operating principle of the machine, as well as its torque production mechanism based on the air-gap flux density waveforms, has been presented. The proposed double salient machine is designed to deliver higher torque and power across a wide speed range of up to 37,500 RPM. It offers several advantages, including topology suitable for enhanced direct coil cooling, modular manufacturing construction, winding with separated phase coils and inherent fault tolerance, high-speed operation capability, and a wide speed range with a constant power speed ratio of at least 3:1.

1.4 Publications

The main elements covered in this dissertation have been peer reviewed and published in:

- **Kesgin, M. G.**, Han, P., Lawhorn, D. L., and Ionel, D. M., “Analysis of Torque Production in Axial-flux Vernier PM Machines of the MAGNUS Type,” Proceedings, 2021 IEEE IEMDC, Hartford, CT, USA, 2021, pp. 1-5, doi: 10.1109/IEMDC47953.2021.9449556 (May 2021)
- **Kesgin, M. G.**, Han, P., Taran, N., Lawhorn, D., Lewis, D., and Ionel, D. M., ”Design Optimization of Coreless Axial-flux PM Machines with Litz Wire

and PCB Stator Windings," Proceedings, IEEE ECCE 2020, Detroit, MI, doi: 10.1109/ECCE44975.2020.9236194, pp. 22-26 (Oct 2020)

- **Kesgin, M. G.**, Han, P., Taran, N., and Ionel, D. M., "Optimal Study of a High Specific Torque Vernier-type Axial-flux PM Machine with Two Different Stators and a Single Winding," Proceedings, IEEE ECCE 2020, Detroit, MI, doi: 10.1109/ECCE44975.2020.9235901, pp. 4064-4067 (Oct 2020)

- **Kesgin, M. G.**, Han, P., Taran, N., and Ionel, D. M., "Overview of Flywheel Systems for Renewable Energy Storage with a Design Study for High-speed Axial-flux Permanent-magnet Machines," Proceedings, IEEE ICRERA 2019, Brasov, RO, doi: 10.1109/ICRERA47325.2019.8996526, pp. 1026-1031 (Nov 2019) – *Best Paper Award.*

- Han, P., **Kesgin, M. G.**, Ionel, D. M., Gosalia, R., Shah, N,. Flynn, C. J., Goli, C. S., Essakiappan, S., and Manjrekar, M. "Design Optimization of a Very High Power Density Motor with a Reluctance Rotor and a Modular Stator Having PMs and Toroidal Windings," Proceedings 2021 IEEE ECCE, Vancouver, BC, Canada, 2021, pp. 4424-4430, doi:10.1109/ECCE47101.2021.9595129 (Oct 2021).

- Rallabandi, V., Han, P., **Kesgin, M. G.**, Taran, N. and Ionel, D. M., "Axial-field Vernier-type Flux Modulation Machines for Low-speed Direct-drive Applications," Proceedings, IEEE ECCE 2019, Baltimore, MD, doi: 10.1109/ECCE.2019.8912550, pp. 3123-3128 (Oct 2019).

- *Goli, C. S.,* ***Kesgin, M. G.****, Han, P., Ionel, D. M., Essakiappan, S., Gafford, J., and Manjrekar, M., ”Equivalent Circuit and Loss Components for a Special Double Salient Machine Employing a Stator with Phase Winding Modules and PMs,” Prepared for Journal Submission (Mar 2023)*

Chapter 2 Combined Procedure of Design Sizing, Finite Element Analysis (FEA), and Optimization of Electric Machines

2.1 Introduction and Problem Formulation

To begin the design process, the design requirements must be clearly defined, including the desired motor performance, operating conditions, and any relevant constraints such as cost, size, and weight. Once the requirements are established, several design options are explored to identify the most promising candidates. The initial design procedures of electric machines typically involve using sizing equations. Sizing equations are mathematical formulas that relate the physical dimensions of the machine to its performance characteristics, such as torque, speed, and power output. These equations take into account the specific design requirements, such as the desired power output, the speed of operation, and the efficiency of the machine. While formulas and sizing equations can be useful for initial estimation and outcomes, they may not always lead to optimal results.

The design, analysis, and optimization of electric machines based on Finite Element Analysis (FEA) involve using computer software to simulate and analyze the behavior of the machine under various operating conditions. FEA is a powerful tool that enables engineers to design and optimize electric machines with a high degree of accuracy and precision. The first step in the FEA design process is to create a 3D model of the machine using computer-aided design (CAD) software. The CAD model is then imported into the FEA software, where the engineer defines the material properties, boundary conditions, and loads that will be applied to the machine during operation. FEA simulations can provide valuable insights into the behavior of electric machines, such as the magnetic flux density, the distribution of electromagnetic forces, and the temperature distribution within the machine. This information can be used to optimize the design of the machine, improving its performance, efficiency, and durability.

The development process of electric machines requires methodologies that are both effective and precise. While formulas, sizing equations, and experience can be useful for initial estimation and outcomes, they may not always lead to optimal results.

This chapter is divided into the design, analysis, and optimization procedures of two distinct types of electric machines. Through a comprehensive investigation of these machines, this chapter aims to provide insights into the complexities and nuances of optimizing electric machine performance and the critical role of design and analysis in achieving these objectives. A brief review of FEA for low frequency electromagnetics and of electric machine application specifics is also included.

This chapter is substantially based on the following papers:

- M. G. Kesgin *et al.*, "Design Optimization of Coreless Axial-flux PM Machines with Litz Wire and PCB Stator Windings," Proceedings, IEEE ECCE 2020, Detroit, MI, doi: 10.1109/ECCE44975.2020.9236194, pp. 22-26 (Oct 2020)

- M. G. Kesgin *et al.*, ”Overview of Flywheel Systems for Renewable Energy Storage with a Design Study for High-speed Axial-flux Permanent-magnet Machines,” Proceedings, IEEE ICRERA 2019, Brasov, RO, doi: 10.1109/ICRERA47325.2019.8996526, pp. 1026-1031 (Nov 2019

2.2 Literature Review

The flywheel system is employed to store and release energy. Recent technological developments have spawned the growth of renewable energy resources, such as solar and wind power. The intermittent nature of these resources may introduce issues with system stability, reliability and power quality. Storing power from these intermittent sources with energy storage systems partially decouples the energy generation from demand and is thus considered as an effective approach to addressing problems introduced by the penetration of renewable energies [1], [2]. Interests in energy storage have seen rapid growth recently and the renewable energy industry is expected to generate a larger proportion of the overall energy consumption in the near future.

Energy can be stored through various forms, such as ultracapacitors, electrochemical batteries, kinetic flywheels, hydroelectric power or compressed air. Their comparison in terms of specific power, specific energy, cycle life, self-discharge rate and efficiency can be found, for example, in [3]. Compared with other energy storage methods, notably chemical batteries, the flywheel energy storage has much higher power density but lower energy density, longer life cycles and comparable efficiency, which is mostly attractive for short-term energy storage.

The second example of electric machine design and development for coreless axial-flux permanent-magnet (AFPM) machine. This machines typically employ a special disk-type construction with a stator, which does not have a ferromagnetic core, positioned in between two rotors that ensure the magnetic return path. As a consequence, these machines may be, in principle, lighter and more efficient, because the stator core losses are eliminated [4]. Designs of coreless AFPM have been recently proposed and studied by the authors' extended research group [5–8] and by others, e.g. [9–11].

Because in a coreless machine the windings are directly exposed to the time-varying main magnetic field the eddy current losses in the stator conductors may be significant and special mitigation measures are required [12, 13]. Such constructive techniques include the use of special Litz wires, especially if the machines operate at high frequency [8, 14, 15].

An alternative approach is to employ printed circuit boards (PCBs) for the stator, such that copper traces serve as planar winding conductors between layers of laminated material. PCB stators have been reported as being compact, flexible, suitable for design modifications and accurate manufacturing techniques [16], and with good capabilities for heat dissipation [17]. A prototype motor for low-cost household applications was designed with a PCB stator employing a wave winding pattern and described in [16]. A non-overlapping concentrated winding with hexagonal concentric shapes was utilized in the PCB stator proposed in [17].

2.3 Axial Flux Electric Machines and Sizing Procedures

This stage may involve conducting preliminary research to gain a better understanding of the problem and its constraints, as well as identifying the key parameters and specifications of the product or system. During the design of an electric machine, mathematical equations such as sizing equations and loss estimation can be applied to help determine the appropriate specifications and design parameters of the machine.

2.3.1 Flywheel energy storage systems (FESS) and associated electric machines

Configurations and principle of operation

A typical FESS, as shown in Fig.2.1, includes a flywheel rotor, an electric motor/generator and its associated drive, bearing systems, and a containment. The flywheel rotor is a moving mass that stores the kinetic energy. The machine and drive work in three modes of operation, i.e., charging, standby and discharging, and perform the energy conversion, as illustrated in Fig. 2.2. During the charging mode, the machine works as a motor and accelerates the flywheel, while in discharging mode, the machine serves as a generator and extracts the stored energy to supply the load.

Flywheel energy storage systems (FESS) have been used in uninterrupted power supply (UPS) [18–20], brake energy recovery for racing cars [21], public transportation [22], off-highway vehicles [23], container cranes/straddle carriers [24], and grids [25–27]. They were also proposed to be used in the pulse power supply for electromagnetic launch systems [28]. Major manufacturers of FESS are tabulated in Table 2.1, focusing on UPS, brake energy recovery, and grid.

Table 2.1: Major manufacturers of FESS and their applications

Manufacturer	Ratings	Applications
ABB	1,800-3,600 rpm, 100-1,500 kW	Renewable microgrid stabilization [25]
Active Power	Max. 10,000 rpm, 225 kW	UPS [18]
Beacon Power, LLC	Max. 16,000 rpm, 100 kW	Utility grid [27]
Calnetix Technologies, LLC	25,000-35,000 rpm, 125 kW	UPS [19]
Williams Hybrid Power	Max. 36,000-45,000 rpm, 150-180 kW	Brake energy recovery for vehicles [21]
Kinetic Traction Systems	Max. 36,000 rpm, 250-400 kVA	Brake energy recovery, UPS and grid [29]
PowerThru	–	UPS [20]
PUNCH Flybrid	Max. 60,000 rpm, 60 kW	Brake energy recovery for vehicles [23]
Ricardo PLC	Max. 44,000 rpm, 100 kW	Brake energy recovery for vehicles [30]
Temporal Power	–	Utility grid [31]

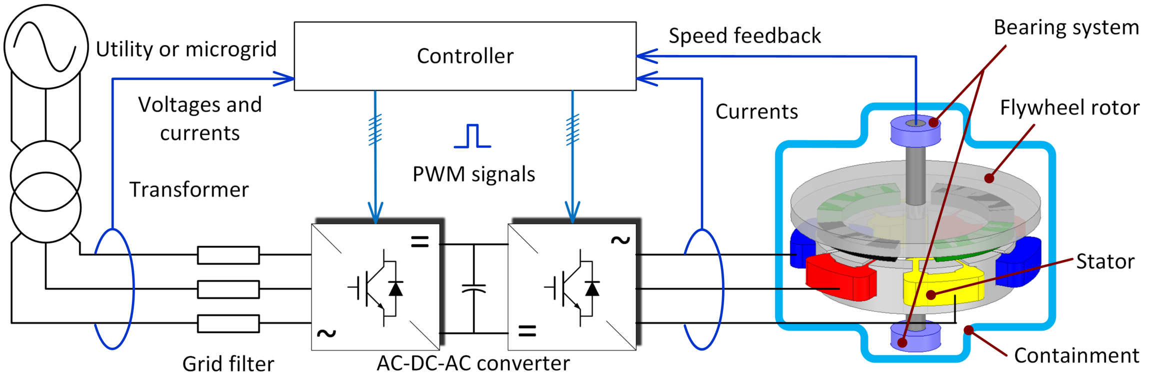

Figure 2.1: A typical FESS with a solid flywheel rotor. A transparent view of the rotor back iron is employed in order to show PMs and stator coils.

Bearings are used to keep the flywheel rotor in place with very low friction. They can be mechanical, magnetic or hybrid. Active and/or passive magnetic bearings are usually employed to hold the flywheel during operation, ensuring a long life, reduced losses and low maintenance [32]. The high-temperature superconducting (HTS) type has also been proposed to levitate and rotate the flywheel [33]. Mechanical types may also be included to hold the flywheel while it is stationary or below operational speed. Additional catch bearings may be installed to provide a fail-safe system. The containment not only provides an environment with low aerodynamic drag, but also shields the fragments in the event of rotor failures.

Sizing procedure for flywheel rotors

In this section, sizing equations will be investigated. The electrical and magnetic loads can be roughly determined based on preliminary layout and approximate motor component dimensions, such as stack length, rotor diameter, etc. This procedure is helpful to conjecture possible performance of an electric machine. Type of materials for motor parts (magnet type, stator and rotor core) are considered in this stage.

Flywheel rotors are built as solid or hollow cylinders. The maximum kinetic energy stored in the flywheel E_k is:

$$E_k = \frac{1}{2} J \omega^2, \tag{2.1}$$

where ω_{max} is the maximum angular velocity, J is the moment of inertia, which is a function of the mass and shape of the rotor, and for hollow cylinders, it can be expressed as:

$$J = \frac{1}{2} m \left({r_o}^2 + {r_i}^2 \right) = \frac{\rho \pi h}{2} \left(r_o^4 - r_i^4 \right), \tag{2.2}$$

where m is the flywheel rotor mass and ρ the mass density, r_o and r_i are the outer radius and inner radius of a hollow cylinder flywheel, respectively, h is the thickness of the flywheel rotor in axial direction. The useful energy of a flywheel within a speed range of minimum speed ω_{min} and maximum speed ω_{max} can be obtained by:

$$E_{keff} = \frac{1}{2} J \left(\omega_{max}^2 - \omega_{min}^2 \right) = \frac{1}{2} J \omega_{max}^2 \left(1 - \frac{\omega_{min}^2}{\omega_{max}^2} \right), \tag{2.3}$$

The ratio $\omega_{min}/\omega_{max}$ depends on the voltage variation and maximum torque for a given power rating. The peak torque occurs at the lowest speed in discharging mode, as shown in Fig. 2.2. A typical value for $\omega_{min}/\omega_{max}$ is 0.5, in which case, 75% of the total stored energy can be extracted from the flywheel. The selection of this value also has an impact on the life cycle [34].

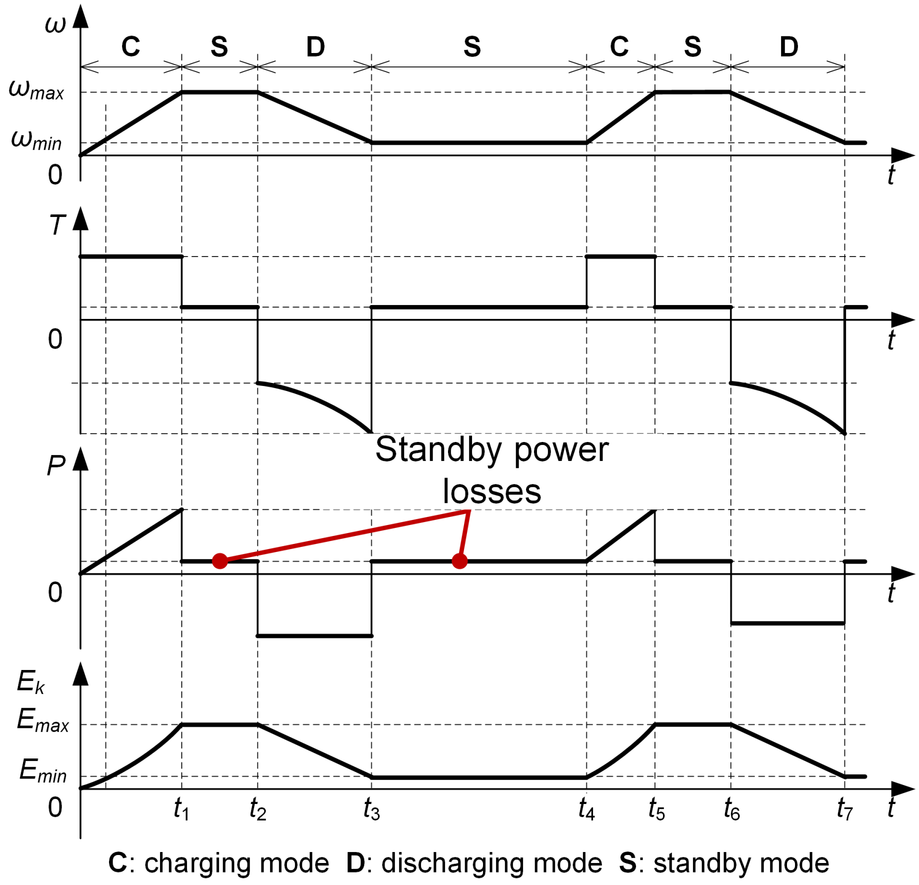

Figure 2.2: Typical operating cycles for FESS. The power rating is limited by the lowest speed in discharging mode, where the maximum torque occurs. The standby power losses are shown disproportionately for illustration purposes.

The outer radius is limited by the yield stress of the material σ_y, external stress σ_{sh} introduced by the shrink-fit between the flywheel rotor and shaft, Poisson's ratio υ and the maximum rotating speed of the flywheel ω_{max}:

$$r_o < \sqrt{\frac{4\left(\sigma_y - \sigma_{sh}\right)}{\left(3+\upsilon\right)\rho\omega_{max}^2} - \frac{1-\upsilon}{3+\upsilon} r_i^2}, \tag{2.4}$$

The thickness in the axial direction can then be estimated by:

$$h = \frac{4E_k}{\rho\pi{\omega_{max}}^2\left(r_o^4 - r_i^4\right)}. \tag{2.5}$$

Based on (2.4) and (2.5), the maximum specific energy is:

$$\frac{E_k}{m} = K\frac{\sigma_y}{\rho}, \tag{2.6}$$

where K is the shape factor of the hollow cylinder flywheel with isotropic material, such as steel:

$$K = \frac{\left(1 - \frac{\sigma_{sh}}{\sigma_y}\right)\left[\left(\frac{r_i}{r_o}\right)^2 + 1\right]}{\left[\left(1-\upsilon\right)\left(\frac{r_i}{r_o}\right)^2 + \left(3+\upsilon\right)\right]}. \tag{2.7}$$

The shape factor K is a measurement of material utilization and depends on the flywheel geometry, as summarized in [35]. Considering ease of manufacturing and assembling, conventional flywheel rotors are hollow cylinders with central holes to install the shaft, which are used to couple the electric motor/generator.

Equation (2.6) indicates that the specific energy (energy per mass unit) and energy density (energy per volume unit) of the flywheel are dependent on its shape, expressed by the shape factor K, and the yield stress σ_y. By contrast, the power rating depends on the motor/generator characteristics. This means the energy and power rating can be sized independently, depending on the application requirements. This flexibility is a particularly advantageous feature of flywheel technology.

Table 2.2: Flywheel material characteristics.

Material	ρ (kg/m^3)	σ_y (MPa)	σ_f (MPa)	E_k/V (kWh/m^3)	E_k/m (Wh/kg)
Steel - wrought	7,800	950	550	46.6	6.0
Steel - maraging	8,000	2,337	765	64.8	8.1
Titanium	4,500	1,186	662	56.1	12.4
Fiber - glass	2,000	1,100	220	30.0	15.0
Fiber - aramid	1,400	1,400	700	97.0	69.0
Fiber - Carbon	1,550	2,000	1,600	222.0	143.0

To achieve high-specific-energy flywheels, strong materials with low mass densities are typically needed for the flywheel rotors as listed in Table 2.2 based on data from [35]. The fatigue strength for a cycle life of 10^7 cycles σ_f instead of the yield strength is used to give more practical estimations about the energy density and specific energy. The calculation of E_k/m and E_k/V for hollow cylindrical flywheels made of metal uses $K = 0.305$ and $K = 0.500$ is used for flywheels made of filamentary composites.

Performance metrics

Uniform parameters and evaluation methods have been defined by the Pacific Northwest National Laboratory (PNNL) and Sandia national Laboratories (SNL) to serve as the basis to compare the performance of different energy storage systems. The definitions are applicable to various energy storage methods but not all of them are of special interest to a specific storage method. In this section, only metrics essential to FESS are presented. Table 2.3 lists the statistical results of published FESS in terms of these performance. The definitions of depth of discharge, round-trip efficiency and standby power losses are presented below. The details related to other performance

Table 2.3: Published metrics of FESS. Statistical results from multiple sources.

Metric	Value
Power rating (MW)	0.001-10
Specific energy (Wh/kg)	5-200
Specific power (W/kg)	400-30,000
Energy density (kWh/m^3)	0.25-424
Power density (kW/m^3)	40-2,000
Round-trip efficiency (%)	70-96
Calendar life (year)	15-20
Cycle life (cycles)	10,000-100,000
Self-discharge rate (%/day)	24-100

metrics can be found in [36].

The depth of discharge is the percentage of flywheel energy capacity that has been discharged, expressed as a percentage of the maximum capacity. The depth of discharge of flywheels is up to the output power and the maximum current of the power converter. The round-trip efficiency is expressed as a percentage of the useful output energy with respect to the input energy over one duty cycle under normal conditions. The time period from t_3 to t_7 in Fig. 2.2 is a typical operating cycle. Round-trip efficiency is a pivotal design factor especially for long-term FESS. Nowadays, the round-trip efficiency of FESS can reach 80%-95%. The key metrics of FESS listed in Table 2.3 are based on data compiled from [18–21, 23, 25, 27, 29–31, 37].

The standby power losses are loss components that gradually reduce the stored energy in the standby mode of operation. The standby power losses depend on the design of flywheels and are usually caused by friction, aerodynamic drag and open-circuit motor/generator losses that slow down the rotor. To reduce the standby power losses, vacuum containment and magnetic bearings are usually employed [38, 39]. The standby losses are designed to be very low, typically less than 25 W/kWh of the stored energy and in the range of 1-2% of the rated output power.

Electric machine topologies for FESS, research and development trends

PM brushless machines and squirrel-cage induction machines of the radial-flux type have been widely used in FESS. Radial-flux and transverse-flux homopolar induction machines have drawn much attention during the past two decades considering their low-standby-loss nature and the ease of integrating the electric machine rotor with the flywheel [40–42]. However, the torque/power density of this type is relatively low compared with induction machines and PM brushless machines [43]. Other machines, such as synchronous reluctance machines, and bearingless versions of PM brushless machines and induction machines have also been proposed, yet experimental demonstrations of the feasibility are still rare.

The research in electric machines for FESS mainly focuses on the reduction of standby power losses. The use of magnetic or HTS bearings and installing the flywheel in low-pressure containments are effective ways to achieve the goal. Flywheel energy storage tends to use various active/passive magnetic and HTS bearings to reduce the losses caused by friction as well as extend the lifetime for maintenance-free operation. Retractable configurations, i.e., adjustable airgaps [44], [45], and slotless or coreless structures [46] have also been used to reduce the standby power losses. The heat dissipation and thermal analysis of electric machines are of significance if the motor/generators are included in the low-pressure containments considering the very low convective heat transfer in such conditions.

Axial flux permanent magnet (AFPM) machines

AFPM brushless machines have also been proposed for FESS. An AFPM machine in a vertical arrangement with two stators and one central rotor has been presented to improve the round-trip efficiency by making full use of the axial forces instead of active/passive bearings in [47]. The central rotor serves as the flywheel of the integrated system and the magnetic attractions between the rotor and stators were controlled appropriately to counteract the rotor gravity. A flywheel system with an axial-flux motor/generator whose airgap can be adjusted dynamically to reduce the standby power losses during idle periods has also been proposed [45]. A micro-flywheel energy storage with an AFPM machine and HTS bearing was fabricated and tested in [48]. The disk-type aluminum rotor with high moment of inertia was used as the flywheel rotor and the maximum speed reached 51,000 rpm.

2.3.2 Special coreless AFPMs with Litz wire and PCB stator windings

Coreless AFPM machines are usually constructed using a special disk-shaped design that incorporates a stator without a ferromagnetic core. The stator is positioned between two rotors that serve to complete the magnetic return path.

In this section, three coreless AFPM machines are considered for study (Fig. 2.3). Two-phase wave windings are used in the two machines shown in Fig. 2.3a and Fig. 2.3b to reduce the number of wire joints. Two-phase windings are advantageous in terms of balance. The minimization of the mutual coupling provides better fault

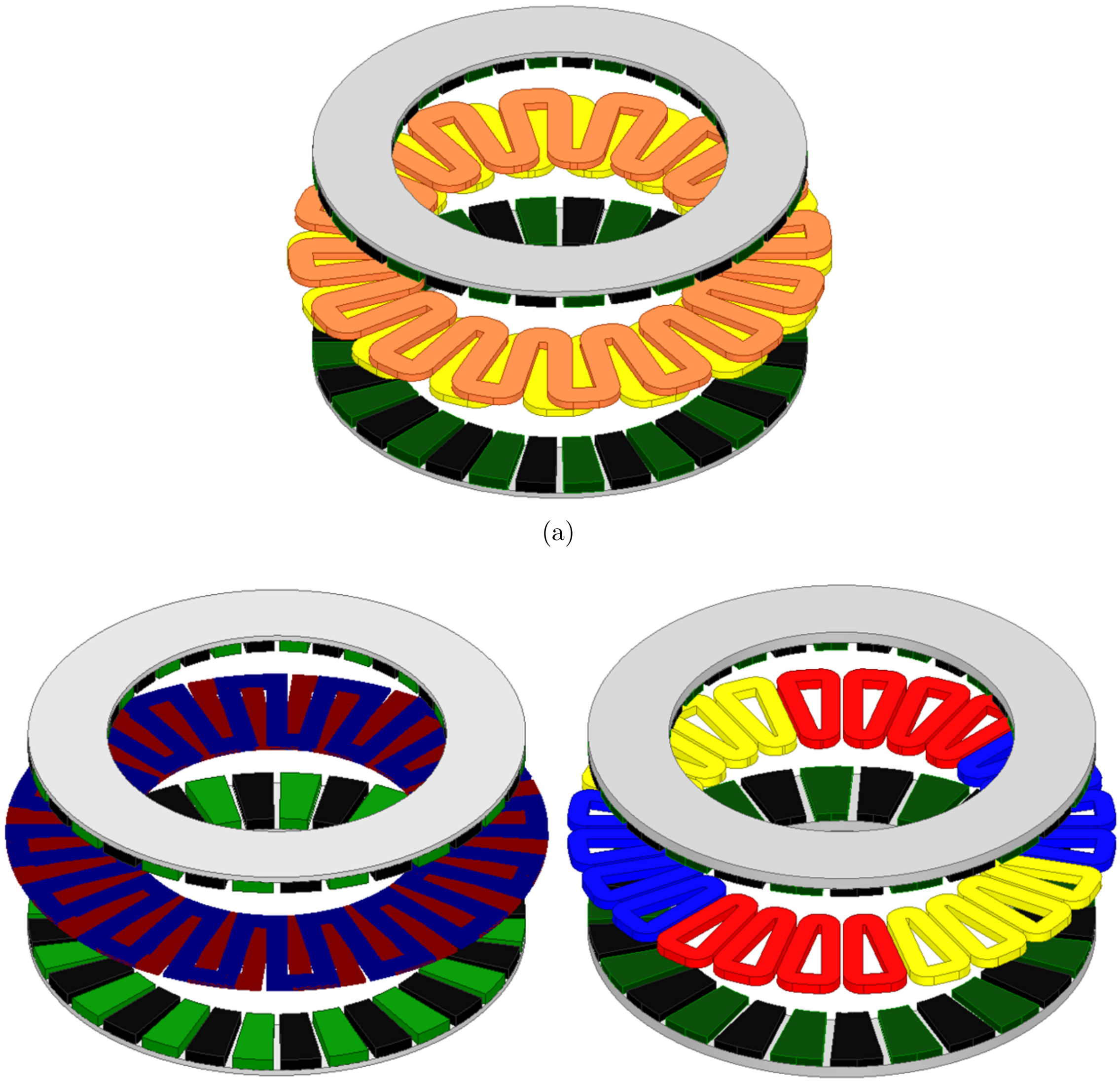

(a)

(b)

(c)

Figure 2.3: Exploded views of coreless AFPM machines under study: (a) 2-phase AFPM with wave windings wound with Litz wires, (b) 2-phase AFPM with PCB wave windings, (c) 3-phase AFPM with fractional-slot concentrated windings.

tolerance. The third machine employs a special fractional-slot concentrated winding configuration, which is suitable to be fabricated with modular coil groups. All the machines are required to produce 12 Nm up to a speed of 3,000 r/min.

The higher the operating frequency is, the smaller the nominal single wire diameter has to be. To consider the interaction between several bundle diameters with skin depth, δ, in a simplified way, the maximum single wire diameter is recommended to be smaller or equal to nearly $\delta/3$ [49].

The efficiency of coreless machines with PCB stators is heavily dependent on cross-sectional area of the copper traces. Reducing the conductor's height or width increases the dc copper loss due to lower current carrying capacity unless the number of tracks (turns) increases. Outside of a typical range, available copper trace height differs from manufacturer to manufacturer. The minimal copper trace width is limited by the precision of machines used in current manufacturing practices. However, the number of traces can be increased axially by stacking and connecting more PCBs, creating more layers in the PCB, or by reducing the conductor width to allow for more traces on the same plane. Since higher numbers of printed boards increases the electromagnetic airgap, ideally, more traces should be placed on each single board.

The fill factor of PCBs is restricted by the material properties of the insulators between copper traces wherein voltage creepage threatens the integrity of the PCB if gaps are created below a minimum defined in current standards for PCB manufacturing. For a coreless machine operating at a very low fundamental frequency of 25 Hz, the copper trace width of 1.2 mm was employed [17]. Another group considered trace width of 0.2-0.3 mm and trace height of 0.07-0.105 mm with the gap between traces set at 0.23-0.3 mm for a machine operating at a fundamental frequency of 33.3 Hz [50]. In a PM machine designed for operation at 1 kHz, a copper trace width of 0.3 mm was adopted, with a 0.3 mm circumferential gap between traces [51]. The generic standard on PCB design, IPC-2221, recommends to have a minimum gap of 0.13 mm between traces at our intended voltage and a minimum trace width of 0.15 mm was chosen to allow for that gap for the design target under study.

2.4 Electromagnetic FEA for Electric Machines

FEA is a commonly used technique to assess the performance of electric machines. The machine is broken down into small elements, and calculations are performed on each of these elements. The accuracy of the calculations is influenced by the size of the mesh, which should be optimized to balance accuracy and computation time. As the number of elements increases, so does the accuracy of the simulation, but this also leads to longer computation times.

Recent advancements in computer software and hardware have led to widespread use of FEA in the design process of electric machines. New FEA tools have improved the flexibility of designing, allowing for shapes beyond 2D and even 3D. Using 3D FEA in the design of axial-flux machines, for example, allows designers to consider the effects of 3D flux paths and eddy-current distributions. FEA also enables designers to perform parametric studies to understand the impact of each geometric detail on the motor's performance. During computation, magnetic saturation and eddy currents are taken into account. FEA is considered to be a highly accurate analysis technique for electric machine design, but it comes with a longer computation time compared to other techniques.

2.4.1 Field problems: formulations and solutions

Electromagnetic field models and finite element analysis are used together to compute electromagnetic fields in computational electromagnetics. They are utilized to calculate and understand the behavior of electromagnetic fields for the steady-state performance of a synchronous permanent magnet (PM) machine at various time points, rotor positions, and stator current distributions. This section reviews finite element analysis for solving Maxwell's equations that govern the behavior of electromagnetic fields. The review is reliant on published references which are included. [52, 53].

A simplified version of Ampere's law is included in the part of the Maxwell equations that governs the magnetostatic field:

$$\nabla \times H = J \ , \tag{2.8}$$

and the reduced form of Gauss's law:

$$\nabla \cdot B \ = \ 0 \ . \tag{2.9}$$

The material's magnetic non-linearity is represented:

$$B = B_r + \mu(B)H, \tag{2.10}$$

where the remanence B_r is non-zero values only in the PMs.

Since magnetostatic fields are solenoidal, they can be analyzed using a magnetic vector potential (MVP) for simplification. This MVP is defined as:

$$\nabla \times A = B \tag{2.11}$$

In combination with the Coulomb gauge condition

$$\nabla \cdot A = 0 \tag{2.12}$$

By applying Gauss' magnetic flux law (2.9) to the previous equation (2.11), the resulting equation is the magnetic vector potential equation as:

$$\nabla \cdot (\nabla \times A) \equiv 0 \ . \tag{2.13}$$

By combining the equations mentioned above, the Poisson vector equation can be obtained:

$$\nabla \times \left(\frac{1}{\mu}\nabla \times A\right) = J + \left(\frac{1}{\mu}\nabla \times B_r\right) . \tag{2.14}$$

Rewrite the equation above for cases where the magnetostatic fields are non-linear and the materials are isotropic:

$$\frac{\partial}{\partial x}\left(\frac{1}{\mu}\frac{\partial A}{\partial x}\right) + \frac{\partial}{\partial y}\left(\frac{1}{\mu}\frac{\partial A}{\partial y}\right) = -J - \left[\frac{\partial}{\partial x}\left(\frac{B_{r,y}}{\mu}\right) - \frac{\partial}{\partial y}\left(\frac{B_{r,x}}{\mu})\right)\right] . \tag{2.15}$$

In electrical machine problems, anti-periodic or periodic boundary conditions are used to simplify the analysis of cross-sectional fields to either an odd or an even number of poles:

$$A(r,\theta) = -A\left[\theta + \frac{(2k-1)\pi}{p}\right], \ \ A(r,\theta) = -A\left[\theta + \frac{2k\pi}{p}\right], \tag{2.16}$$

where p is the number of pole pairs and r, θ are polar coordinates.

The process of Finite Element Analysis (FEA) involves using a network of nodes to create a grid that breaks down the field region into smaller elements. In the example illustrated in Figure 2.4, the magnetic vector potential is calculated at point P, which is located within one of the smaller elements (e), by considering the values of A at the np nodes within that element and using the corresponding shape function N.

$$A^e(P) = \sum_{i=1}^{np} N_i^e(P)A_i^e. \tag{2.17}$$

Triangular elements of the first or second order are typically employed in FEA models of electrical machines. The first-order elements, $np = 3$, have three nodes, i, j, k, placed in the three verticals as shown in Figure 2.4. The second-order elements have 3 nodes at the verticals and another 3 on the mid-points of each edge.

FEA models of electrical machines commonly use triangular elements of the first or second order. The first-order elements contain three nodes, i, j, k, placed at the three vertices, as illustrated in Figure 2.4. On the other hand, the second-order elements consist of six nodes, with three nodes located at the vertices and the remaining three placed at the mid-points of each edge.

The shape functions for first-order elements are:

$$N_i^e(x, y) = \frac{1}{2\Delta^e}(a_i^e + b_i^e x + c_i^e y), \; i = i, j, k \tag{2.18}$$

where

$$\Delta^e = \frac{1}{2}\begin{vmatrix} 1 & x_i^e & y_i^e \\ 1 & x_j^e & y_j^e \\ 1 & x_k^e & y_k^e \end{vmatrix} \tag{2.19}$$

$$\begin{bmatrix} a_i^e & b_i^e & c_i^e \\ a_j^e & b_j^e & c_j^e \\ a_k^e & b_k^e & c_k^e \end{bmatrix} = \begin{bmatrix} x_j^e y_k^e - x_k^e y_j^e & y_i^e - y_k^e & x_k^e - x_j^e \\ x_k^e y_i^e - x_i^e y_k^e & y_k^e - y_i^e & x_i^e - x_k^e \\ x_i^e y_j^e - x_j^e y_i^e & y_i^e - y_j^e & x_j^e - x_i^e \end{bmatrix} \tag{2.20}$$

For first-order triangular elements the approximation model for the magnetic vector potential is provided by:

$$A^e(x, y) = \sum_i^k N_i^e(x, y) A_i^e = [N_e]\{A^e\}, \tag{2.21}$$

$$B_x^e = \frac{\partial A^e}{\partial y} = \frac{1}{2\Delta^e}\sum_i^k c_i^e A_i^e = ct \;, \tag{2.22}$$

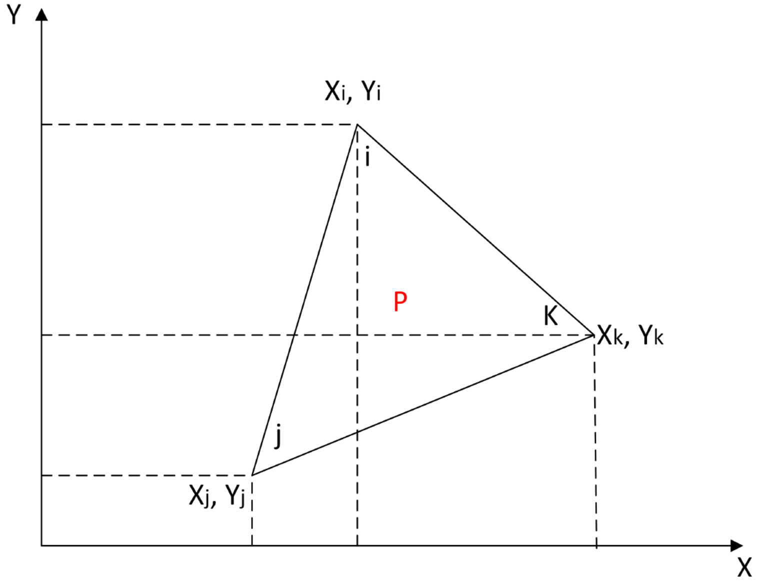

Figure 2.4: Triangular finite element in the xy plane.

$$B_y^e = -\frac{\partial A^e}{\partial x} = -\frac{1}{2\Delta^e} \sum_i^k b_i^e A_i^e = ct \ , \tag{2.23}$$

where the summation is processed for $i = i, j, k$ and the element is identified by the superscript.

The magnetostatic field functional is obtained from the energy density in a general form as follows:

$$\mathcal{F} = \int_\Omega \left[\int_0^B \frac{1}{\mu(B)} (B - B_r dB - JA) \right] d\Omega \ . \tag{2.24}$$

For 2D fields , the equation becomes simpler and can be expressed as:

$$\mathcal{F} = \int_D \left\{ \frac{1}{2\mu} \left[\left(\frac{\partial A}{\partial x} \right)^2 + \left(\frac{\partial A}{\partial y} \right)^2 \right] - \left\{ J - \left[\frac{\partial}{\partial x} \left(\frac{B_{r,y}}{\mu} \right) - \frac{\partial}{\partial y} \left(\frac{B_{R,X}}{\mu} \right) \right] \right\} \right\} dxdy. \tag{2.25}$$

This functional is minimized with respect to the unknown magnetic vector potential A over a finite element a mesh with n_t nodes:

$$\frac{\partial \mathcal{F}^e}{\partial A_i} = \sum_e^{m_i} \frac{\partial \mathcal{F}}{\partial A_i^e} = 0, \ i = 1, 2, \cdots, n \ , \tag{2.26}$$

where the summation is performed for the m_i elements that have the i node common.

We can obtain a system of equations that is non-linear and algebraic as:

$$\sum_{e}^{m_i} \sum_{\lambda=i,j,k} K_{i\lambda}^{e} A_{\lambda}^{e} + \sum_{e}^{m_i} G_i^e = 0,\ i = 1, \cdots, n \tag{2.27}$$

with the coefficients:

$$K_{i\lambda}^{e} = \frac{1}{4\Delta^e \mu(B)} \left[c_i^e c_\lambda^e + b_i^e b_\lambda^e \right],\ \lambda = i, j, k \tag{2.28}$$

$$G_i^e = -\frac{1}{3}\Delta^e J^e + \frac{1}{2}\left[\frac{b_i^e B_{r,y}^e}{\mu_m^e(B^e)} - \frac{c_i^e B_{r,x}^e}{\mu_m^e(B^e)} \right] \tag{2.29}$$

Based on the magnetic vector potential solution, the x and y components of the magnetic flux density are derived in further chapters.

2.4.2 Eddy currents and associated losses based on FEA and analytical calculations

Litz wires consist of multiple strands insulated electrically from each other, which are usually twisted or woven to minimize the skin effect and proximity effect. Accurate predictions of eddy current loss in Litz wires involve detailed 3D wire models for which the scale of the problem is usually prohibitive for solving without using the high performance computing system. To reduce the burden of modeling and computation, numerous reduced-order methods were proposed, such as the fast 2.5-dimensional (2.5D) partial element equivalent circuit [54], the combined numerical and analytical approach called the squared-field-derivative method [55], the hybrid method that combines the analytical equations and FE simulations [12, 13], etc.

In contrast with Litz wire windings, PCB windings are comprised of large numbers of copper traces, which are typically straight and without complex transposition.

Eddy current loss in PCB traces can be estimated by 2D or 3D FE models, as described, for example, in [16, 51, 56].

For coreless machines, the eddy current loss needs to be considered during the design and optimization stage. However, the calculation of eddy current loss in conductors, including Litz wires and PCB traces, if solved directly using FE solvers, is time-consuming and challenging for large-scale design optimizations [53]. This study proposes to use a hybrid analytical–numerical approach that can be directly incorporated into the multi-objective optimization algorithm to quickly estimate the eddy current loss in windings based on the variation of average flux density in equivalent macro coils from 3D transient FEA.

Based on the guidelines from the previous section, the wire gauge for each strands needs to be at least AWG 38. A Litz wire consisting of 100 strands of AWG 40 magnet wires was selected, which is expected to be able to reduce the ac winding losses for this study to negligible levels. The equivalent macro coil model for Litz wire windings is illustrated in Fig. 2.5.

Assuming that all the conductors in coils are straight and directly exposed to a uniform magnetic field varying sinusoidally with time, neglecting the eddy current loss in end coils, the eddy current loss in Litz wire windings with round conductors is estimated by:

$$P_{eddy} = \sigma L_c N_c N_t N_s \omega^2 \frac{B_a^2 \pi d^4}{128}, \tag{2.30}$$

where σ is the conductivity of conductors, ω the electrical angular velocity, L_c the length of conductors, N_c the number of coils, N_t the number of turns per coil, N_s the number of strands per turn, d the diameter of each strand (conductor). B_a is the

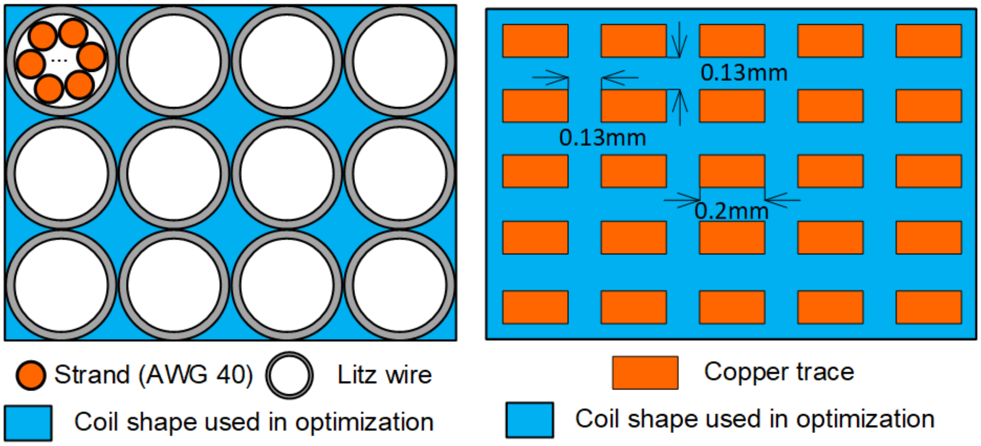

Figure 2.5: Cross sections of equivalent macro coils of Litz wire and PCB stator windings used in 3D parametric models for optimization. Dimensions of PCB traces and the gap between them depend on the number of layers, overall thickness, finnished copper, etc., and are closely related to PCB manufacturers.

amplitude of the flux density [12].

For PCB stator windings, the traces are treated as rectangular wires, and the equation for eddy current loss estimation is:

$$P_{eddy} = \sigma L_c N_c N_t N_s \omega^2 \frac{(B_{az}^2 w^2 + B_{a\phi}^2 h^2) w h}{24}, \tag{2.31}$$

where B_{az} and $B_{a\phi}$ are the axial and tangential components of the flux density, and w and h are the width and height of each strand, respectively.

2.5 Design and Optimization Case Studies

2.5.1 High-speed AFPM machines for FESS

In this section, two main topologies, i.e., the conventional single-sided AFPM machine with stator and rotor cores and the coreless structure with two rotors and a central stator, as illustrated in Fig. 2.6, are evaluated by finite element analysis (FEA) to show their suitability for FESS applications in terms of specific power, efficiency and open-circuit losses. Both 3-phase and 2-phase windings can be employed in the

AFPM machines under study. The coreless design example adopts the 2-phase wave winding in order to show the enhanced fault-tolerant capability due to the magnetic decoupling between the two phases.

The proposed motor/generator designs are modular low-power high-speed units. They have the same power rating 17.5 hp and will run between 25,000 rpm and 50,000 rpm, corresponding to a maximum depth of discharge 0.5. The same envelope dimensions, i.e., total outer diameter = 200 mm and total axial length = 50 mm, are used for both the designs with and without stator core. The magnet grade is NdFeB N30 and the stator core is made of lamination steel M15-29G.

For the AFPM machine with core, the fundamental frequency at very high speed operation and number of poles are limited by the core losses, which are approximately proportional to the square of fundamental frequency. By eliminating the stator core and associated core losses, the coreless design may employ a higher number of poles. A parametric study is carried out to show the influence of number of poles on the motor/generator performance. The current density is adjusted accordingly to achieve the target torque 5 Nm at 25,000 rpm. The motor/generator can operate up to 50,000 rpm but the torque is reduced to 2.5 Nm to maintain constant output power.

As shown in Fig. 2.7, the coreless machine designs can achieve a specific power output of around 6 kW/kg, regardless of the number of poles from 4 to 10, while the design with stator core has a much lower value due to the required large core volume and mass. Furthermore, the applied current density reduces with the increase in the number of poles for coreless machines. This is caused by the relatively low torque capability of machines with a low number of poles for a small ratio of total axial

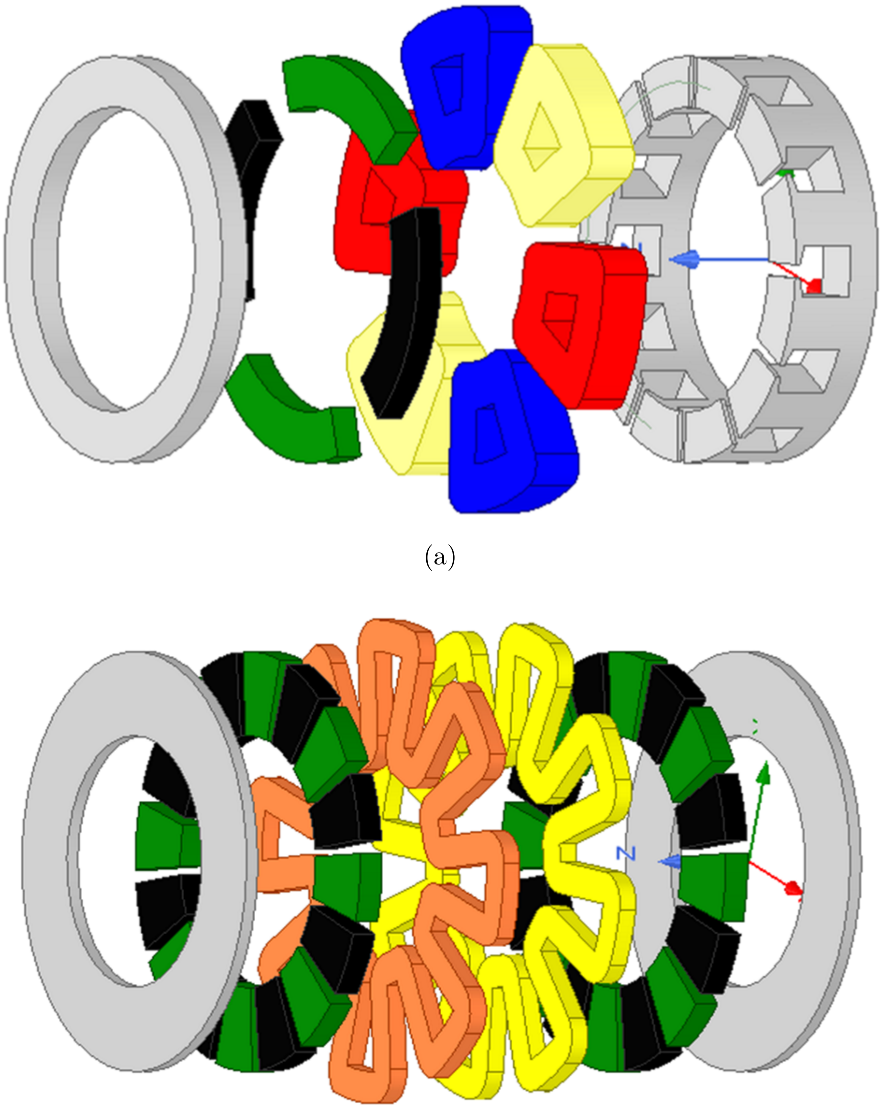

(a)

(b)

Figure 2.6: Two typical AFPM machine topologies, (a) with stator core, (b) without stator core. Concentrated or wave-type windings may be used to reduce the length of end winding and associated copper losses, as well as for the ease of manufacturing. Solid conductors are depicted for illustration, and they would be made of fine wire or Litz wire to minimize the high-frequency AC losses.

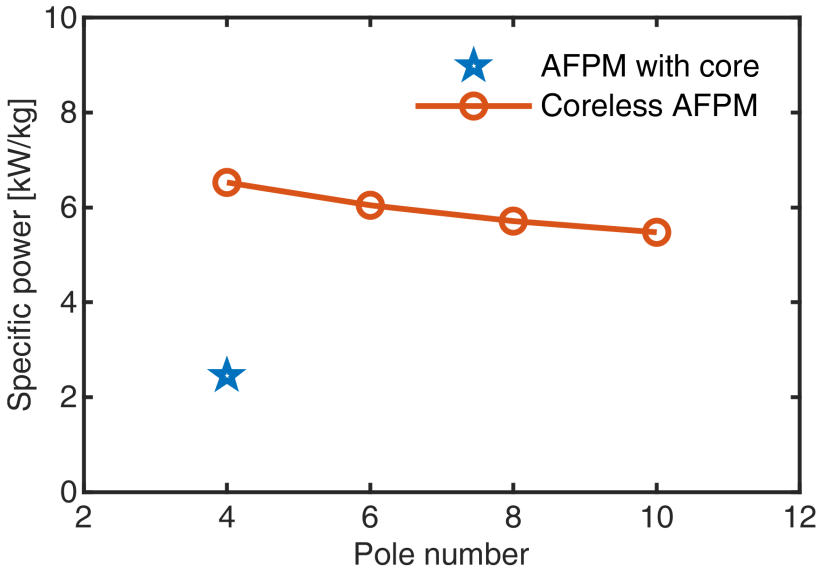

Figure 2.7: Specific power of AFPM machine design examples with and without stator core. The pole number of the design with stator core is mainly limited by the core losses at high rated frequencies. In contrast, the coreless design may have more poles due to the elimination of core losses.

length to total diameter [57].

It may be noted that coreless machines tend to feature high conductor AC losses, due to eddy currents induced by the time-dependent variations of the airgap magnetic field, and therefore would need to be designed with fine multi-strand conductors or Litz wire. For the example design based on multi-strand conductors shown in Fig. 2.8, the induced instantaneous current density is more than twice the applied current density at 25,000 rpm, indicating that the use of Litz wire may be necessary in this case.

The efficiency of the designed electric machines in charging/discharging mode is shown in Fig. 2.9. It may be observed that the efficiency is almost invariant with the number of poles for the operation at 25,000 rpm, while at 50,000 rpm, the efficiency drops sharply with the increase of pole number, indicating that either a lower rotor

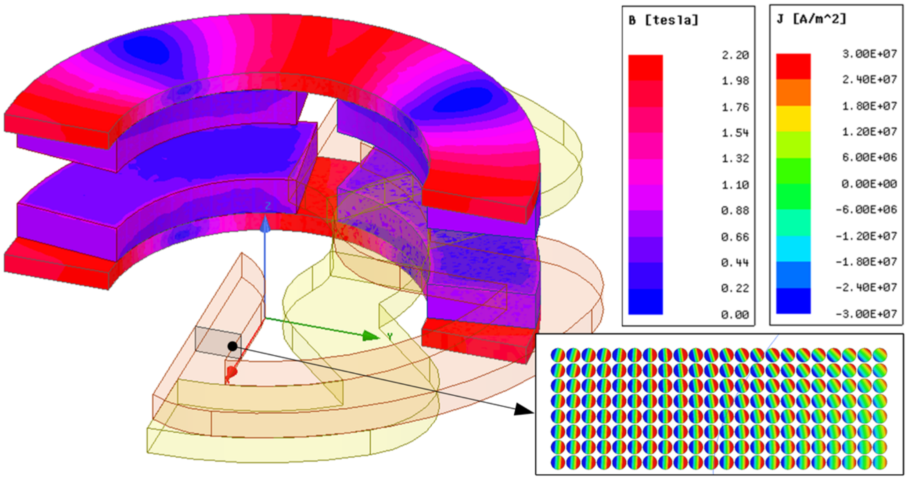

Figure 2.8: Flux density and instantaneous current density distribution for an example 4-pole coreless design using multi-strand conductors at 25,000 rpm. The high induced current densities indicate that Litz wire may need to be used to mitigate the high frequency conductor losses.

polarity, or a winding design with Litz wire may be the right choice.

It is worth noting that in order to operate AFPM machines with relatively large pole numbers at very high speeds, it is necessary to use wide-bandgap (WBG) switching devices to enable higher fundamental frequency as well as improve the system efficiency, such as sillicon carbide (SiC) and gallium nitride (GaN) metal oxide semiconductor field effect transistors (MOSFETs). Inverters with all WBG devices or hybrid switch converters can be employed to drive the proposed low-power high-speed units.

FEA results indicate that designs with a low number of poles are preferred in terms of open-circuit loss. In order to take advantage of the high torque per ampere provided by higher polarity designs, the open circuit loss can be mitigated by increasing the airgap length in standby mode.

The round-trip efficiency is closely related to both the efficiency in charging/discharging mode and power losses in standby mode. In short-term energy storage applications, the efficiency in charging/discharging mode may be more important. For long-term

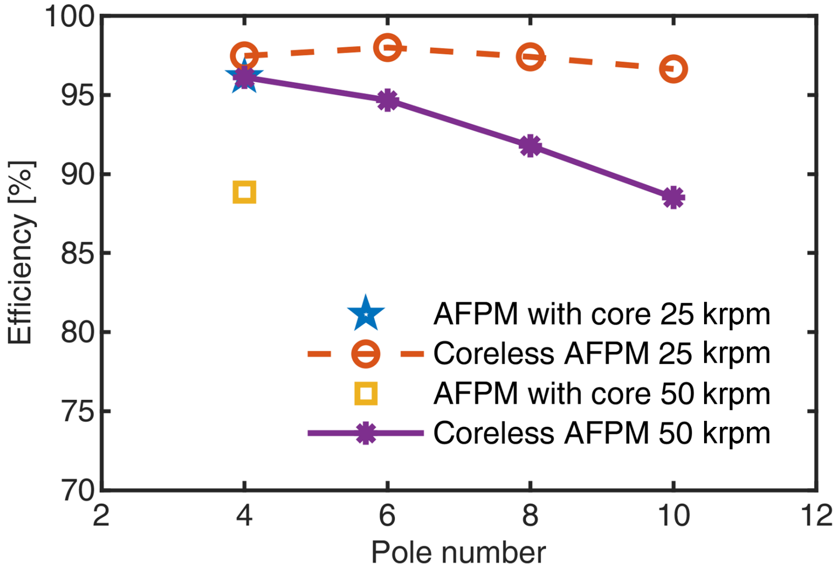

Figure 2.9: Efficiency of AFPM machine design examples with and without stator core at 25,000 rpm and 50,000 rpm.

flywheel energy storage, the standby mode may last a long period of time and the standby power losses become the dominating loss component in a whole round trip.

Based on the calculation results of the design examples, it can been found that AFPM machines, especially those with stator cores, are subject to constraints on the fundamental frequency. Low number of poles are favored to reduce the open-circuit loss. In the case of coreless machines, relatively larger pole numbers provide higher specific power at the same current density level and higher efficiency in the designed charging/discharging speed range. Coreless designs may need to use Litz wire in order to minimize the additional conductor losses at high frequency. It should be noted that the current density in conductors and heat dissipation of stator windings may bring about additional challenges in designing high-speed AFPM machines for FESS applications.

Table 2.4: Optimization Variables and Their Ranges.

Variable	Description	Min.	Max.
R_{ir}	Inner radius of rotor [mm]	80	120
k_{cw}	Coil width / Max. coil width	0.50	0.95
k_{ry}	Rotor yoke thickness / PM axial length	0.5	1.5
k_s	Stator axial length / PM axial length	0.5	2.0

2.5.2 Corelesss AFPM machines

The material properties and dimensions of magnets and Litz wires are kept constant during the optimization since they are predetermined by available suppliers. The dimensions of the stator and rotor back iron are optimized to achieve the minimum total axial length and total electromagnetic loss, including the dc winding loss, ac winding loss and PM eddy current loss. The AC and DC winding losses refer to the eddy current loss and resistance or Joule loss of the winding, respectively. The width and height of equivalent macro coils are m and n times the diameter of Litz wire for Litz wire windings, where m and n are positive integers. They can be equal or unequal. In PCB stator windings, the width and height of the equivalent macro coil are controlled similarly to keep the fill factor constant.

Four independent variables are identified for the optimization, as tabulated in Table 2.4. The geometry of the coreless machine using Litz wire and PCB stator windings is illustrated in Fig. 2.10. The fill factor for equivalent macro coils is determined by the wire layout. It is 0.386 and 0.303 for the Litz wire winding and PCB stator winding shown in Fig. 2.5, respectively.

The optimization method is a variation of the 2-level surrogate-assisted algorithm

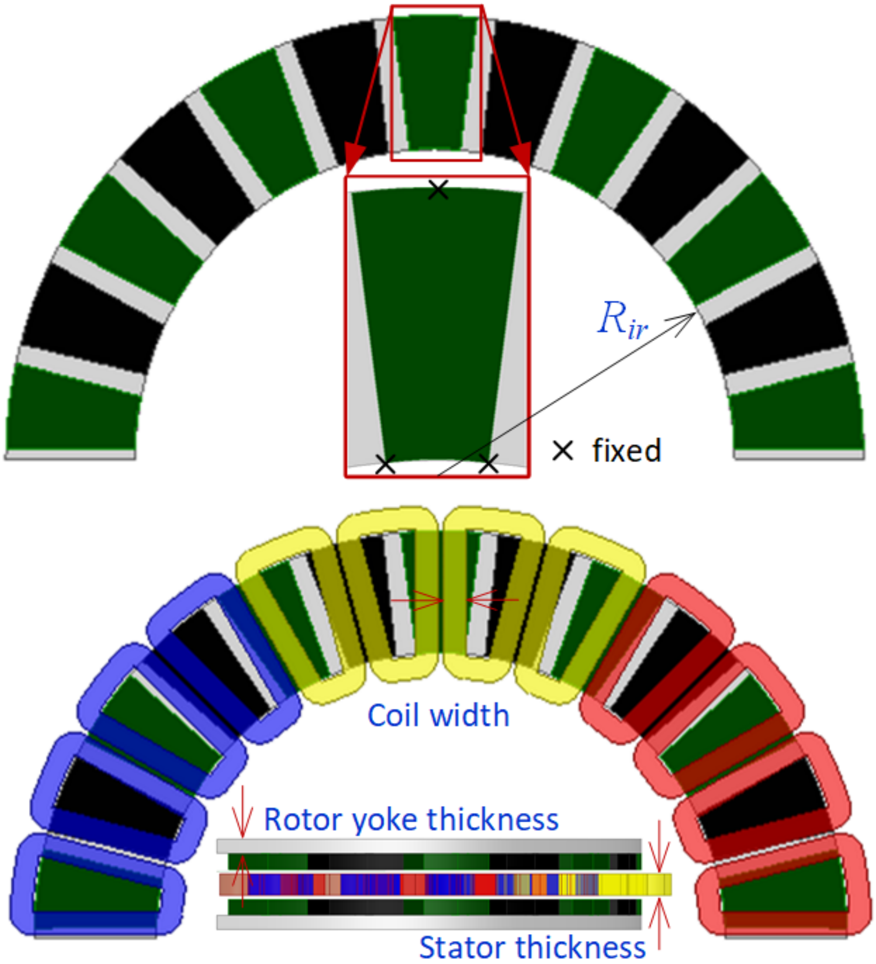

Figure 2.10: Parametric 3D model and main geometric variables.

which combines the multi-objective differential evolution (DE) and kriging metamodels to accelerate the generation of the Pareto front [58]. This optimization algorithm requires a reduced number of design evaluations and can be implemented in powerful workstations or high performance computing systems, enabling the accurate performance calculation of each candidate design in less than 10 minutes.

The Pareto front for the optimization and all the other designs using Litz wires are shown in Fig. 2.11. The highest electromagnetic efficiency achieved by the optimum designs from the Pareto front is 98.8%. The box plot as shown in Fig. 2.12 indicates

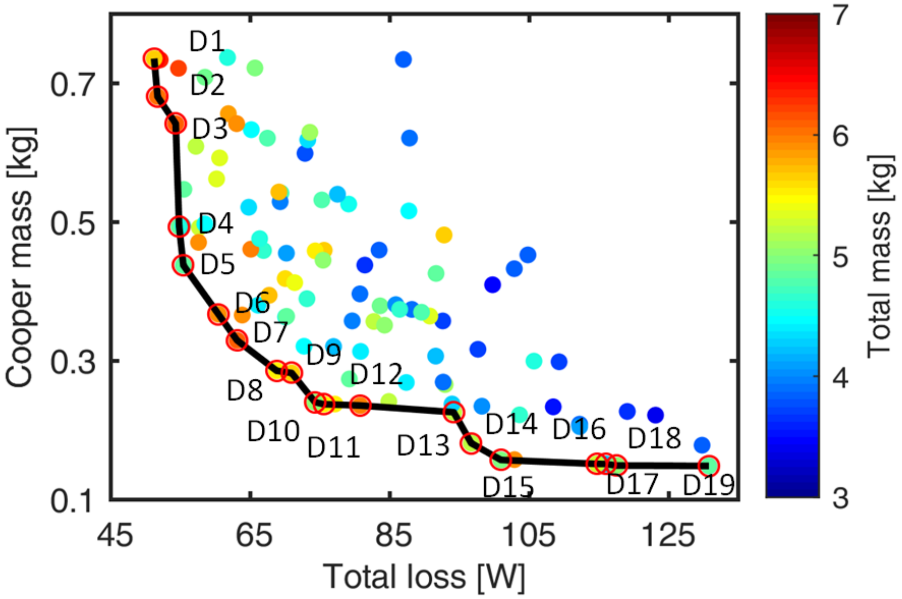

Figure 2.11: The Pareto front and all the other designs evaluated by 3D FEA throughout the differential evolution for the 3-phase AFPM with fractional-slot concentrated windings.

that independent variables of all the Pareto front designs are within their ranges and the optimization is acceptable. The ac winding loss accounts for a small fraction of the total electromagnetic loss, as shown by the loss breakdown in Fig. 2.13.

The PCB version is also optimized following the same procedure except the Litz wires are replaced by rectangular copper traces. The equation used for ac winding loss estimation and fill factor are changed according to the different constructions. One design example with PCB stator windings from the optimization was selected and modeled in detail, as shown in Fig. 2.14. There are two PCBs, one for each phase, stacked with a phase shift of 90 electrical degrees. Each PCB has 6 layers with 50 traces per layer. The terminals are shown in the zoomed-in view in Fig. 2.14a.

Three selected optimal designs have been being fabricated. The customized test fixture shown in Fig. 2.15 is able to adjust the airgap length during the testing. The

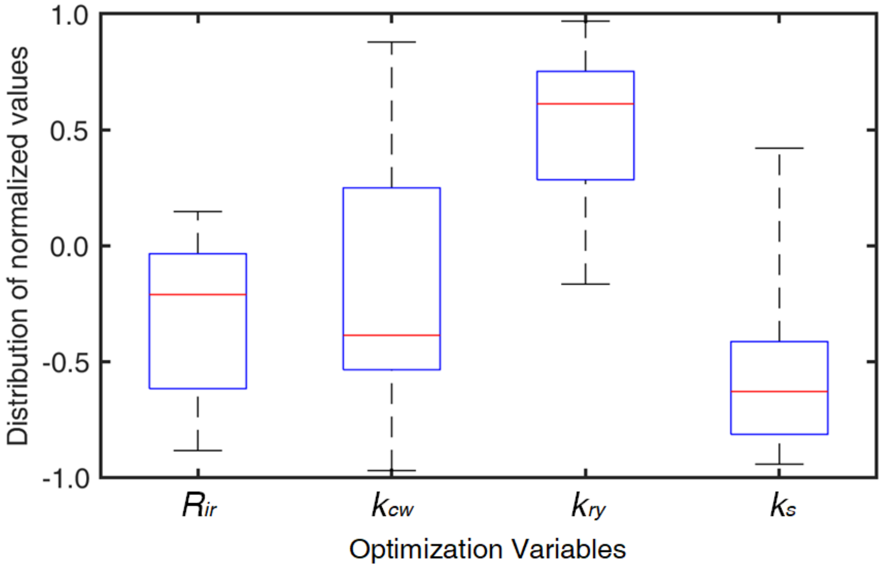

Figure 2.12: Box plot for the Pareto front shown in Fig. 2.11.

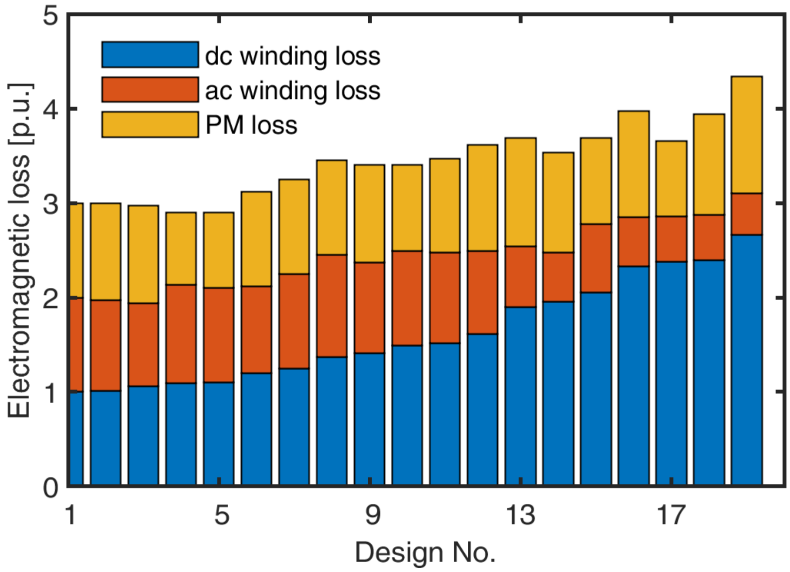

Figure 2.13: The loss breakdown of Pareto front designs shown in Fig. 2.11. The three loss components are normalized relative to the values for the Design 1.

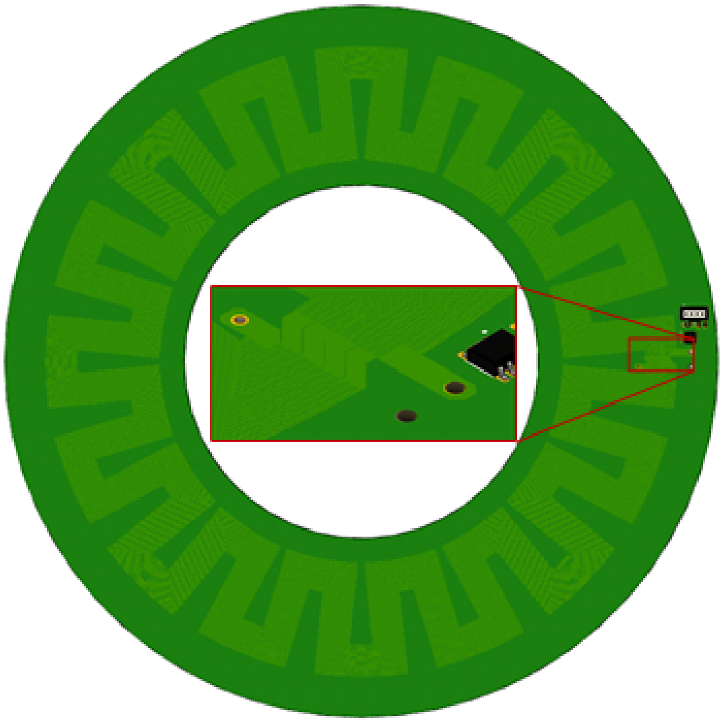

(a)

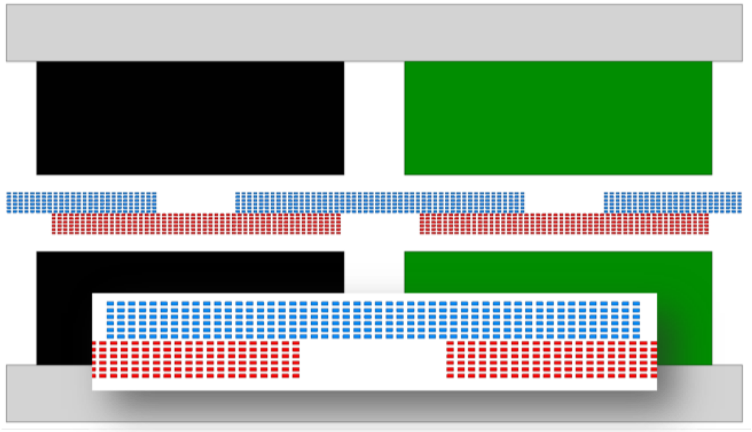

(b)

Figure 2.14: Detailed modeling of a PCB stator design example, (a) top view, (b) unrolled 2D view from a cylindrical cut plane shown together with rotors.

structure developed has been constructed using tight tolerance aluminum jig plate and a 20 mm keyed steel shaft, as well as a dual bearing system for proper alignment. This design allows flexibility for mounting of various AFPM machines and precise calibration of their airgaps. The fixture is also equipped with a vertical back plate with an opening for the shaft such that an encoder can be mounted for speed feedback to be used in the control loop for the machine.

To assemble the coreless machine under test to the fixture, the first of the two rotors is mounted to a flanged clamping shaft collar and then placed onto the shaft into position and locked into place using the collar's locking nuts. Nylon spacers are then bolted to the vertical plate of the fixture, which the stator is then bolted to. This procedure sets the airgap between the first rotor and stator. To combat axial forces present between the second rotor and stator, an adjustment tool is used which allows precise, controlled placement of the second rotor on the shaft. Once the airgap is satisfactory, the second rotor is locked into place using the same flanged shaft collar approach as the first.

2.6 Summary

This chapters presents a summary of the key aspects involved in developing Coreless AFPM machines, including the use of specialized construction techniques such as Litz wires and PCB windings. These techniques are particularly important when operating at high frequencies.

Coreless AFPM machines have special constructions and their windings can be designed with additional degrees of freedom as there are no geometrical constraints

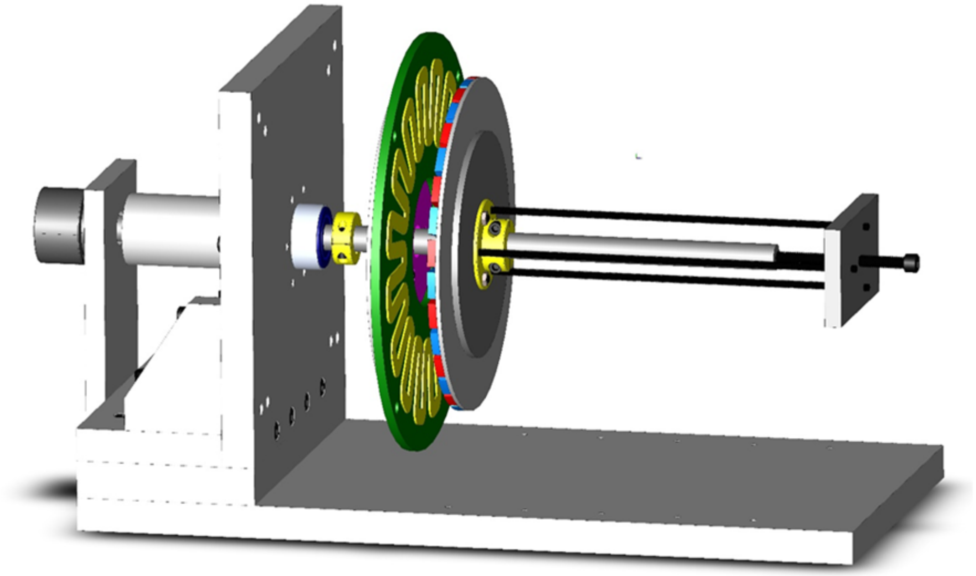

Figure 2.15: Customized test fixture with the coreless machine with PCB stator installed.

imposed by teeth and slots. Such machines may achieve very high efficiency by employing Litz wire or PCB windings and through design optimization.

Flywheels can be used in many different applications where energy storage is required, and they are especially well-suited for use in microgrid and utility grid systems that are integrating renewable energy sources. To achieve high energy density and specific energy, flywheel rotors are often made from composite materials that have high tensile strength and low mass density.

High-speed AFPM machines are evaluated in terms of power density/specific power, efficiency, and open-circuit power losses at high rotating speeds, showing their feasibility in FESS with high energy density/specific energy. The adjustable airgap length of AFPM machines may further benefit the self-discharge reduction in the standby mode. In addition, there is a higher potential to integrate the rotor of axial-flux PM motor/generator with the flywheel rotor due to its disk-like shape. The design study conducted opens up an opportunity for AFPM machines in the grid integration of renewable energy sources.

Chapter 3 Design and Optimization of Axial-flux Vernier PM Machines of the MAGNUS Type

3.1 Introduction and Problem Formulation

In-wheel motors are being increasingly sought in automotive applications in an attempt to simplify the drive train and eliminate gear boxes, which constitute points of failure. In this regard, high-polarity permanent magnet (PM) synchronous machines with fractional-slot concentrated windings, which feature high efficiency, torque density and power factor are commonly employed. These particular machines are well-suited for low-speed direct-drive applications, such as in-wheel traction and wind turbine generators, because they possess a high torque density.

High-polarity PM machines in low-speed applications lead to increased torque density and efficiency, due to the reduction in the flux per pole linked by the stator winding, which allows the use of more compact magnetic parts, as well as shorter end turn volume. Larger rotor polarities require a proportional increase in the number of stator slots and coils, which, for a specified envelope, may become too small to be practically manufacturable. For example, the slot width may become comparable to the thickness of coil insulation, leading to very poor slot filling, increased winding resistance and conductor losses. To address such limitations, a three-phase radial-field vernier-type PM machine with 46 rotor poles, and only 6 stator coils has been proposed in [59]. Other researches on the subject with radial- and axial-flux versions include [60, 61].

Vernier-type permanent-magnet (PM) machines can be considered as well-suited candidates for this type of application. These machines are a type of PM machine that use a stator with teeth that are twice the number of the rotor poles, which allows for a high torque density and a low cogging torque. Important advantages of vernier-type motors include a very low number of stator coils, which may simplify the manufacturing of stator windings, combined with high rotor polarities that provide opportunities for magnetic flux concentration.[62, 63].

In this chapter, axial-flux vernier type machines of the MAGNUS type motor of new topology has been introduced. MAGNUS machines are a type of machine which modulated air gap flux density to generate torque in the general family of vernier machines implemented in axial flux configuration with multiple stators and rotors. The working principle and feasible slot-pole combinations for 2-phase and 3-phase versions have been established. A large-scale optimization study based on three-dimensional (3-D) finite element analysis (FEA) for a MAGNUS AF machine with two special stators and one spoke-type PM rotor was performed.

Further contributions to the subject matter are brought in this paper by studying the torque production and its components with examples from a 3-phase MAGNUS machine, which has 40 rotor poles but only 6 coils wound on the main stator teeth in a single layer arrangement. The stator winding is advantageous in terms of simplified manufacturing, as well as improved tolerance, because phase coils are placed in separate slots. In the active stator, which includes the winding, each main stator tooth has 2 auxiliary teeth. The second stator has neither coils nor main slots and is profiled towards the air-gap in the same way as the active stator. The two stators are rotated relatively to each other by one rotor pole pitch, in order to minimize flux leakage and increase the torque output and the power factor. The rotor is of the spoke PM type, which yields high flux concentration and specific magnetic loading. Prototyping of a MAGNUS motor and its corresponding test fixture were introduced. This chapter is substantially based on the following papers:

- M. G. Kesgin *et al.*, ”Analysis of Torque Production in Axial-flux Vernier PM Machines of the MAGNUS Type,” Proceedings, 2021 IEEE IEMDC, Hartford, CT, USA, 2021, pp. 1-5, doi: 10.1109/IEMDC47953.2021.9449556.

- M. G. Kesgin *et al.*, ”Optimal Study of a High Specific Torque Vernier-type Axial-flux PM Machine with Two Different Stators and a Single Winding,” Proceedings, IEEE ECCE 2020, Detroit, MI, doi: 10.1109/ECCE44975.2020.9235901, pp. 4064-4067 (Oct 2020)

- V. Rallabandi, P. Han, M. G. Kesgin *et al.*, ”Axial-field Vernier-type Flux Modulation Machines for Low-speed Direct-drive Applications,” Proceedings, IEEE ECCE 2019, Baltimore, MD, doi: 10.1109/ECCE.2019.8912550, pp. 3123-3128 (Oct 2019)

3.2 Literature Review and Early Developments in the SPARK Lab at University of Kentucky

Permanent magnet (PM) synchronous motors are well-known for their ability to generate high specific torque and have been created for a variety of for direct-drive low-speed applications, such as in-wheel traction and wind turbine generators. Permanent magnet (PM) machines that incorporate a magnetic gearing effect are advantageous for low-speed direct-drive applications because they have the potential due to its exceptional torque density and potential applications. These types of PM machine topologies, which are often variations of the Vernier-type concept, have been proposed since 1990 and have had recent research published on them in [64–70]. However, because of their high magnetic leakage and relatively large equivalent air-gap, their power factor is naturally low. To improve their performance, dual stator arrangements have been suggested, such as those in [65, 66, 71]. Additionally, air-gap flux modulation techniques, like those used in split tooth machines, could also increase torque output alongside Vernier type machines [64–69].

Among different topologies, machines of the vernier-type in axial-flux (AF) configurations have been reported to have great potential in this respect and were considered suitable candidates for diverse low-speed direct systems, such as electric propulsion systems, generator sets, and others. Important advantages of vernier-type motors include a very low number of stator coils, which may simplify the manufacturing of stator windings, combined with high rotor polarities that provide opportunities for magnetic flux concentration [62, 72].

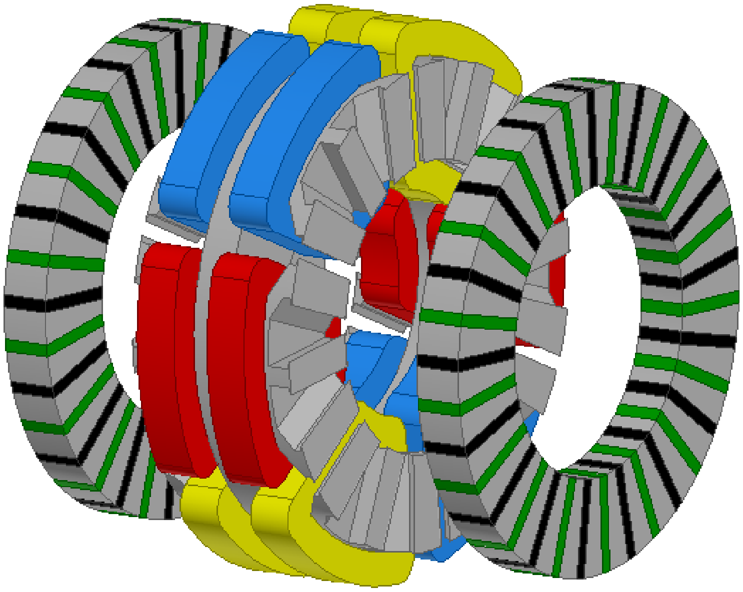

Figure 3.1: Three dimensional model and an NN version of the MAGNUS topology employing a reduced number of concentrated coils in combination with a very large number of rotor poles.

The following literature review is focused on papers previously published by SPARK Group at University of Kentucky [73, 74].

Proposed topology with two rotors and one stator

The study introduced a unique design called MAGNUS as seen Fig. 3.2, which boasts torque magnification features . This is achieved by merging a YASA central stator in an NS configuration with two external spoke rotors that exhibit very high polarity, resulting in a significant flux focusing effect. Interestingly, only a few primary stator teeth are used, each containing a single concentrated winding, similar to the flux reversal machine mentioned in [75]. The design allows for a high number of rotor poles due to the stator's inner surface being specially profiled with small notches, which create extra smaller stator teeth and modulate the air-gap magnetic flux.

The proposed configurations with 6 and 12 coils and up to 44 poles, representing an exceptionally high ratio not previously documented. Additionally, the mathematical relationships between large and small teeth and rotor poles are methodically presented and recorded in tables. Variations of the north-north (NN) type, employing concentrated or Gramme ring type windings, are explored and compared alongside a conventional YASA reference design.

MAGNUS machines are primarily intended for low-speed direct drive systems, where power factor is not a major concern due to the large size and higher cost of the electrical machine compared to power electronics. However, recent advancements in wide band gap semiconductor device technology [76] might make it possible to use these high-polarity, ultra-high specific torque machine designs in higher-speed applications.

Proposed high polarity motor topology

The suggested topology involves using stator coils that are focused around specific main teeth that have notches in the tips to create extra teeth, along with a high polarity PM rotor. This arrangement is shown in a dual-stator axial flux setup with a single rotor in Fig. 3.2. These machines can be designed with various numbers of stator teeth and rotor poles, as depicted in Fig. 3.3.

These unique motors operate based on principles that are similar to Vernier type machines and magnetic gears. Their functioning can be explained by the modulation of the armature MMF (magneto-motive force), which has a different number of poles than the rotor, by the main and auxiliary stator teeth and slots. This creates a flux density component in the air-gap that corresponds to the rotor poles. The relationship

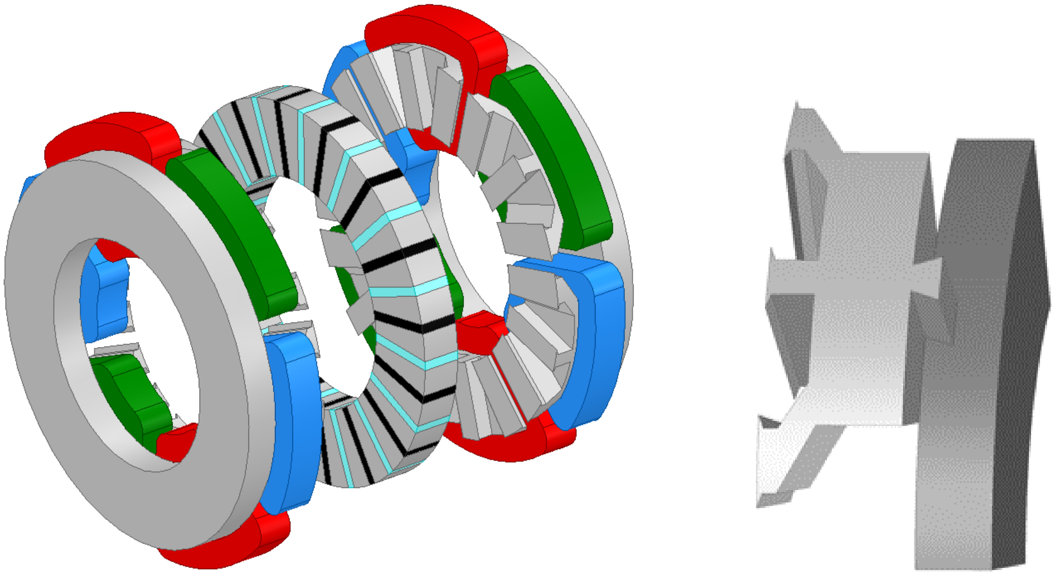
(a) (b)

Figure 3.2: High polarity axial flux machine concept with rotor PMs in a spoke-type arrangement and multiple stator teeth, including a modulated profile towards the air-gap. Flux concentration and modulation is achieved by the dual action of the PMs and stator teeth. The special stator teeth shape allows the use of a relatively small number of coils, which may be pre-wound. High slot fill factors could be achieved together with the possible use of compressed aluminum conductor technology.

between the number of rotor poles, main and auxiliary stator teeth, and armature poles is established as:

$$P_r = 2 \times T_{ms} \times t_{st} - P_a, \tag{3.1}$$

where, P_r is the number of rotor poles; T_{ms}, the number of main stator teeth; t_{st}, the number of auxiliary stator teeth and P_a, the number of armature poles.

The proposed topology's operation is showcased by using the 6/32 machine design mentioned earlier. The analysis presented is simplified and disregards the saliency introduced by the spoke PM rotor. This saliency's significance depends on factors like the number of poles and the ratio of PM pole width to the pole pitch. The analysis also assumes that the widths of the main and auxiliary stator slots are identical.

For example, if a machine has 6 primary stator teeth and 3 additional teeth per

Table 3.1: Feasible large stator teeth, small stator teeth, and rotor pole combinations

Large Stator Teeth	Armature Poles	Small Stator Teeth	Rotor Poles	Winding Factor
6	2	2	22	0.500
		3	34	0.500
		4	46	0.500
6	4	2	20	0.866
		3	32	0.866
		4	44	0.866
9	6	2	30	0.866
		3	48	0.866
		4	66	0.866
12	8	2	40	0.866
		3	64	0.866
		4	88	0.866

main stator tooth and is wound for 4 poles. In that case, it would necessitate 32 rotor poles, as shown in Fig. 3.3b. This configuration is referred to as a 6/32 design for simplicity in the following. 3.1 includes additional feasible stator teeth and rotor pole combinations, along with their fundamental winding factors. If the armature is wound for 2 poles in a variation of this machine topology, the number of rotor poles required would be 34 according to equation (3.1).

The 6/32 machine has the same winding configuration as a 6-slot(teeth) 4-pole PM synchronous machine, the armature reaction MMF of which may be expressed in the form of a Fourier Series over one mechanical cycle of 360° as follows:

$$\begin{aligned} MMF = \frac{9}{4\nu\pi} \sum_{\nu=2,10,16,22..}^{\infty} \cos\left(\nu\theta + \frac{\pi}{3}\right) - \\ \frac{9}{4\nu\pi} \sum_{\nu=4,8,14,20..}^{\infty} \cos\left(\nu\theta - \frac{\pi}{3}\right), \end{aligned} \tag{3.2}$$

and thus the MMF contains not only a 4 pole ($\nu = 2$) component, but also 8, 16, 20,

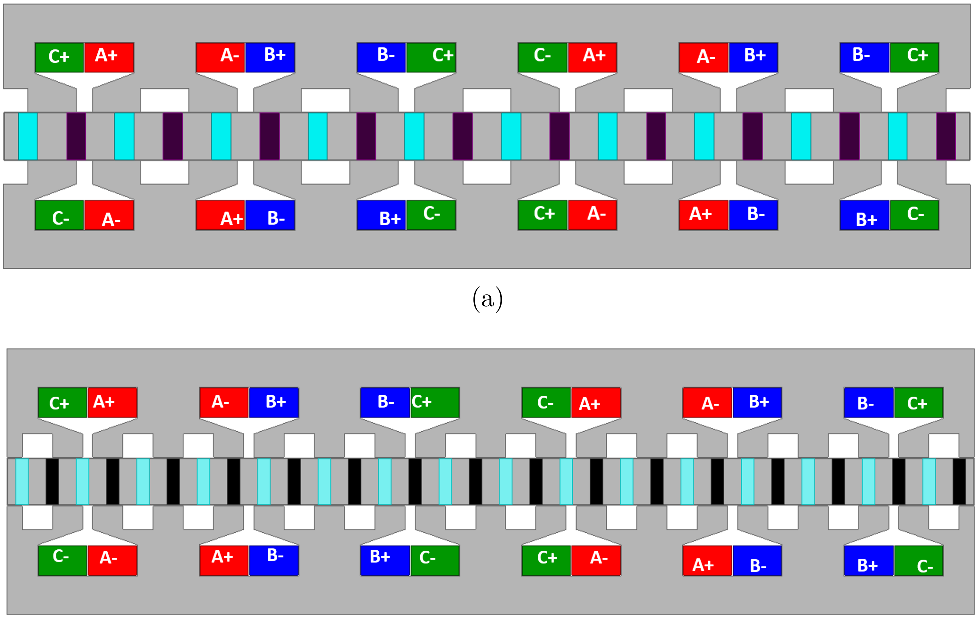

(a)

(b)

Figure 3.3: The proposed axial flux PM machine can be visualized in a linearly unrolled view. Two and three small auxiliary stator teeth are created per main tooth by tip notches in (a) and (b), respectively. Concentrated coils are connected in such a way as to produce a four-pole armature flux in both topologies. In order to correspond with the stator topology and maximize torque production, different numbers of poles, namely 20 and 32, are utilized in the rotor, as shown in Table I. The designs are presented using ”spoke” PM rotor arrangements, but other rotor topologies are also feasible.

and 28 pole components.

The permeance, P_m, caused by all the slot openings and teeth on the air-gap surface can be formulated by ignoring the higher-order components as:

$$P_m = h_o + h_1 \cos 18\theta, \tag{3.3}$$

where h_o is the DC component of the permeance, and h_1 is its fundamental component corresponding to the total number of slot openings, i.e. main slots and "dummy" slots/notches on the stator teeth i.e. $T_{ms} \times t_{st}$).

The result of the armature reaction on the airgap flux can be calculated by multiplying the two terms;

$$\begin{aligned} B_g = P\frac{9}{8\pi}[\cos(2\theta + \frac{\pi}{3}) - \cos(4\theta - \frac{\pi}{3}) + \cos(10\theta + \frac{\pi}{3}) \\ - \cos(8\theta - \frac{\pi}{3}) + \cos(16\theta + \frac{\pi}{3}) - \cos(14\theta + \frac{\pi}{3})...]. \end{aligned} \tag{3.4}$$

The 32 pole component of this air-gap flux density is substantial and interacts with the 32 pole PM rotor field in order to produce a net synchronous torque.

Furthermore, because the permeance has, in addition to the high-order harmonic, a DC component, all the MMF harmonics are also present in the air-gap flux density, i.e. 4, 8, 16, 20, 28, and others. Therefore, the 32 pole component already present in the armature MMF is further enhanced by the interaction of the 4 pole ($\nu = 2$) component of the armature MMF with the fundamental component of the permeance, which has a mechanical harmonic order of 18.

In addition to the high-order harmonic, the permeance also contains a DC component, which means that all of the MMF harmonics are present in the air-gap flux density. This includes the 4, 8, 16, 20, 28, and other harmonics. As a result, the

32 pole component that already exists in the armature MMF is further amplified by the interaction of the 4 pole component of the armature MMF with the fundamental component of the permeance, which has a mechanical harmonic order of 18.

The components of the motor that do not produce torque result in both rotor losses and torque pulsations. However, these non-torque producing components can be minimized through suitable electromagnetic design.

3.3 Systematic Analysis of the MAGNUS Machines

3.3.1 Feasible topologies

The number of spoke rotor poles required may be obtained by considering the following two constraints: (a) at a given time, an odd number of PM poles are opposite to each stator tooth, and (b) the required phase shift is achieved between the phases. The first of these conditions ensures that, at a given time, either only north or only south PM poles lead to phase flux linkage. These conditions are mathematically stated as the following for a two-phase machine,

$$P_r > (2t_a - 1)T_m \ , \ P_r = \frac{T_m}{2}k_1 \ , \tag{3.5}$$

where P_r is the number of rotor poles; T_m, the number of main stator teeth; t_a, the number of auxiliary stator slots; and k_1 is any odd number. For a two-phase machine with 8 main stator teeth, 2 auxiliary or dummy slots, the first value of P_r satisfying both these conditions is 28. Additionally, the machines can also be constructed with different winding configurations, with full-pitched coils or concentrated tooth winding (Fig. 3.5). Some example slot-pole combinations are given (Table 3.2).

Table 3.2: Example feasible main- and auxiliary-slot and rotor pole combinations for two- and three-phase machines with different types of windings. Integral multiples of these combinations can also be used.

Topology	Three-phase			Three-phase			Three-phase			Two-phase			Two-phase		
Main slots	6			9			6			8			12		
Armature poles	4			6			2			4			6		
Winding type	Conc.			Conc.			Full			Full; Conc.			Full; Conc.		
Auxiliary slots	2	3	4	2	3	4	2	3	4	2	3	4	2	3	4
Rotor poles	20	32	44	30	48	66	22	34	46	28	44	60	42	66	90
Fund. winding factor	0.866			0.866			1.000			1.000; 0.707			1.000; 0.707		

3.3.2 Operating principles

A representative two-phase machine with 44 rotor poles and 8 main stator teeth, each with 3 auxiliary teeth, is illustrated in Fig. 3.4a. The two stators are circumferentially shifted from each other by one rotor pole pitch, which serves to improve the flux concentration and reduce the flux leakage [74]. A radial-field vernier type PM machine with distributed windings, a central spoke rotor, and two stators shifted from each other by a pole pitch is also proposed in [77]. In another implementation, windings can be eliminated from one of the stators, and since it has no coils, it may be directly integrated with the supporting frame, as shown in Fig. 3.4b. Such a configuration would be of special interest when the envelope is axially limited, which is usually the case in direct-drive applications. Two typical winding types, i.e., the full-pitched winding and the concentrated tooth winding, can be used, as illustrated in Fig. 3.5.

The operating principle for these machines is the same as that of other vernier-type PM synchronous motors. The stator coils produce an airgap magnetomotive

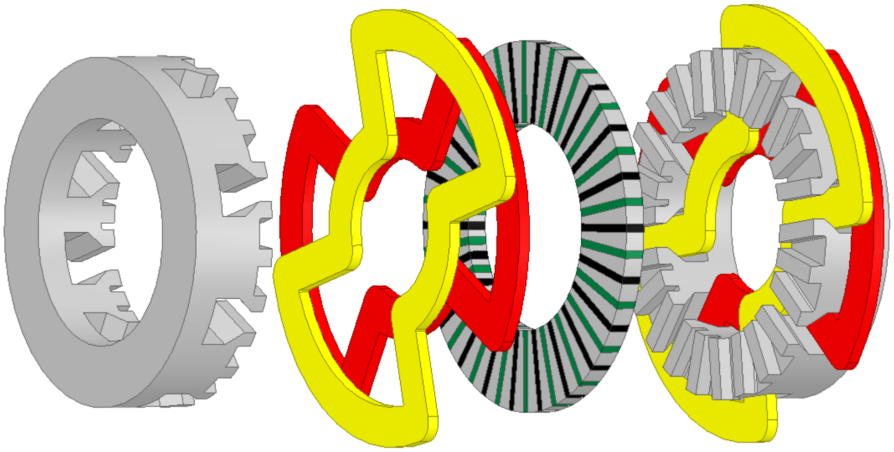

(a)

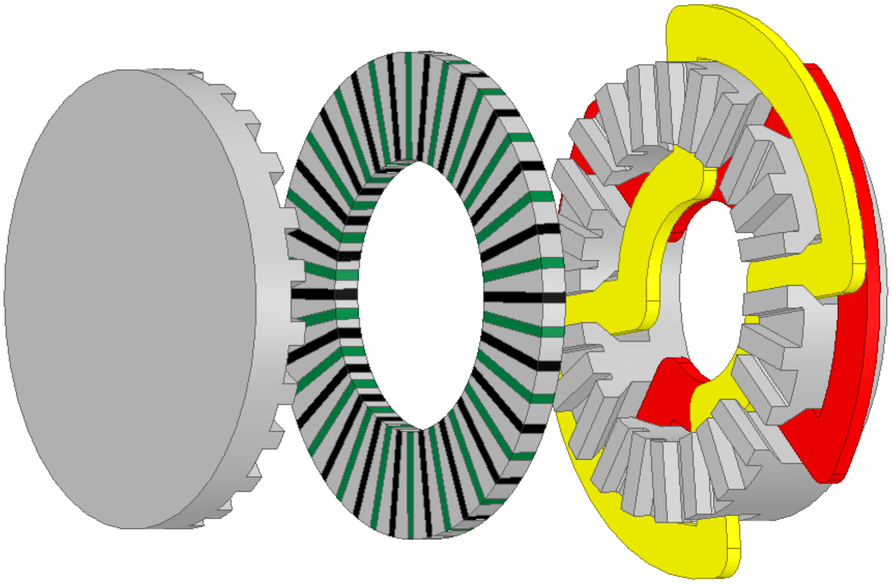

(b)

Figure 3.4: Three-dimensional views for the proposed VTFM PM machines with 1 central spoke rotor and: (a) two active stators, (b) one active stator and one passive stator. The windings, shown as the wave type, can also be implemented as concentrated, full-pitched or gramme windings.

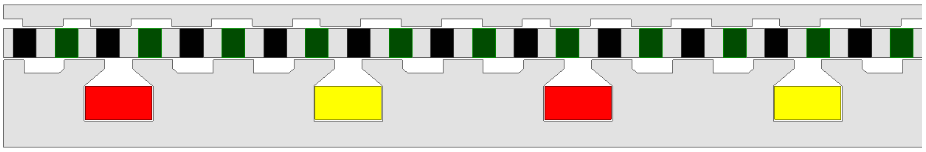
(a)

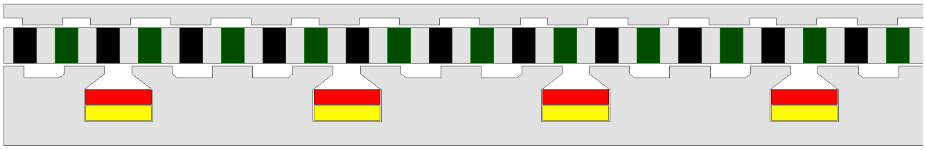
(b)

Figure 3.5: "Developed" two-dimensional views for the proposed VTFM PM machines with 1-central spoke rotor and a single active stator with: (a) full-pitched winding, (b) concentrated tooth winding. Only half the 2D view is shown for each winding type.

force (MMF) and armature reaction flux density rich in harmonics, with the magnitude decreasing with the order, in line with expectations. The stator teeth include dummy slots, the function of which is to enhance the stator winding MMF component corresponding to the number of rotor poles. The dummy slots make it possible to use a stator with a relatively small number of teeth and armature coils along with a high polarity rotor.

Machines of the vernier-type inherently incorporate torque magnification. In AFPM machines, the peak PM flux linkage per phase (ψ_{PM}) may be approximately given as,

$$\psi_{PM} = N_c B_g L_a k \frac{\pi D_m}{P_r} \ , \tag{3.6}$$

where N_c is the number of coils per phase; B_g, the air-gap flux density; L_a, the active length; k, a constant; and D_m, the air-gap diameter. The electromagnetic torque in a motor with m phases with a pure q-axis excitation equal to I_q is given as,

$$T_{em} = m \frac{P_r}{4} \psi_{PM} I_q \ . \tag{3.7}$$

From (2) and (3), it may be noticed as PM flux linkage reduces with increasing number of rotor poles, the electromagnetic torque is independent of it. Second order effects such as reduction in the stator core volume with the increasing number of poles, and consequently increased slot area, permitting higher values of I_q may lead to higher torque.

In the vernier-type PM machines under study in this paper, the number of permanent magnets contributing to the flux linkage of one coil increases linearly with the number of auxiliary slots per main tooth [73]. As observed in Table 3.2, a higher number of rotor poles is required when the number of auxiliary stator slots increases, and therefore, the flux linkage in these types of PM machines is expected to increase with the number of rotor poles. This indicates that these machines would benefit more substantially with higher rotor polarity than conventional machines. Further improvements will also be achieved due to the higher flux concentration in spoke rotors with the increasing number of poles.

The operating principle of these axial-field machines can also be explained by the simple MMF-permeance model. Assuming that there are only fundamental components in the MMF of the spoke rotor and the airgap permeance, the MMF distribution produced by the PM array $f_m(\underline{\phi}, t)$ and the airgap permeance $\lambda(r, \phi)$, based on the coordinate system illustrated in Fig. 3.6 can be written as:

$$f_m(\underline{\phi}, t) = F_m \cos\left[p_m(\underline{\phi} - \phi_{0m})\right] \tag{3.8}$$

$$\lambda(r, \phi) = \lambda_0(r) - \lambda_1(r) \cos\left[N_{SP}(\phi_0 - \phi_{0SP})\right] \tag{3.9}$$

where $\underline{\phi}$ is the angular position in rotor reference frame; F_m, the amplitude of per-pole MMF created by the PM array; $p_m = P_r/2$, the number of rotor pole pairs; ϕ_{0m}, the position of the reference axis in rotor reference frame; ϕ, the angular position in stator reference frame; $N_{SP} = T_m t_a$, the total number of auxiliary stator slots. ϕ_{0SP} is the position of the reference axis in stator reference frame. λ_0 and λ_1 are the average airgap permeance and the amplitude of the pulsating component, respectively.

The angular positions in rotor and stator reference frames are related to each other by:

$$\phi = \underline{\phi} + \theta_r = \underline{\phi} + \omega_r t + \theta_{r0} \tag{3.10}$$

where θ_r is the angle that the rotor rotates relative to the stator, ω_r the rotor speed and θ_{r0} the initial position of rotor with reference to the stator. Similarly, all the harmonic components in the stator MMF produced by the stator winding are also neglected for simplicity. The airgap flux density distribution contributed by both the rotor and the stator MMFs is:

$$\begin{aligned}
&\left[f_m(\underline{\phi}, t) + f_s(\phi, t)\right]\lambda(r, \phi) \\
=&F_m\lambda_0(r)\cos\left[p_m\phi - p_m\omega_r t - p_m(\theta_{r0} + \phi_{0m})\right] \\
&+ \frac{1}{2}F_m\lambda_1(r)\cos[(-p_m + N_{SP})\phi + p_m\omega_r t \\
&- \gamma + (\varphi_s - p_s\phi_{0s})] \\
&+ \frac{1}{2}F_m\lambda_1(r)\cos[(p_m + N_{SP})\phi - p_m\omega_r t \\
&- \gamma + (\varphi_s - p_s\phi_{0s}) - 2p_m(\theta_{r0} + \phi_{0m})] \\
&+ F_s\lambda_0(r)\cos[p_s\phi + \omega_s t + (\varphi_s - p_s\phi_{0s})] \\
&+ \frac{1}{2}F_s\lambda_1(r)\cos[(-p_s + N_{SP})\phi - \omega_s t \\
&- \gamma - p_m(\theta_{r0} + \phi_{0m})] \\
&+ \frac{1}{2}F_s\lambda_1(r)\cos[(p_s + N_{SP})\phi + \omega_s t \\
&- \gamma + 2(\varphi_s - p_s\phi_{0s}) - p_m(\theta_{r0} + \phi_{0m})]
\end{aligned} \tag{3.11}$$

where $F_s = \frac{4}{\pi}\left[N_{ph}k_{w1}I_s/(2p_s)\right]$. N_{ph} is turns in series per phase, k_{w1} the fundamental winding factor, I_s the amplitude of phase current, p_s the number of stator winding pole pairs, and ϕ_{0s} the angular position of phase-A winding axis in stator reference frame.

Equation (3.11) indicates that, both the rotor MMF and stator MMF have additional magnetic field components due to the presence of the auxiliary stator slots. The rotor MMF has components corresponding to different number of pole pairs, i.e., p_m and $N_{SP} \pm p_m$, and rotating at different speeds. The pole pairs of those airgap magnetic field components associated with the stator MMF are p_s and $N_{SP} \pm p_s$, respectively. Non-zero electromagnetic torque will be produced once one or more

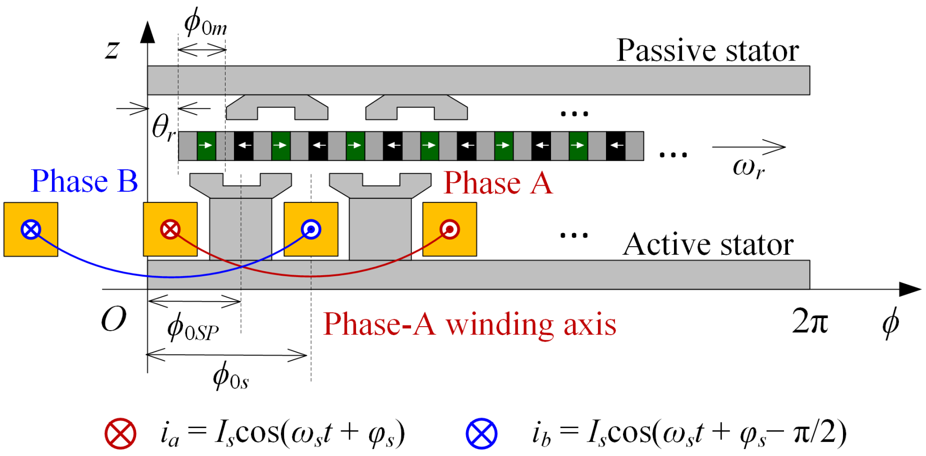

Figure 3.6: The coordinate system used for theoretical analysis. The proposed VTFM machine with 1-active and 1-passive stator is modeled. It may be noted that the phase sequence is opposite to the rotating direction of the spoke rotor, which is different from conventional PM machines.

airgap field components due to the stator MMF synchronize with other components produced by the rotor MMF. It may be noted that the slot pole combinations of Table 3.2 can also be derived by considering the rotor and stator MMFs to be synchronous as per the following,

$$p_m = N_{SP} - p_s \tag{3.12}$$

Manufacturing challenges can arise in these machines owing to the slotted and notched stator teeth. A more feasible approach may be to construct the machine similar to other axial-field PM machines, and add a modulating layer with slots and teeth afterward. The modulating layer can be made of soft magnetic composite material, and affixed to the stator structure through a dovetail.

3.3.3 Three-Dimensional (3D) models for finite element analysis(FEA)

In order to study the performance of the proposed machine configurations, an example two-phase 16-slot 56-pole example machine, as illustrated in Fig. 3.7 is

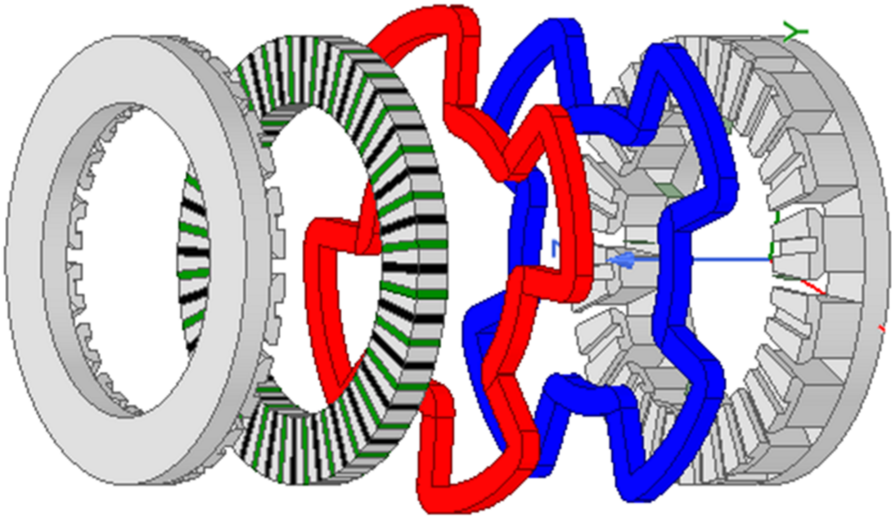

Figure 3.7: Exploded view for the VTFM example machine with 16 stator slots and 56 rotor poles. In an alternate implementation, a modulating structure comprising discrete soft magnetic poles can be placed between the rotor and each stator. In this case, the stator can be made by conventional stamping techniques, thereby greatly simplifying the manufacturing.

modeled via 3-dimensional (3D) FEA. Although the machine can be configured with as few as four stator slots and coils, a 16-slot example is chosen for illustration due to the shorter end turns. The full 3D model, along with the mesh employed in the computational study is shown (Fig. 3.8). The computed back-EMF at the rated speed of 600rpm shows little THD (Fig. 3.9a). The torque waveforms for a full electrical cycle at half-load and full-load conditions are presented (Fig. 3.9b). Low torque ripple ($< 10\%$) is observed even at full-load.

The torque of the 16-slot 56-pole VTFM machine versus the current angle is calculated with 3D FEA and illustrated in Fig. 3.10a and Fig. 3.10b for half-load and full-load conditions, respectively. It can be seen that with the increase of the stator current, the current angle where the peak torque occurs deviates slightly from the theoretical value of 90 degrees. This indicates that the VTFM PM machine shows

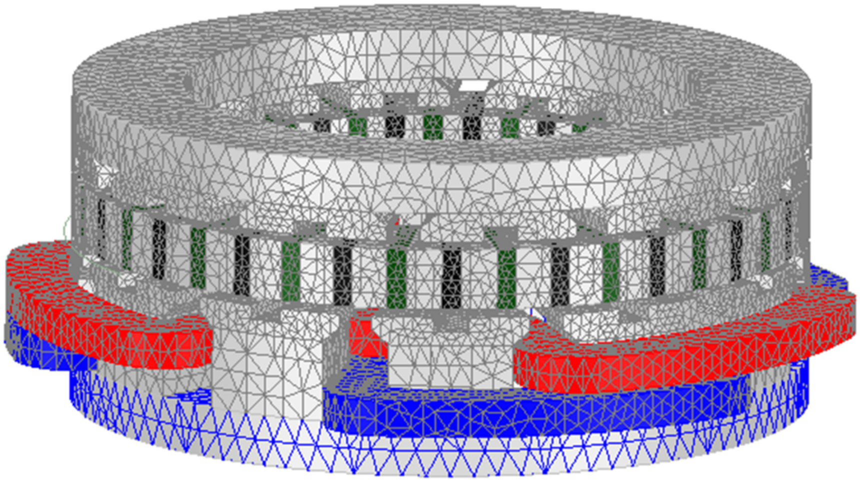

Figure 3.8: Mesh plot used in the 3D FEA model for the VTFM example machine with 16 stator slots and 56 rotor poles. The full problem featured 239193 tetrahedral elements and a quarter model is analyzed to reduce the computational burden.

weak magnetic saliency when the laminated core is saturated.

Based on the phasor diagram for steady state operation, it can be shown that the power factor angle φ depends on current angle γ, PM flux linkage $|\psi_{PM}|$ and stator winding inductance L_s as given by the following:

$$\frac{L_s I_s}{|\psi_{PM}|} = \frac{-\cos(\gamma+\varphi)}{\cos\varphi} \tag{3.13}$$

If $i_d = 0$ control is used, γ is $\pi/2$, and (3.13) can be simplified to:

$$\cos\varphi = \frac{1}{\sqrt{1+\left(L_s I_s/\psi_{PM}\right)^2}} \tag{3.14}$$

Equation (3.13) indicates that the power factor is also impacted by the loading level, i.e., I_s, and the current angle γ. Higher power factors are more likely to be achieved in the case of machines with smaller electric loadings, for example, naturally cooled machines (Fig. 3.10).

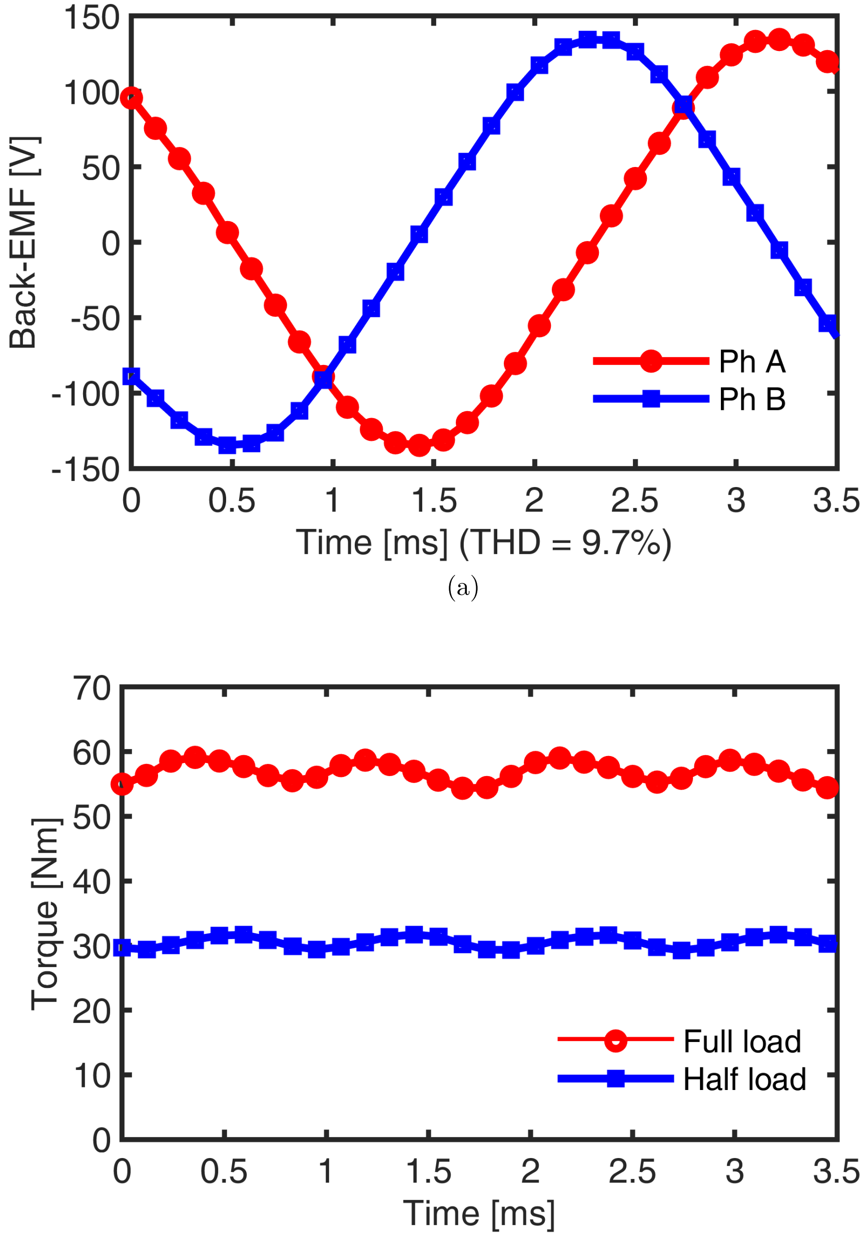

Figure 3.9: Three dimensional FEA results for the 16-slot 56-pole example machine: (a) open-circuit back-EMF, (b) torque with a pure q-axis current excitation. The back-EMF has low THD and the torque ripple is within 10% for both the half-load and full-load conditions.

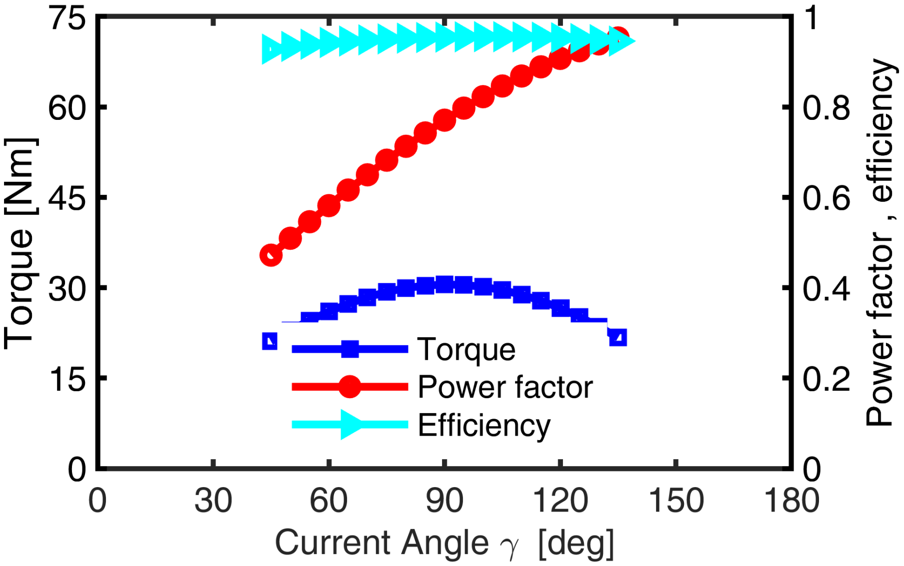

(a)

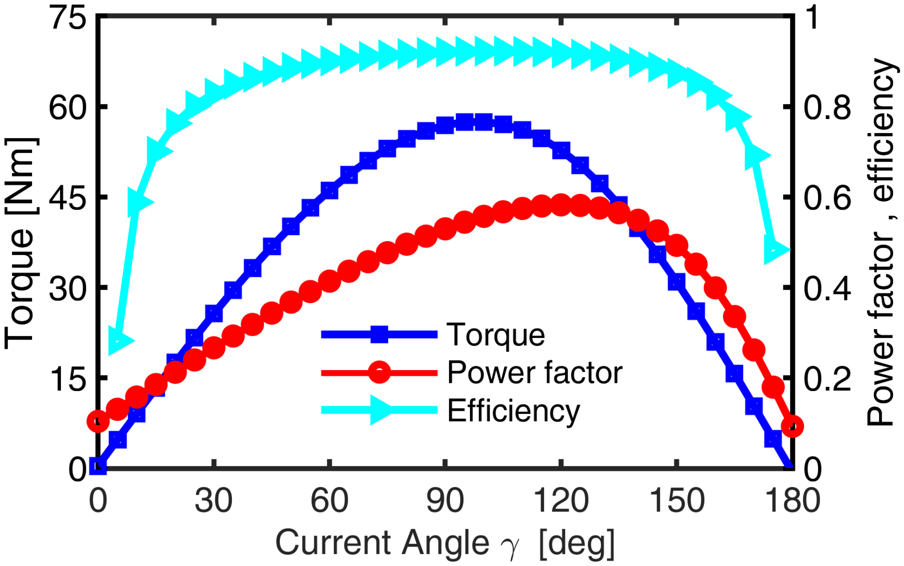

(b)

Figure 3.10: Three-dimensional FEA-predicted torque, power factor and efficiency at different current angles, (a) half-load condition, (b) full-load condition. Maximum torque per ampere is achieved at approximately 90 degrees, which indicates that the VTFM machine has very little saliency.

3.3.4 Steady-state operation in the fault modelling

Owing to the two-phase construction, the proposed vernier-type machines feature an inherent lack of mutual coupling between the two phases. This is verified by FEA results, as shown in Fig. 3.11a and Fig. 3.11b. In order to reduce the computation time and transients, a short-circuit fault during normal operation is simulated on Phase A by the injection of a pure demagnetizing current, while the current in phase B is maintained the same (Fig. 3.11a), and the changes in the phase voltages are observed. It is seen that the phase A voltage reduces to nearly zero due to the fault, while the phase B voltage remains virtually unchanged from the normal operating condition (Fig. 3.11b). This indicates that the phases are magnetically decoupled from each other, which would reduce the risk of the fault in one phase transmitting to the other. Complex 3D FEA models were used to demonstrate that the machine is superior in terms of fault tolerance

3.3.5 Peformance comparison with conventional axial-field PM machines

The performance of the VTFM PM machine is compared with that of a standard three-phase surface-mounted PM synchronous machine designed for solar car application [78] (Fig. 3.12). This baseline conventional machine has 36 stator slots and 12 rotor poles, featuring a single-stator single-rotor construction with distributed windings. The dimensions and specifications of the machines are summarized (Table 3.3).

The performance comparison between the vernier-type machine and the baseline conventional axial-field PM machine is also tabulated in Table 3.3. The airgap length

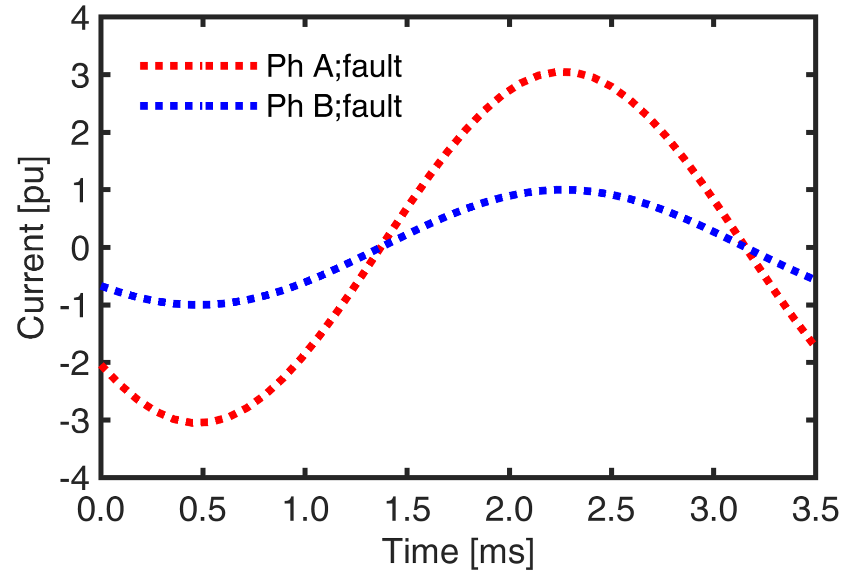

(a)

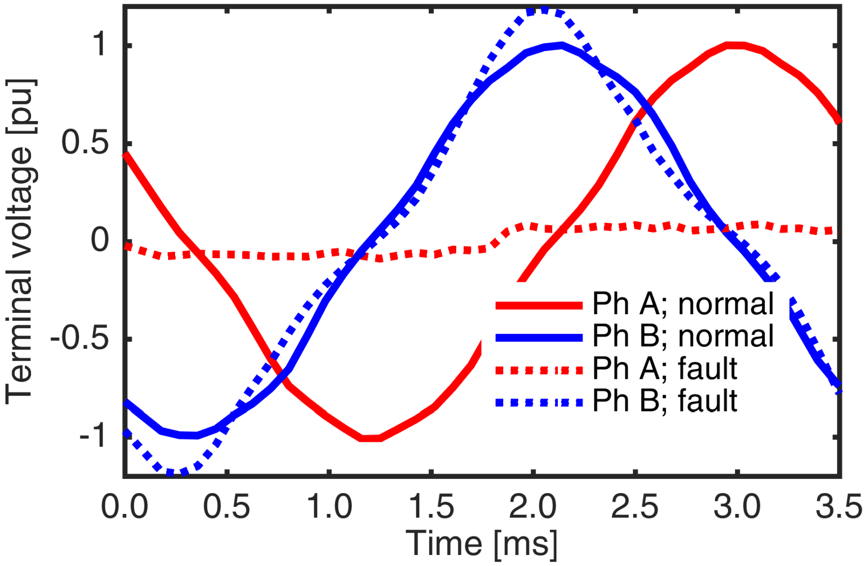

(b)

Figure 3.11: Demonstration of the magnetic independance of the two phases, (a) steady-state currents in p.u. during a short-circuit fault in phase A, (b) steady-state phase voltages in p.u. during the fault. Rated values are considered as the bases for the per-unitization. It is observed that the voltage in the healthy phase B shows very little change, in spite of the short-circuit fault in phase A.

of the baseline machine is modified on the fly to achieve field weakening and the torques at various airgap lengths computed by 3D FEA are shown (Fig. 3.13). In order to enable a basic comparison of electromagnetic performance, the baseline machine was simulated with an airgap length of 2.5mm. More elaborate systematic studies are beyond the space constraints and scope of this paper.

It can be observed that, in line with expectations from the qualitative explanations in the previous sections, the proposed machine can be designed with lower copper loss than the conventional machine. However, its core losses are substantially higher. This may be attributed to the multi-harmonic feature of the VTFM machines, and the greatly increased operating frequency for the same speed. This indicates that these machines are more suited for low-speed direct-drive type applications. The power factor is also lower than in the conventional machine, which emphasizes that the application for this type of machine is in the direct-drive applications, in which typically, the machine is substantially more expensive that the converter due to the large size.

It may be noted that a difference between the results from 3D and 2D FEA is observed, indicating that the 2D analysis performed at the mean diameter is not accurate enough for the analysis of this type of machine. This may be attributed to the significant saturation at the inner diameter. Optimization studies for this machine would therefore require 3D FEA.

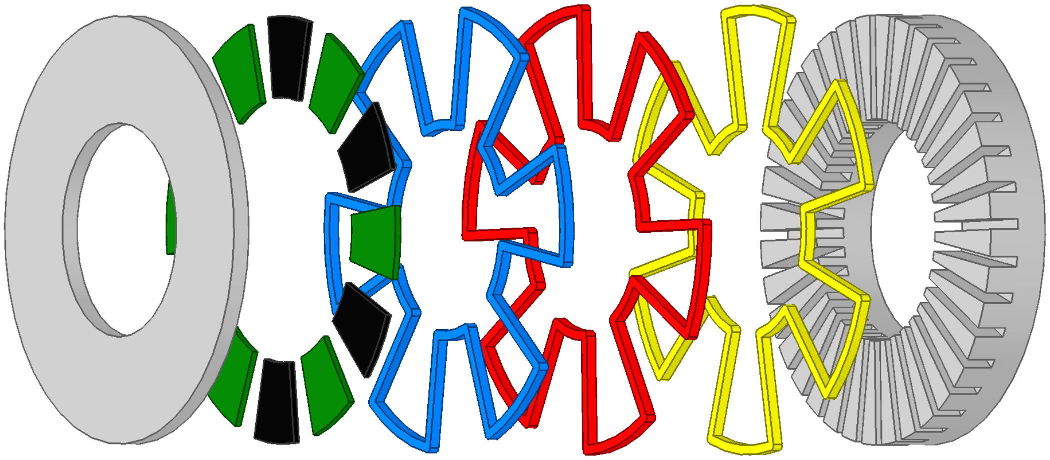

Figure 3.12: Exploded view for the baseline surface-mounted axial-field PM machine with 36 stator slots and 12 rotor poles. This machine employs wave type distributed windings.

Table 3.3: Specifications and calculated performance parameters of the studied VTFM machines, along with those of the baseline AFPM machine. All machines are designed to produce 56 Nm at 600 rpm, and have an active outer diameter and total axial length of 248 mm and 52.5 mm, respectively.

Machine	Baseline	VTFM 3D
Number of stator slots	36	16
Number of rotor poles	12	56
Number of auxiliary stator slots	-	2
Current density [A/mm2]	7.6	6.9
Copper loss [W]	419	263
Core loss [W]	13	54
Total loss [W]	432	317
Power factor	0.78	0.53
EM efficiency [%]	89	92
Magnet mass [kg]	0.365	0.536
Steel mass [kg]	6.16	5.49
Copper mass [kg]	2.17	2.17
Total mass [kg]	8.7	8.2

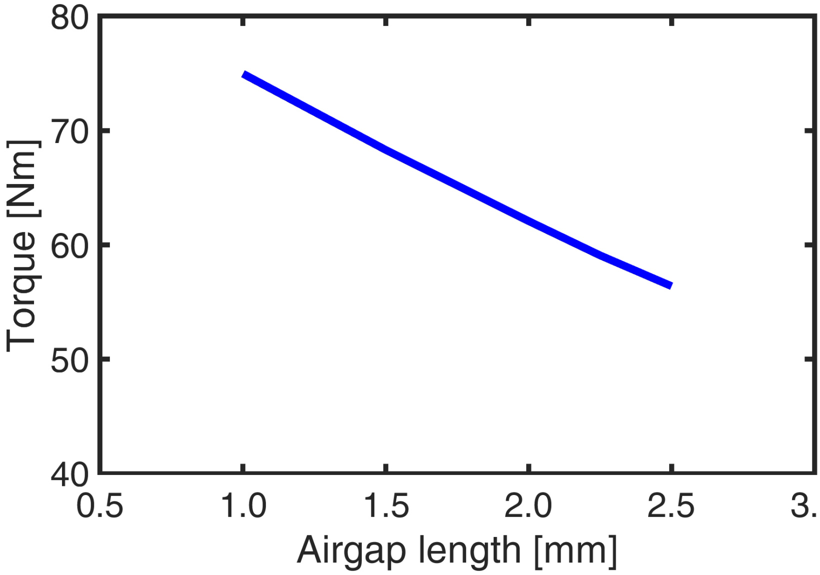

Figure 3.13: The variation of torque with airgap length for the baseline machine. The calculations in Table 3.3 are performed at an airgap of 2.5mm.

3.4 Large scale optimization study based on 3D FEA

The main example of novel MAGNUS axial flux motor considered in the current paper has 40 spoke rotor poles and a total of only 6 coils for the 3-phase stator. The rotor is of the spoke type and is placed in between two stators. One of the stators has a special profiled configuration and is “passive”, i.e. has no winding, an idea [79] inspired from previous work on a radial-airgap flux-reversal machine [80]. A large-scale optimization study, based on 3D FEA and employing a special optimization algorithm, has been conducted and results are discussed in order to provide new technical insights, including the effect of magnetic material characteristics and manufacturing techniques.

3.4.1 Topologies, new Variations, and parametric modeling

The novel topology under study has a central spoke-type PM rotor, a wound stator and a profiled stator and was originally proposed by our extend research group [81]. A 3-phase implementation with 40 rotor poles and only 6 coils is shown in Fig. 3.14a, which is highly advantageous in terms of manufacturing. The profiled stator has neither coils nor main slots. Shown in Fig.3.14b is a version with two wound stators.

Alternatively, the rotor can have surface mounted PMs. The stator windings can be distributed, fractional-slot concentrated or Gramme windings with 2, 3, or multiple phases. In both topologies, one of the stators is rotated by one rotor pole pitch relative to the other for higher torque capability and power factor.

The parametric 3D model has 13 geometric variables, including 7 in the axial direction, 4 in the circumferential direction and 2 in the radial direction (Fig 3.15a). The outer diameter (OD) and inner diameter (ID) of the stators and rotor are fixed to 250 mm and 150 mm, respectively, considering the dimensions of available laminated cores out of which the stators and rotor will be made. There are 11 independent geometric parameters in total for the optimization.

3.4.2 Sensitivity analysis

The design of experiments (DOE) based sensitivity analysis for total active material cost and total electromagnetic loss was performed to identify the key impacting geometric parameters and reduce the searching space. The independent geometric variables for the optimization are labeled in Fig. 3.15a. The mesh plot of the 3D FE

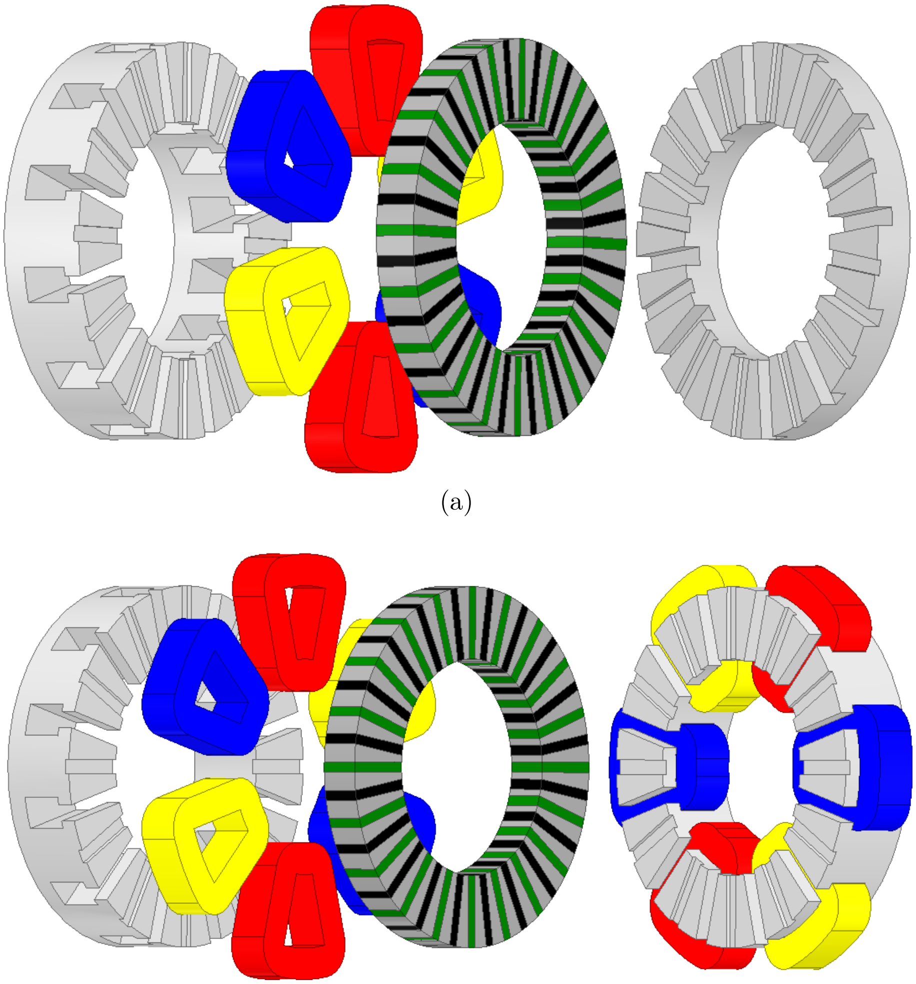

(a)

(b)

Figure 3.14: Exploded views of: (a) the studied vernier-type AFPM machine with one wound stator and one profiled stator, (b) the existing vernier-type AFPM machine with two wound stators. The presented topologies have 40 rotor poles and 12 main teeth, each with 2 auxiliary teeth. One of the stators is rotated relative to the other by one auxiliary tooth pitch to reduce flux leakage and enhance the torque.

model used for the calculation is shown in Fig. 3.15b [53]. The ranges of variables are determined by geometric constraints and manufacturing tolerances. The detailed independent variables and their ranges are tabulated in Table 3.4.

The influence of design variables on the total cost, loss and torque shown in Fig. 3.16. It illustrates the fact that the electromagnetic torque is mainly affected by the auxiliary teeth height k_{ath}, the main slot width k_{sw}, the wound stator back iron

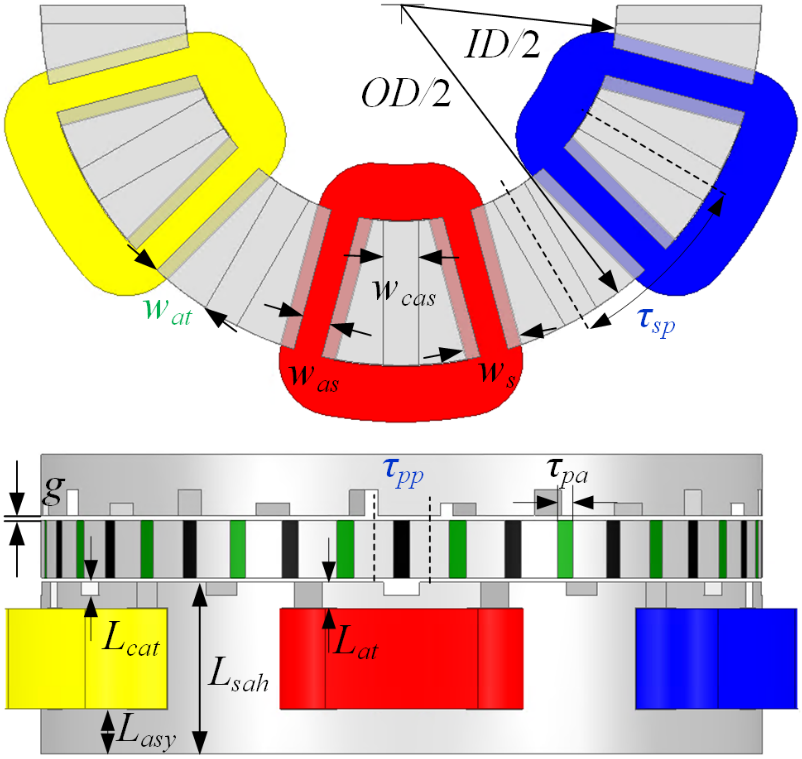

(a)

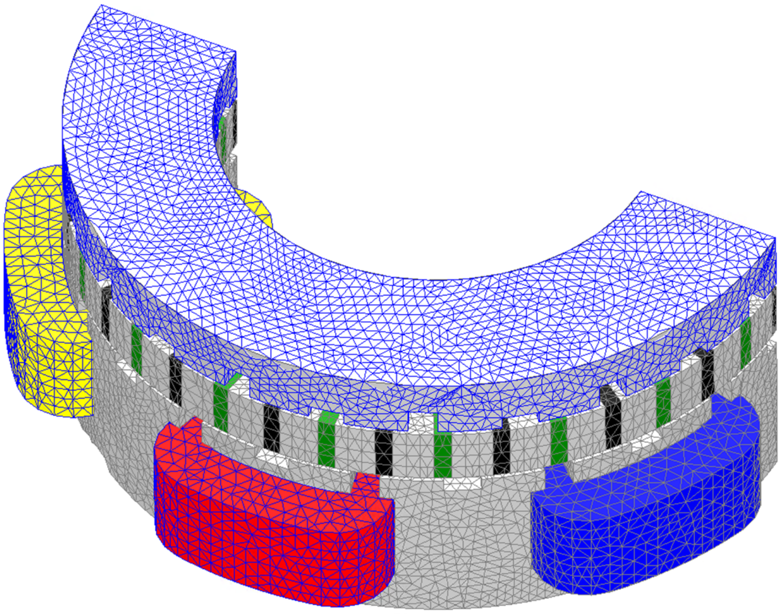

(b)

Figure 3.15: Parametric 3D models: (a) with variables labeled: dark blue–constants, dark green–dependent variables, black–independent variables. (b)FE mesh plot. A 1/2 model is analyzed to reduce the computational burden and there are in total 273,248 tetrahetral elements. Powerful workstations and high performance computing systems are employed in order to accelerate the electromagnetic FEA.

Table 3.4: Ranges and Explanations of Independent Geometric Variables.

Var.	Description	Min	Max
g	Airgap [mm]	1.50	3.00
L_{rt}	Rotor Length [mm]	20.0	35.0
L_{st}	Stator Length [mm]	45.0	60.0
k_{asy}	Wound stator back-iron = L_{asy}/L_{st}	0.20	0.35
k_{psy}	Profiled stator back-iron = L_{psy}/L_{asy}	0.80	1.20
k_{ath}	Auxiliary teeth height = L_{at}/L_{st}	0.40	0.60
k_{cath}	Auxiliary teeth center height = L_{cat}/L_{at}	0.20	0.50
k_{sw}	Slot width = τ_{sw}/τ_{sp}	0.40	0.70
k_{asw}	Auxiliary slot width = τ_{asw}/τ_{asw}	0.15	0.25
k_{casw}	Center auxiliary slot width = τ_{casw}/τ_{asw}	0.40	0.60
k_p	Pole arc ratio = τ_{pa}/τ_{pp}	0.50	0.65

thickness k_{asy}, the axial stator length L_{st} and the airgap length g. The main slot width k_{sw}, the wound stator back iron thickness k_{asy} and the axial stator length k_{st}, which are related to the coil size, are the main impacting factors of torque.

Most of the independent variables can affect the total loss except the auxiliary teeth central height k_{cath}, the central auxiliary slot width k_{casw} and the pole arc ratio k_p. The auxiliary teeth center height k_{cath} and center auxiliary slot width k_{casw} have very small impacts on the cost, loss and torque, and are expected to be removed from the independent variable list for optimization.

3.4.3 Design optimization

The total active material cost and total magnetic loss are selected as the two optimization objectives considering the designed motors are for low-speed direct-drive applications. The current density is adjusted to produce the rated torque 71 Nm at 300 r/min for all the evaluated designs. The slot fill factor is assumed 0.5 for the non-overlapping winding configuration. The optimization problem is formulated as:

$$\text{min:} \begin{cases} f_1(\mathbf{x}, J) & = P_{Cu} + P_{Fe}, \\ f_2(\mathbf{x}, J) & = C_{Fe} m_{Fe} + C_{Cu} m_{Cu} + C_{pm} m_{pm}, \end{cases} \tag{3.15}$$

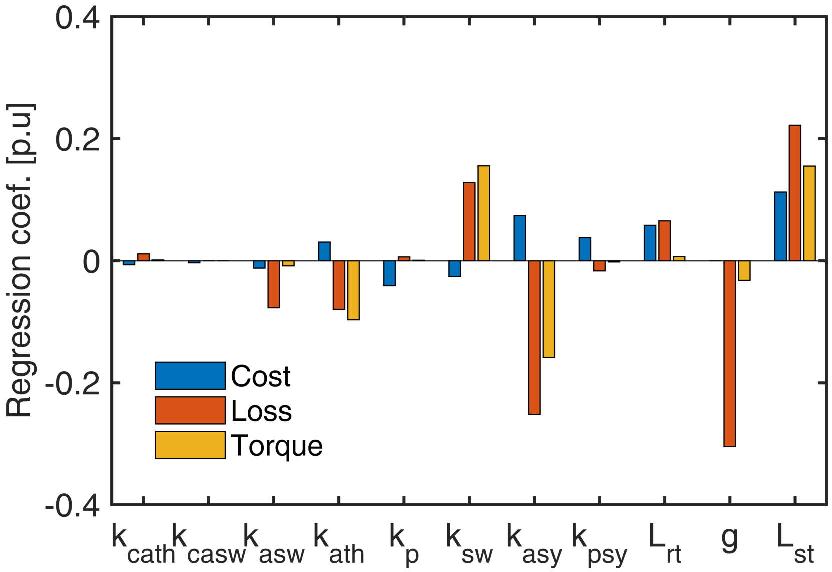

Figure 3.16: Sensitivity analysis results.

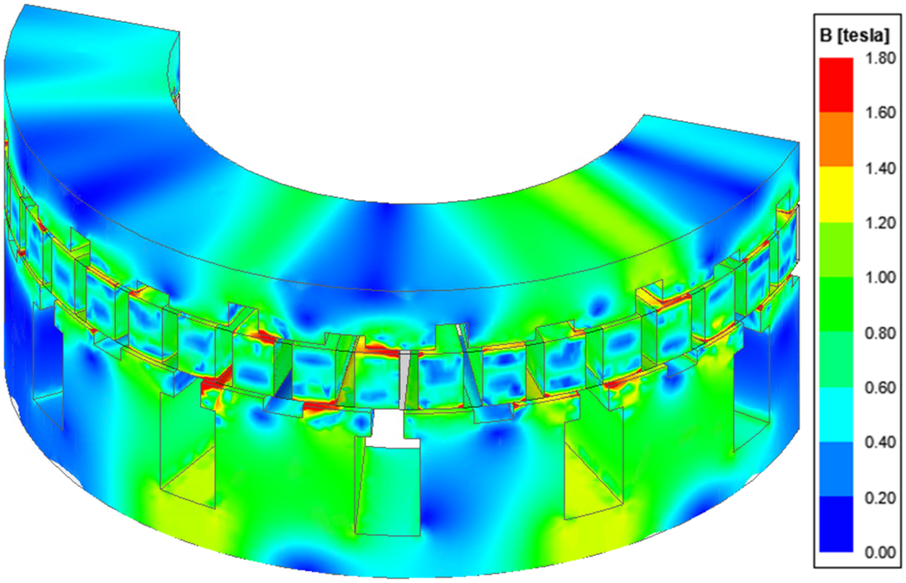

Figure 3.17: Flux density map in stator and rotor cores.

where $\mathbf{x}$ is the geometric variable vector, whose ranges have been tabulated in Table 3.4, and J the current density. P_{Cu} and P_{Fe} are dc copper loss (joule loss) and core loss, respectively. m_{Fe}, m_{Cu}, and m_{pm} denote the mass of steel, copper, and magnet in kilograms, respectively. The per unit price of steel, copper, and magnet are denoted by C_{Fe}, C_{Cu}, and C_{pm}, respectively.

In the optimization process, a variant of the two-level surrogate-assisted multiobjective optimization algorithm, which combines the differential evolution (DE) algorithm with Kriging models, is employed to reach the Pareto front by evaluating less than two hundred 3D designs [58].

3.4.4 Results and discussion

The performance of two optimal AFPM machines, one with a wound stator and a profiled stator, and the other with two wound stators is tabulated in Table 3.5. The total axial length of the selected machines are 104 mm and 143 mm, respectively. The flux density map for the selected design with one wound stator and one profiled stator is illustrated in Fig. 3.17. It is shown that the studied vernier-type AFPM machine with one wound stator and one profiled stator have an advantage over the existing one with double wound stators in terms of both the cost and total electromagnetic loss.

The impact of the stator lamination material on the optimization results is also studied. Commonly-used silicon steel M43, M19, M15 and M10 of the same gauge are used in the optimization, as shown in Fig. 3.18. The comparison of the three Pareto fronts shows that by using M10, the lowest loss can be achieved but the cost

Table 3.5: Performance of Selected Pareto Front Design Examples for the Studied and Existing Vernier-type AFPM Machine Topologies.

Number of wound stators	One	Two
Total loss [W]	154	177
Copper loss [W]	117	128
Core loss [W]	37	49
Current density [A/mm^2]	4.5	3.3
Efficiency [%]	93.5	92.6
Cost [c.u]	73	98

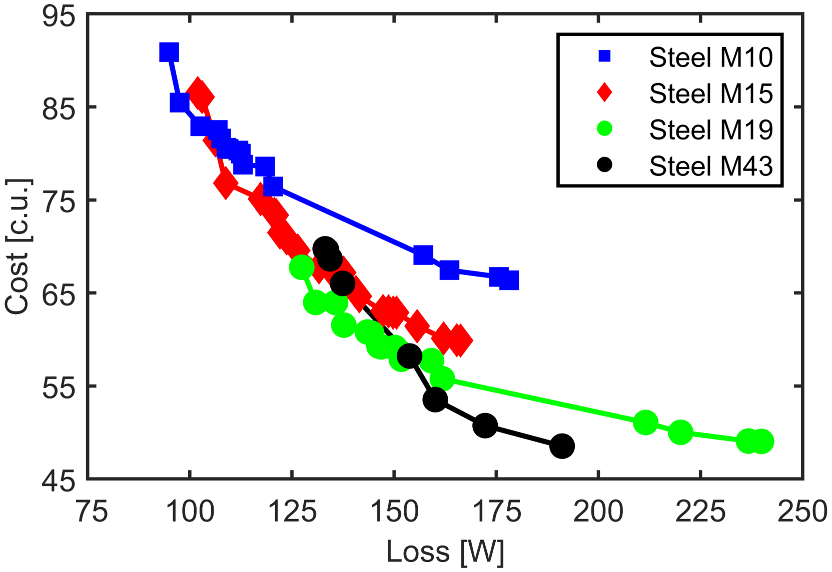

Figure 3.18: Pareto fronts for machines using M10, M15, M19 and M43.

will increase. If cost reduction is more important, then M43 is more suitable.

The ratios between the copper loss and the total loss for all the FE-evaluated designs are as shown in Fig. 3.19a, the copper loss is the dominating loss component in the designed machines for low-speed application, which is in line with the expectation. In addition, the torque ripple of Pareto front designs is within 15%, as shown in Fig. 3.19b.

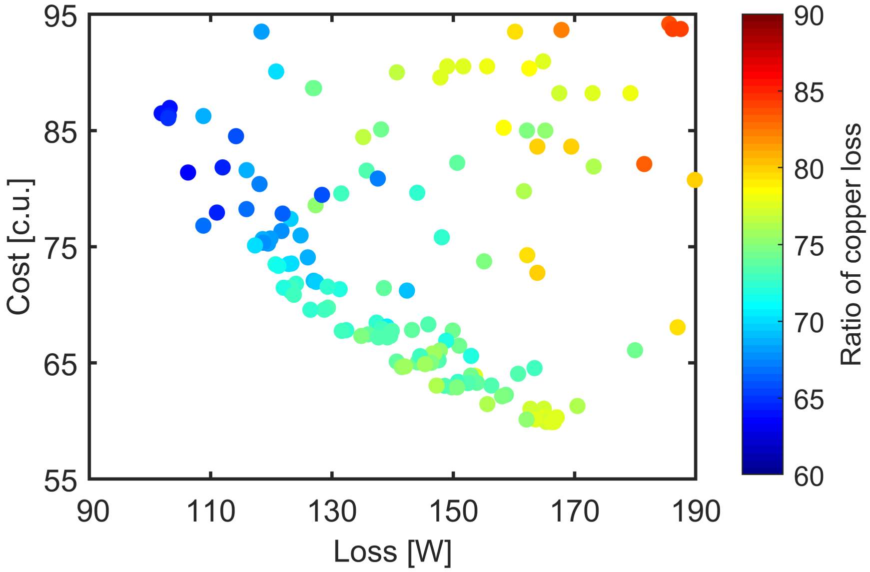

(a)

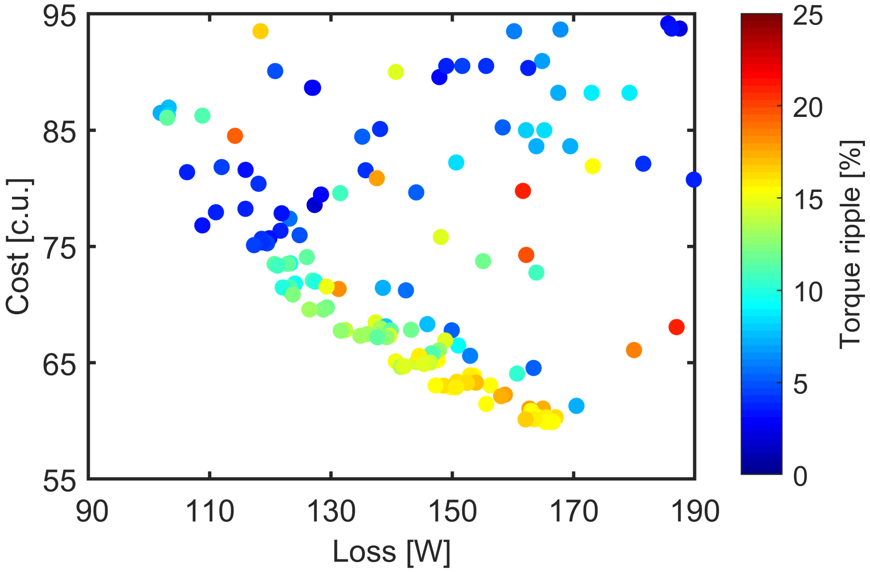

(b)

Figure 3.19: Multi-objective optimization results for cost and loss for designs using M15 and with color maps for: (a) ratio of copper loss to the total loss, (b) torque ripple.

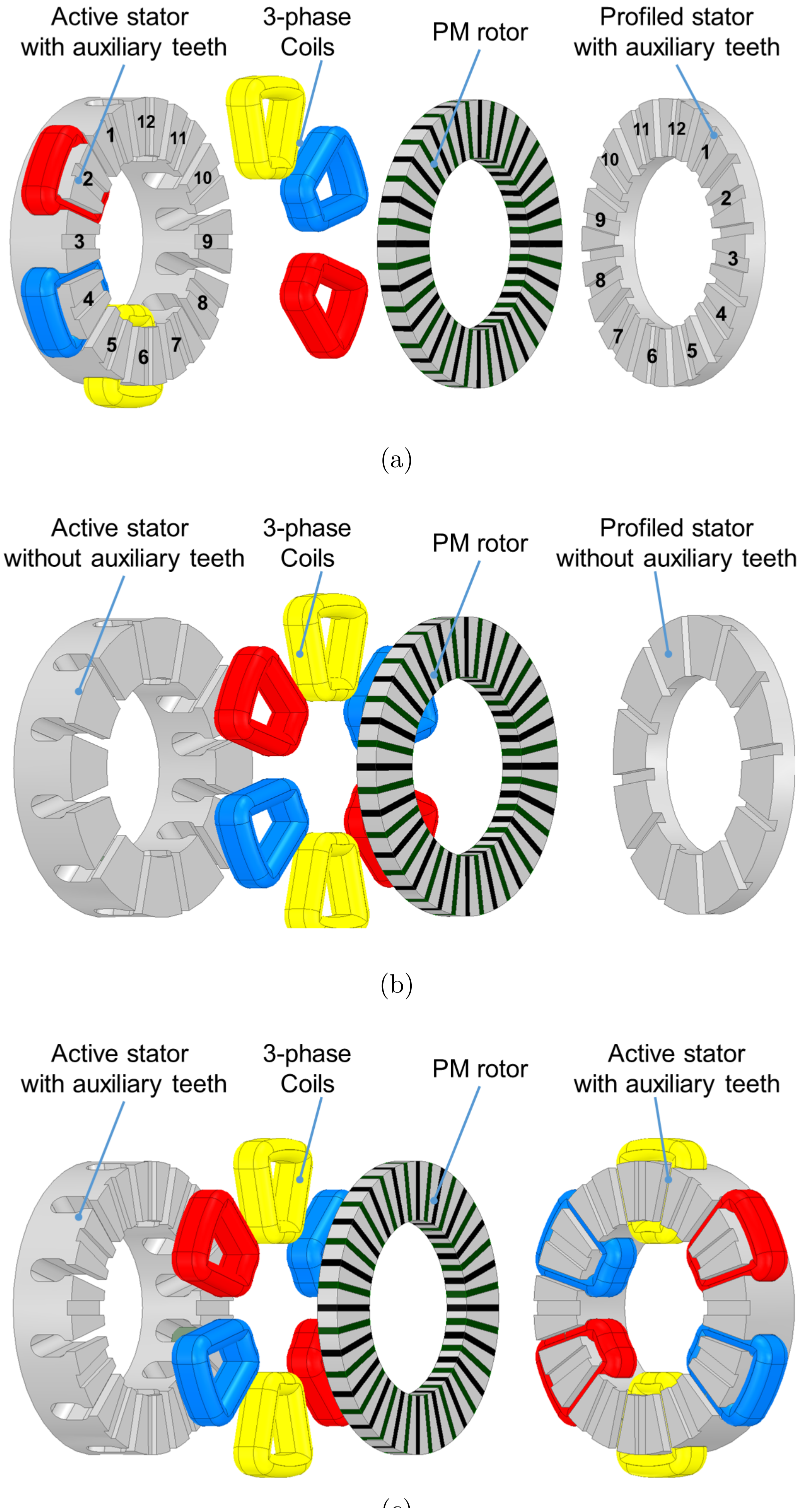

Figure 3.20: Exploded view of proposed topology versions of vernier-type AFPM machine of the MAGNUS type (a) one wound stator and one profiled stator, (b) one wound stator and one profiled stator but no auxiliary teeth, (c) two wound stators.

3.5 Detailed Analysis for Torque Production

3.5.1 Torque contribution by rotor and stators

The torque contribution of each stator and rotor components has been examined by integrating the tangential component of the Maxwell Stress Tensor over the component surfaces using:

$$f_t(t,\theta) = \frac{B_a(t,\theta)B_t(t,\theta)}{\mu_o} \tag{3.16}$$

where $B_a(t,\theta)$ and $B_t(t,\theta)$ are the axial and tangential flux densities calculated by FEA. The tangential force on the individual stator teeth and rotor components can be evaluated by integrating the stress over the corresponding mechanical components as follows:

$$F_t = \int\limits_S f_t(t,\theta)\,dS. \tag{3.17}$$

Torque breakdown for the studied MAGNUS machine calculated from this approach is illustrated in Fig. 3.21 and shows that the active stator produces almost twice the torque than the profiled stator without winding. In the rotor, the average torque is almost equally distributed over the rotor components. The torque generated by each PM and rotor ferromagnetic pole (FP) is 1.2 Nm and 0.6 Nm, respectively. The sum of the torque by all rotor components is 71.0 Nm.

Contributions of the stator teeth are listed in Table 3.6. The teeth surrounded by coils are numbered with even numbers and are the main contributors to torque production. The profiled stator tooth labeled by odd numbers only generates a low

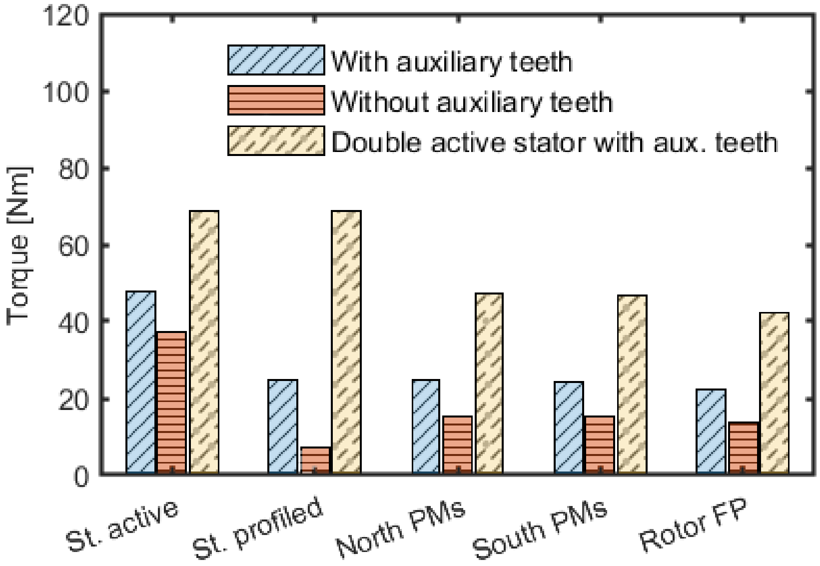

Figure 3.21: Torque breakdown in motor components for the studied three topologies.

and negative torque. Most flux lines are passing through stator teeth labeled by even numbers as shown in Fig. 3.22.

Two other topologies shown in Fig. 3.14(b) and Fig. 3.14(c) have also been modeled. Their torque breakdowns are also illustrated in a way similar to the studied MAGNUS machine in Fig. 3.21. It is shown that auxiliary teeth increase the torque production by introducing additional torque-contributing harmonics and reduce flux leakage. Torque waveforms of the models are demonstrated in Fig. 3.23, showing relatively low torque ripple.

Table 3.6: Individual torque contribution by each stator tooth.The teeth labeled even number contribute higher torque than odd number.

Components	Torque [Nm]
Active stator odd teeth (1, 3, 5, 7, 9, 11)	0.6
Active stator even teeth (2, 4, 6, 8, 10, 12)	7.4
Profiled stator odd teeth (1, 3, 5, 7, 9, 11)	-0.4
Profiled stator even teeth (2, 4, 6, 8, 10, 12)	4.2

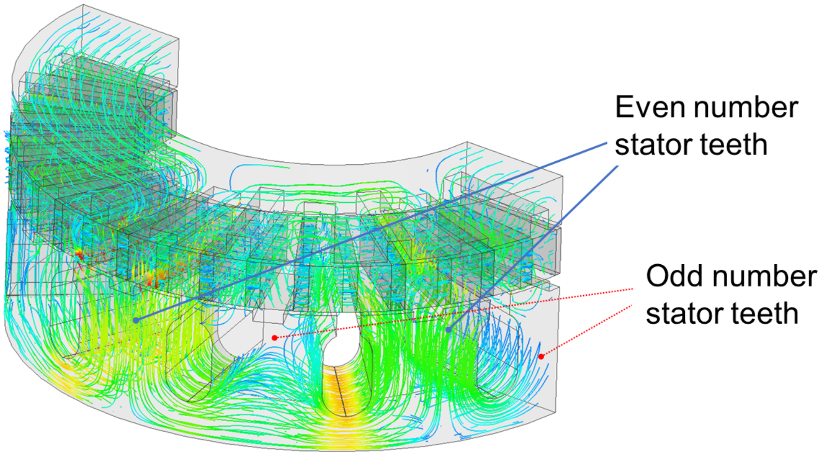

Figure 3.22: Magnetic flux for a 3-D FE model. Only half of the machine was modeled to reduce the computational burden. There are in total 990,154 tetrahedral elements. The presented topology has 40 rotor poles and 12 main teeth, each with 2 auxiliary teeth. One of the stators is rotated relative to the other by one rotor pole pitch.

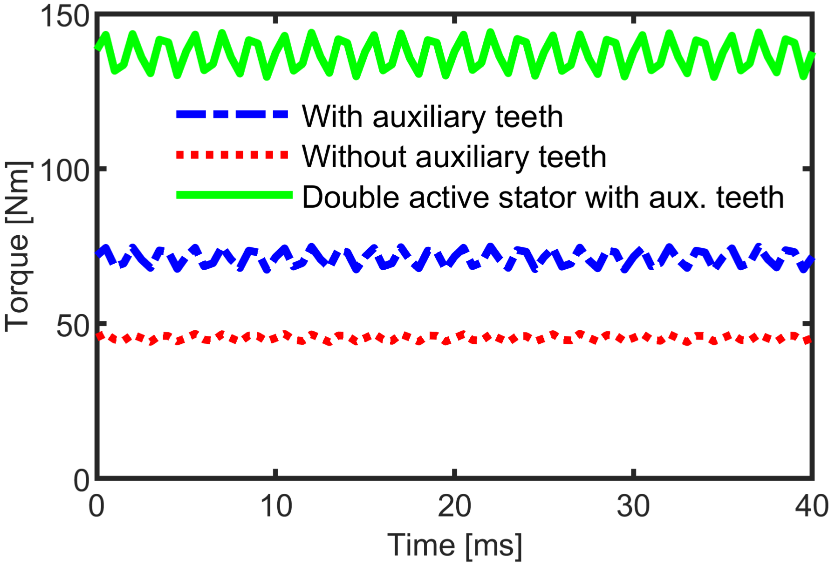

Figure 3.23: Torque wave-forms for the 3 topologies shown in Fig. 1. relatively low torque ripple can be observed for the three models.

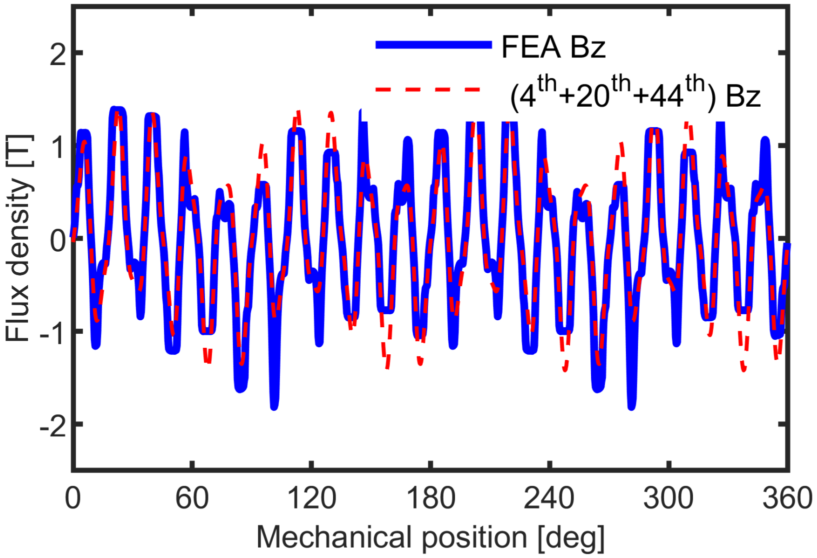

(a)

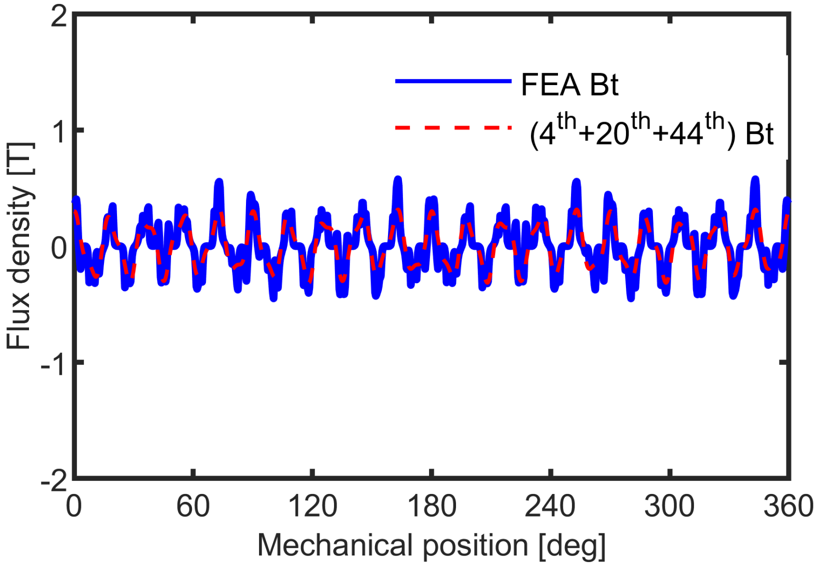

(b)

Figure 3.24: Analysis of air-gap flux density distribution in the air-gaps. (a) 3-D FEA predicted axial flux density for the air-gap between active stator and rotor at median diameter, (b) 3-D FEA predicted tangential flux density for the air-gap between the active stator and rotor at median diameter

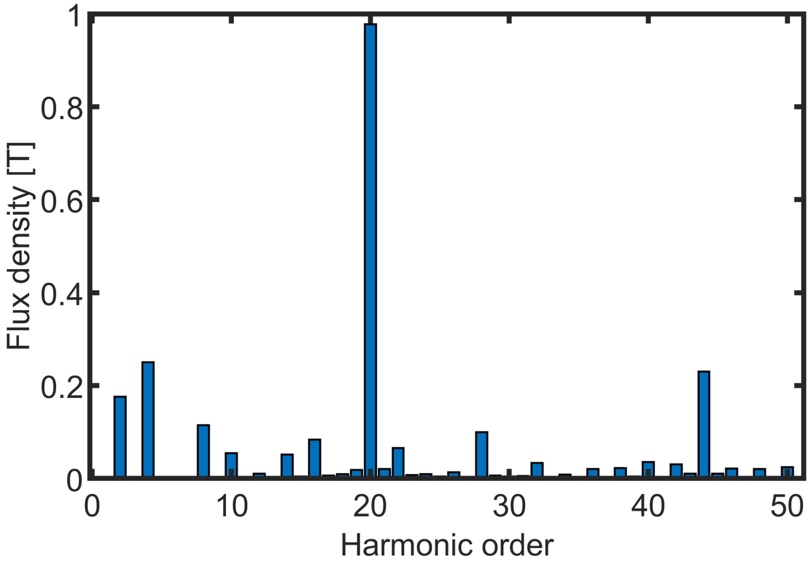

(a)

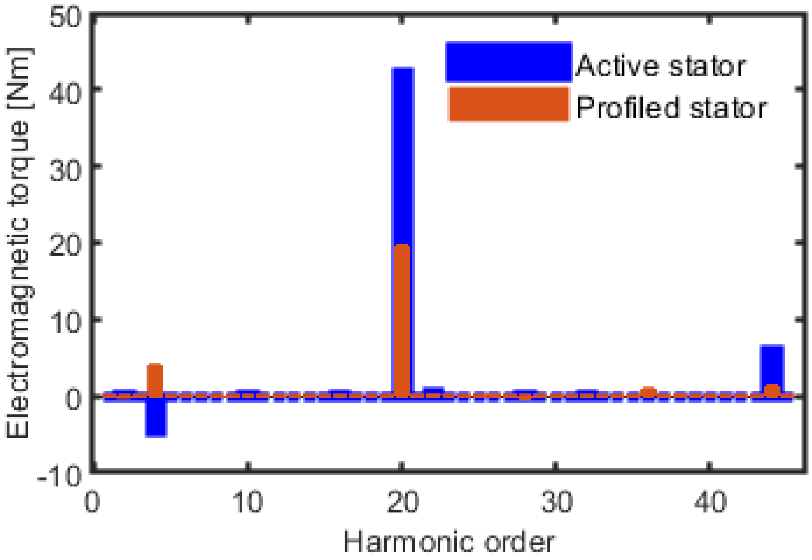

(b)

Figure 3.25: Harmonic torque production in the air-gaps. (a) Amplitude spectrum of the axial component of the air-gap flux density and (b) torque contribution of corresponding harmonics for each air-gaps.

3.5.2 Harmonic-based torque decomposition

In AFPM machines, the air-gap flux density has two main components, one in the axial- and the other in the tangential direction. These two components of the air gap flux density distribution at an arbitrary rotor position are obtained from 3-D FEA. The air-gap flux density can be decomposed into a series of harmonics. With the air-gap flux density harmonics, the torque contributed by each harmonic is obtained by:

$$T = r^2 L_{stk} \iint \frac{B_a B_t}{\mu} \mathrm{d}\theta, \tag{3.18}$$

$$T = \sum_k \left(\frac{D_r}{2}\right)^2 L_{stk} |{B_a}^k| |{B_t}^k| \cos({\theta_a}^k - {\theta_t}^k), \tag{3.19}$$

where D_r is the average diameter of the rotor, L_{stk} is the radial stack length of rotor, k is harmonic number, B_a and B_t are the axial and tangential components of flux density in air-gap, respectively.

The axial and tangential components of flux density in the air-gap between the active stator and rotor at the average diameter are extracted from FEA and plotted as shown in Fig. 3.24(a) and Fig. 3.24(b). The harmonic spectrum of the axial component waveform, illustrated in Fig. 3.25(a), shows that only the harmonics of 8, 40, and 88 poles,respectively are substantial and their amplitudes are larger than 0.2T. The reconstructed air-gap flux density waveforms considering the three substantial harmonics are also plotted in Fig. Fig. 3.24(a) and Fig. 3.24(b). Torque contributions by 40 pole harmonics are of the largest value in both air-gaps. The 8-pole and 88-pole harmonics can also produce synchronous torque. The torque from

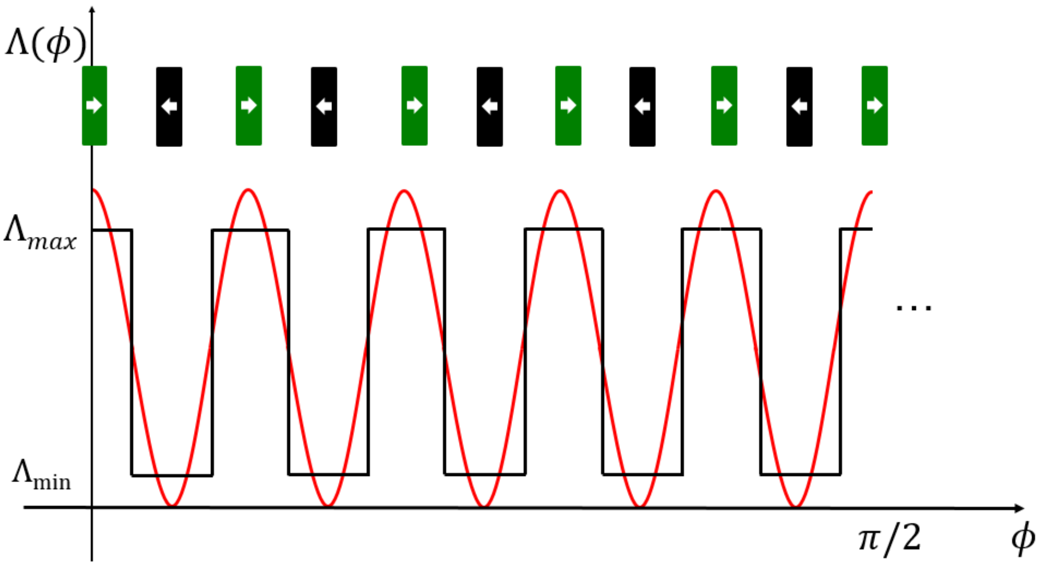

Figure 3.26: The air-gap permanence function is modeled as a square-waveform.

the profiled stator side is about half of the active stator side as shown in Fig. 3.25(b).

3.5.3 Analytical developments

In this section, the analytical air-gap flux density and corresponding torque equations are deduced. The air-gap PM-MMF under open circuit condition is:

$$F_{PM}(\phi') = F\frac{1}{2h+1}\sin[(2h+1)p_m\phi'], \tag{3.20}$$

where $(2h+1)p_m$ is the PM pole-pair number.

The air-gap permeance is modeled as a square wave as seen in Fig. 3.26 and expressed by:

$$\Lambda(\phi) = \frac{\Lambda_{max}+\Lambda_{min}}{2} + \frac{\Lambda_{max}-\Lambda_{min}}{2}\cos[N_{ST}(\phi-\phi_0)] \tag{3.21}$$

where N_{ST} is number of stator teeth.

The angular positions in the rotor and stator reference frames are related to each other by:

$$\phi = \phi' + \theta_r = \phi' + \theta_{r0} + \omega_r t \tag{3.22}$$

where θ_r is the rotor angle relative to the stator, $\omega_r t$ the rotor speed and θ_{r0} the initial position of rotor with reference to the stator (Fig. 3.27). The open-circuit air-gap flux density $B_{PM}(\phi)$ can be obtained by multiplying $F_{PM}(\phi)$ and $\Lambda(\phi)$ from (5) and (6):

$$\begin{aligned}
&B_{PM}(\phi) = F_{PM}(\phi) \cdot \Lambda(\phi) = \\
&= F_{PM}\frac{1}{2h+1}\sin[(2h+1)p_m\theta_{r0} + (2h+1)p_m\omega_r t]\cdot \\
&\cdot\left(\frac{\Lambda_{max}+\Lambda_{min}}{2} + \frac{\Lambda_{max}-\Lambda_{min}}{2}\cos[N_{ST}(\phi-\phi_0)]\right) = \\
&= F_{PM}\frac{1}{2h+1}\frac{\Lambda_{max}+\Lambda_{min}}{2}\cdot\sin[(2h+1)p_m\theta_{r0} + (2h+1)p_m\omega_r t] \\
&+\frac{F_{PM}}{2}\frac{1}{2h+1}\frac{\Lambda_{max}-\Lambda_{min}}{2}\cdot\sin[(2h+1)p_m(\theta_{r0}+\omega_r t) + N_{ST}(\phi-\phi_0)] \\
&+\frac{F_{PM}}{2}\frac{1}{2h+1}\frac{\Lambda_{max}-\Lambda_{min}}{2}\cdot\sin[(2h+1)p_m(\theta_{r0}+\omega_r t) - N_{ST}(\phi-\phi_0)]
\end{aligned} \tag{3.23}$$

The armature air-gap flux density B_{AR} can be obtained with same approach and employed for the derivation of electromagnetic torque analysis T_{em} as follow:

$$\begin{aligned}
T_{em} &= \frac{\partial W_{co}}{\partial \theta_r} = \frac{\partial}{\partial \theta_r}\int_V \frac{B(\phi,t)^2}{2\mu}\,dv = \\
&= \frac{D_r g L_{stk}}{4\mu}\frac{\partial}{\partial \theta_r}\int_0^{2\pi}(B_{PM}(\phi,t) + B_{AR}(\phi,t))^2\,d\phi,
\end{aligned} \tag{3.24}$$

where D_r is the average diameter, g is air-gap, and L_{stk} is radial stack length.

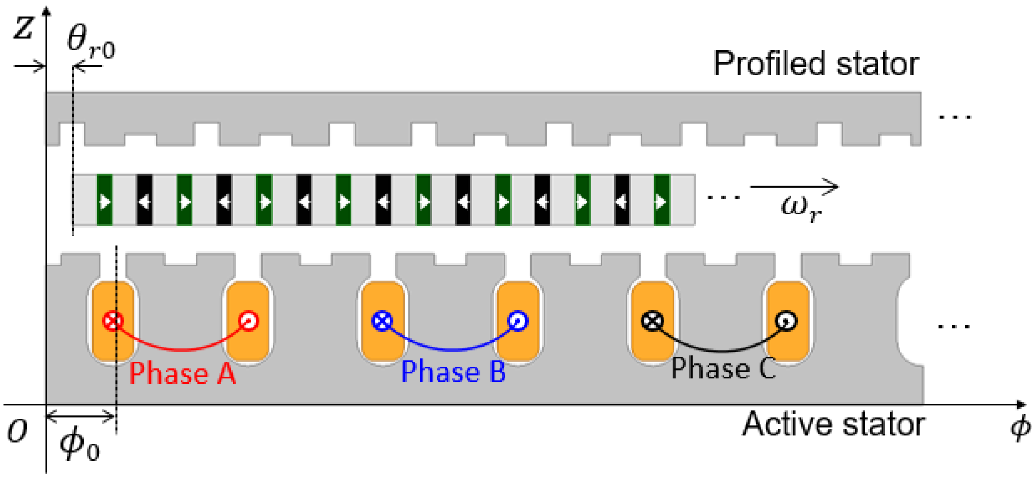

Figure 3.27: The coordinate system used for the theoretical analysis. The MAGNUS machine with one active stator and one profiled stator is modeled in 2-D.

3.5.4 Advantages of auxiliary teeth

In the proposed topology, there are two auxriliary teeth on each main stator teeth.The function of which is to enhance the high-polarity component of the stator magnetomotive force interacting with the rotor to produce a net torque. It is shown that auxiliary small teeth included in the stator main teeth yield a significant increase in the output torque and that the profiled stator has a lower contribution than the active stator to the total torque. The effect of the auxiliary teeth on increasing the torque output by approx. 61% has also been identified.

3.6 Prototyping and Experimentation

One of the optimal design from the Pareto front for M15 steel has been selected and prototyped. To simplify the fabrication of the high-polarity spoke-type PM rotor, the rotor poles between the magnets may be made from as single non-laminated steel pieces, which unavoidably reduces the torque and increases the rotor core loss [63].

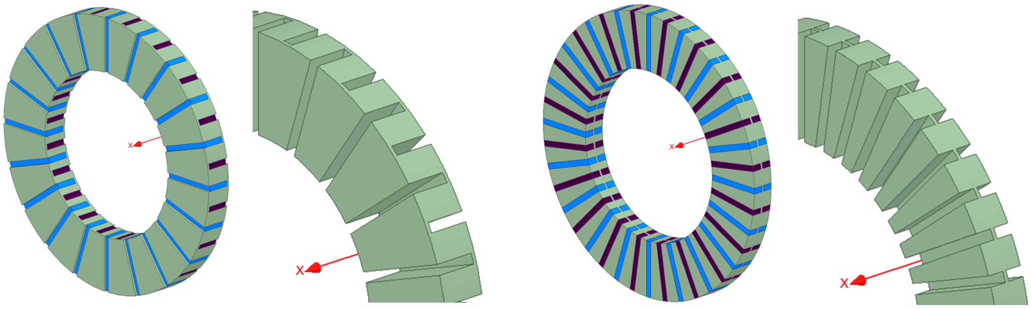

(a) (b)

Figure 3.28: Practical rotor designs for prototype manufacturing, (a) laminated rotor core with alternate single-sided bridge, (b) laminated rotor core with middle bridge.

Calculation based on the selected optimal design shows the rotor core loss will be increased to 38 W by a solid pole construction. Laminated steel exhibits only 3 W rotor core losses.

To maintain the optimized performance, a new rotor manufacturing procedure is proposed. The rotor is made from a laminated ring by machining a number of slots on the surfaces close to the airgap. To achieve enough rigidity and ease the insertion of magnets, two practical rotor implementations are considered, as illustrated in Fig. 3.28. The stators are also made from laminated rings by machining off the slot regions. To protect the laminated ring during the machining process, a sacrificial case is used, as shown in Fig. 3.29.

The stator and rotor cores were fabricated using laminated M15_29G steel rings to provide optimal performance. Solidworks was used to draw parts of the 3D model machine, which were then utilized in the prototyping process. The detailed drawings of active (Figs:3.30-3.31) and passive stator (Figs:3.32-3.33) can be observed. The machined active stator core and the surface-treated version can be seen in Fig. 3.34. Each tooth is wounded with coils in the active stator providing opportunities

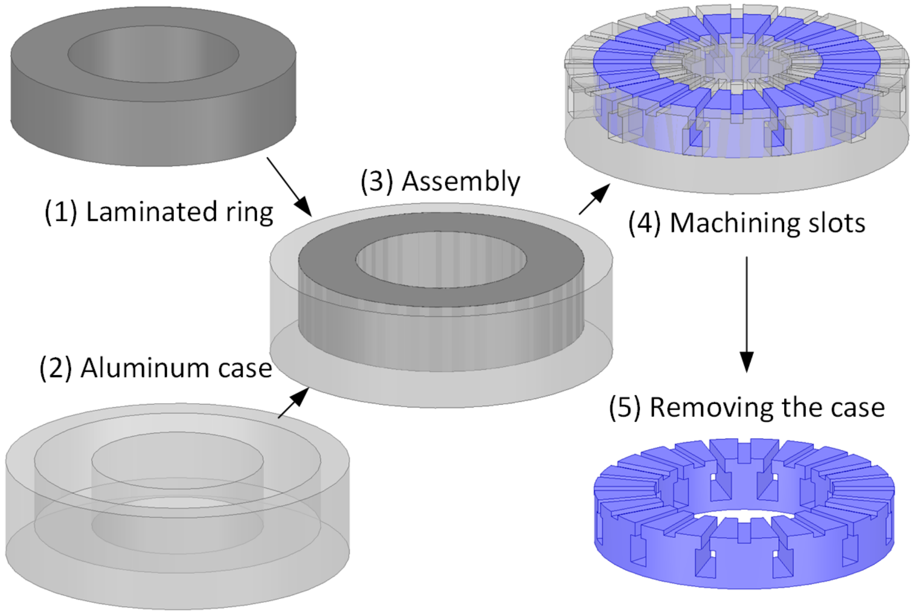

Figure 3.29: Fabrication of the laminated stator for the topology with one wound stator and one profiled stator.

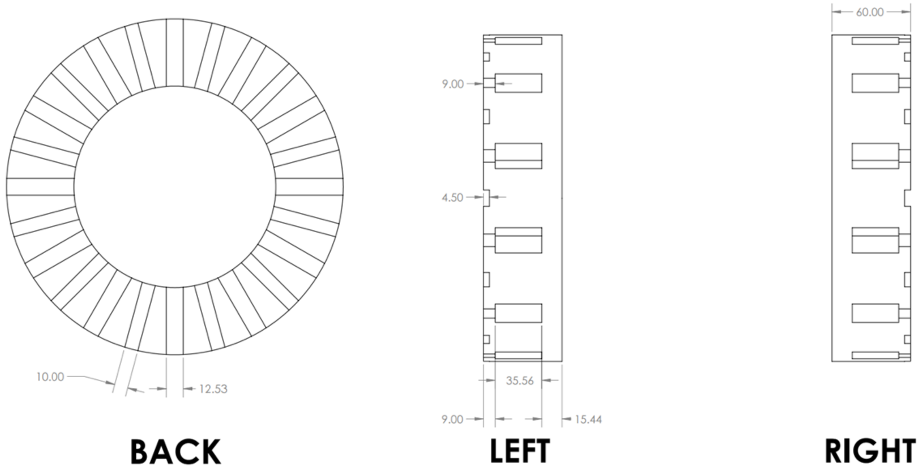

Figure 3.30: Active Stator left and right.

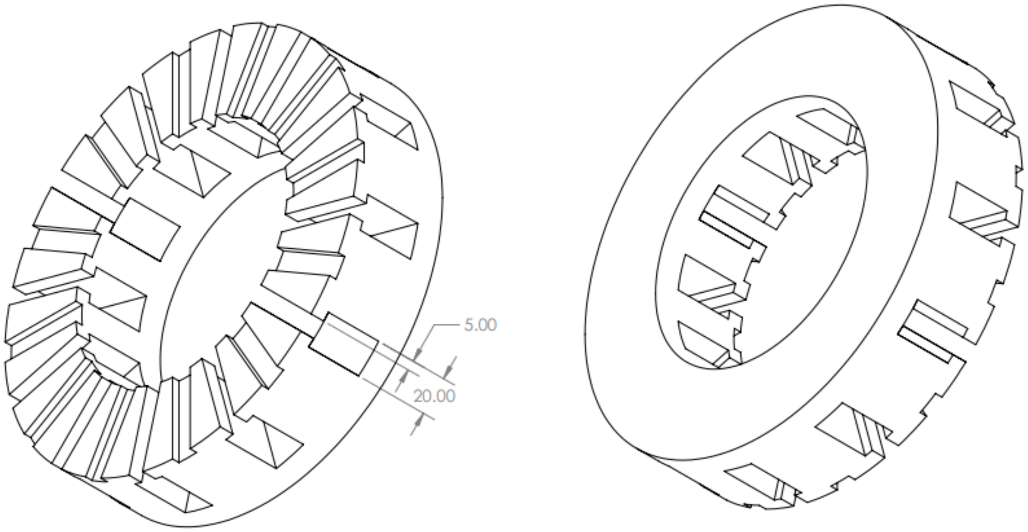

Figure 3.31: The active Stator.

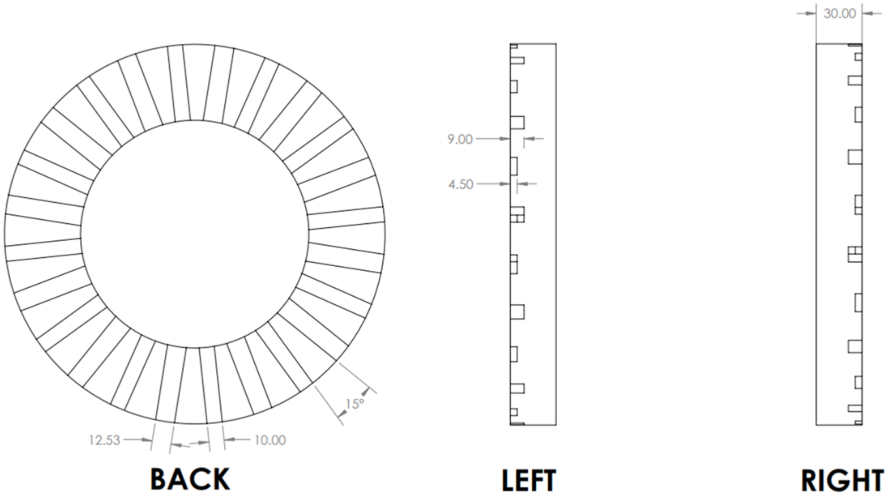

Figure 3.32: Passive stator left and right.

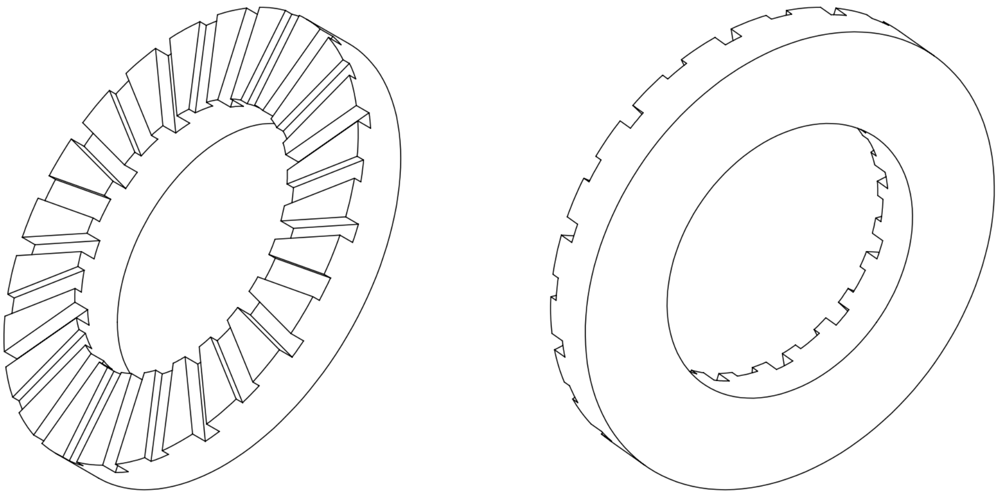

Figure 3.33: Passive stator.

to perform experimental studies with different winding configuration. The active stator with coils and profiled stator are shown in Fig. 3.35. The 40-pole rotor is manufactured and assembled with stators.

The conditions of the experiment and simulation were set to have comparative studies, with two phases and a magnetic airgap of 7mm between the rotors in an open-circuit configuration. A prime mover was then attached to the machine's shaft and used to rotate the machine up to a speed of 3050rpm. An oscilloscope was used to record the induced back emf in one of the phases and compared to the simulated results (Fig. 5.25). A fast Fourier transform was conducted on both the experimental and simulated back EMF to evaluate the magnitude of the fundamental and harmonic components.

The CAD drawing of the proposed test fixture for experimentation can be seen in Fig.3.36. By adjusting the distance between the adapter plate and the cylindrical

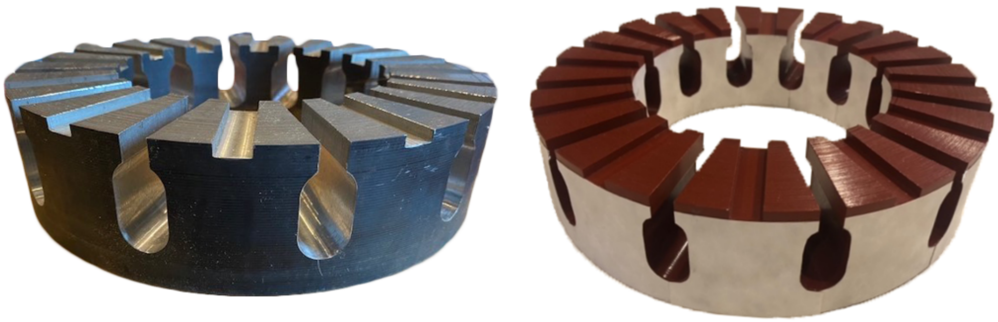

Figure 3.34: Active stator core machined from a laminated steel ring, before surface treatment.

spacer, the test procedure can be conducted with various air-gap lengths. The experimental setup involving the MAGNUS machine is visible in Fig. 3.37. The machine is connected to a prime mover using a shaft extension and a u-joint, which allows for misalignment between the shafts. The prime mover was then affixed to the machine's shaft and used to rotate the machine at a speed of 300rpm. An oscilloscope was used to record the induced back electromotive force (emf) in one of the phases, which was subsequently compared to the simulated results presented in Fig3.38.

3.7 Conclusion

Conventional high-polarity PM synchronous machines, which require a large number of stator slots and coils, these machines can achieve high electrical frequency with very few stator coils and teeth, leading to simplification of the construction and manufacturing under certain conditions. The machines also can be constructed with three or two phases, in which case they inherently exhibit high tolerance to faults due to the combined effect of a lack of coupling between phases and a relatively large

Figure 3.35: The prototyped profiled stator core and active stator wound with coils.

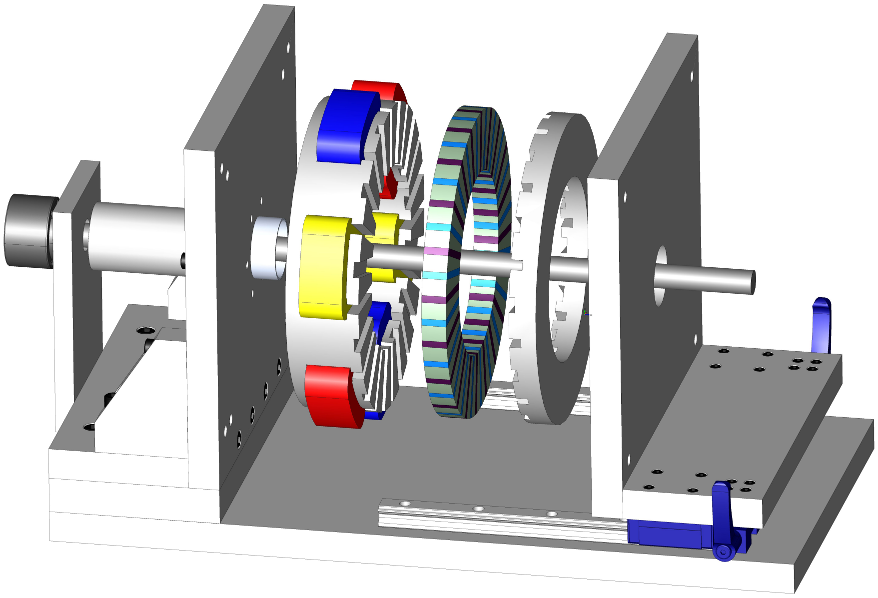

Figure 3.36: Exploded view of the computer-aided design (CAD) model for the MAGNUS motor on a testing fixture.

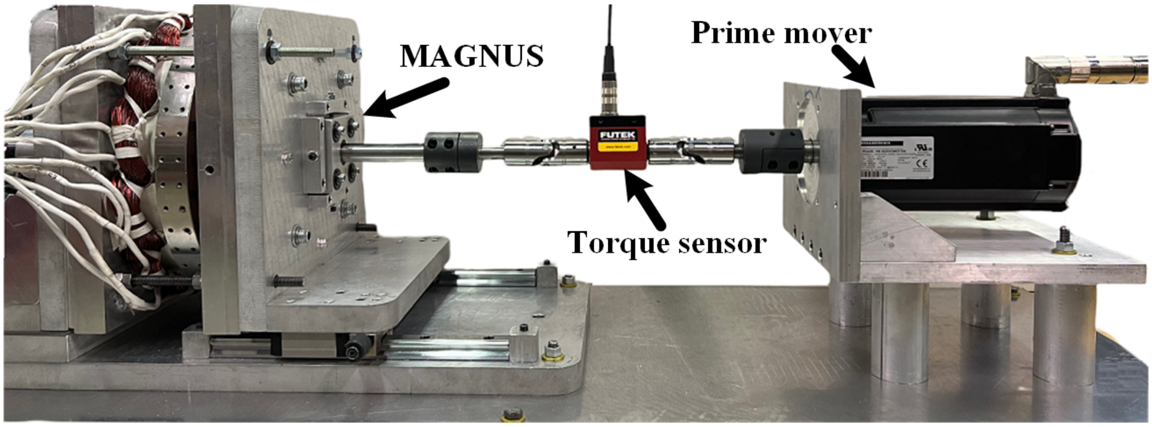

Figure 3.37: Prototyped MAGNUS motor on the experimental test fixture.

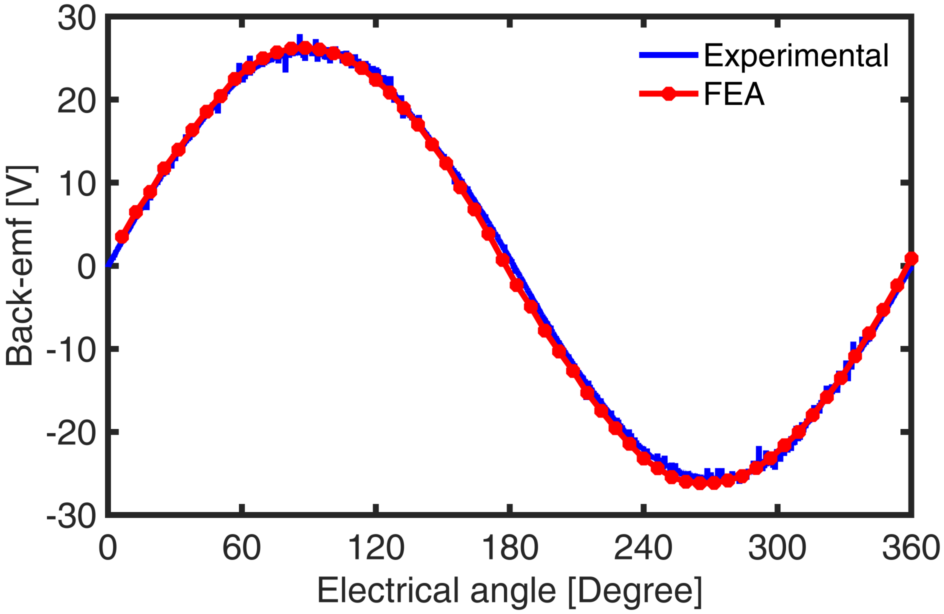

Figure 3.38: The simulated and experimental open-circuit back electromotive force (EMF) at 300rpm.

phase inductance. A preliminary comparative simulation study shows performance improvement over a conventional reference permanent magnet synchronous machine. An additional advantage of the two-phase construction is the inherent fault tolerance, owing to the lack of mutual coupling between the phases.

In this chapter, an optimal design study based 3D FEA for a novel vernier-type AFPM machine topology with one wound stator and one profiled stator without windings. The design optimization for the studied topology and its counterpart with two wound stators are conducted. The comparison shows that the topology with one wound stator and one profiled stator have a lower total loss and cost than the two wound stator counterpart.

In the proposed design, each main stator tooth has two auxiliary teeth, which serve to amplify the high-polarity aspect of the stator magnetomotive force that interacts with the rotor to generate net torque. The incorporation of these auxiliary small teeth within the main stator teeth results in a considerable enhancement of the output torque. It has been demonstrated that the profiled stator contributes less to the overall torque than the active stator. Moreover, the presence of these auxiliary teeth has been found to increase the torque output by approximately 61%, showcasing their significant impact on the machine's performance.

Chapter 4 Very High Power Density Motor with a Reluctance Rotor and a Modular Stator Having PMs and Toroidal Windings

4.1 Introduction and Problem Formulation

In this chapter, it is proposed a new high volumetric power density permanent magnet (PM) motor design for traction applications to achieve the 50kW/L target set by the US Department of Energy by increasing the torque capability and operating speed compared to conventional PM machine topologies. A large-scale multi-objective design optimization based on 2D finite element analysis (FEA) and differential evolution algorithm was conducted to achieve the best trade-off among high efficiency, high volumetric power density and high power factor. The torque-speed envelopes are also checked for the Pareto front designs to make sure they have a constant power speed ratio of at least 3:1. An open frame lab prototype (OFLP) motor has been fabricated and tested to validate the principle of operation and design optimization approach, and to identify the potential challenges in manufacturing and testing. Ongoing work on further pushing the electromagnetic performance to the limit and improving the manufacturing and cooling techniques are also discussed.

By placing PMs in the stator yoke or teeth, the risk of demagnetization by armature field can be minimized. In addition, since the rotors are simple reluctance structures, such machines are very suitable for high-speed operation and thus high power density design. This study presents the theoretical analysis, design optimization, and experimental study of a reluctance machine with both PMs and armature windings on the stator aiming at the 50kW/L volumetric power density target. Special care was considered for the stator core modularization, PM segmentation, winding structure, and cooling system to maximize the volumetric power density.

This chapter is substantially based on the following papers:

- P. Han, M. G. Kesgin *et al.*, ”Design Optimization of a Very High Power Density Motor with a Reluctance Rotor and a Modular Stator Having PMs and Toroidal Windings,” 2021 IEEE Energy Conversion Congress and Exposition (ECCE), pp. 4424-4430, 2021.

- *C. S. Goli, M. G. Kesgin* et al.*, ”Equivalent Circuit and Loss Components for a Special Double Salient Machine Employing a Stator with Phase Winding Modules and PMs,” (submitted for Journal Mar 2023).*

4.2 Literature Review

The U.S. DRIVE Electrical & Electronics Technical Team Roadmap (2017) identified key challenges and R&D targets for electric traction drive systems for the year 2025, which mainly include a volumetric power density requirement of 50kW/L for the motor, 100kW/L for the accompanying power electronics, and an overall system figure of 33kW/L [82]. This represents an ambitious 89% reduction in motor volume compared to 2020 targets. Representative electric machines used in state-of-the-art commercially available electric vehicles (EVs) and hybrid EVs (HEVs), mainly the induction machines and interior permanent magnet (IPM) machines, have been surveyed in [83]. Innovative motor and drive technologies having the potential to meet the DOE 2025 targets are, therefore, in great need.

Synchronous machines with PMs in the rotor have been continuously developed for increasing specific power capability. In order to achieve very high magnetic loading, the ”spoke” IPM configuration with radially oriented and tangentially magnetized PMs has been employed in conjunction with, for example: q-axis flux barriers [84], special stator tooth profiles [85], and high-polarity fractional slot-pole combinations, leading to high-performance demonstrators for special applications, such as Formula E traction motors [86]. A major challenge for PM synchronous motor designs is the cooling of the rotor in order to avoid the risks of PM overheating and demagnetization [87]. Alternative solutions are provided by machines in which both the armature windings and the PMs, possibly in a ”spoke” arrangement for flux focusing, are placed in the stator. Examples of such machine concepts include: doubly salient PM (DSPM) [88], flux-reversal PM [89], flux-switching PM [90, 91], and, more recently, switched reluctance with PMs [92] motor types. The power densities of existing traction motors used in commercial electric vehicles are significantly lower than the desired targets. This indicates that there is potential for improvement in the performance and efficiency of these vehicles, and future research may focus on achieving higher power densities in electric vehicle traction motors [93].

4.3 Proposed Very High Volumetric Power Density PM Motor

The proposed very high volumetric power density PM motor derived from the parallel path magnetic technology [94, 95] has a PM-free castellated reluctance rotor, a modular stator having concentrated toroidal coils and circumstantially magnetized PMs, as illustrated in Fig. 4.1. The robust rotor construction is very suitable for high-speed operation. In addition, since both the PMs and armature windings are placed on the stator and there is no overlapping between them, the design and implementation of the cooling system are expected to be significantly simplified.

The toroidal windings are naturally concentrated, therefore, the copper slot fill is improved and the end coils are shortened compared to conventional distributed windings, which lead to reduced dc copper loss. The adjacent magnets are magnetized in the opposing way, as shown in Fig. 4.2, to provide the desired flux coupling for torque enhancement [94, 95]. The combination of stator PMs, rotor protrusions and stator winding layout plays a key role in determining the overall electromagnetic performance, such as average torque, torque ripple, power factor, etc, which will be shown in Section 4.4.

4.4 Operating Principle and Analysis

To show the operating principle and torque production mechanism of the proposed motor, both the open-circuit (OC) PM field and OC armature field are analyzed based on the simple MMF-permeance model illustrated in Fig. 4.3. In analyzing the OC PM field, the armature windings are removed and PMs are the only source of the

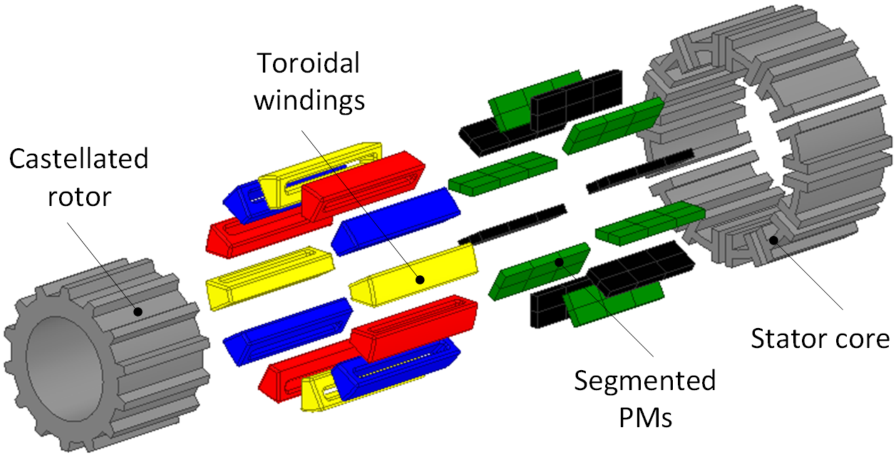

Figure 4.1: Exploded view of the proposed PM motor. The PM-free castellated rotor, modular stator, segmented PMs, and concentrated toroidal windings are the key features.

magnetic field.

Neglecting the slotting effect of the stator, the air-gap flux density distribution produced by PMs can be expressed concisely as (4.1),

$$\begin{aligned}
&B_{PM}(\phi,t) = \\
&\frac{F_{PM}}{2h+1}\Bigg\{\left(\frac{\Lambda_{max}+\Lambda_{min}}{2}\right)\sin\left[(2h+1)p_m(\phi-\phi_0)\right] \\
&+\left(\frac{\Lambda_{max}-\Lambda_{min}}{4}\right)\sin\left[(2h+1)p_m+N_r\right]\cdot \\
&\left[\phi-\frac{N_r\omega_r}{(2h+1)p_m+N_r}t-\frac{(2h+1)p_m\phi_0+N_r\theta_{r0}}{(2h+1)p_m+N_r}\right] \\
&+\left(\frac{\Lambda_{max}-\Lambda_{min}}{4}\right)\sin\left[(2h+1)p_m-N_r\right]\cdot \\
&\left[\phi-\frac{-N_r\omega_r}{(2h+1)p_m-N_r}t-\frac{(2h+1)p_m\phi_0-N_r\theta_{r0}}{(2h+1)p_m-N_r}\right]\Bigg\},
\end{aligned} \tag{4.1}$$

where $B_{PM}(\phi,t)$ is the air-gap flux density distribution produced by PMs only. F_{PM} is the amplitude of the square-wave MMF created by PMs. Λ is the air-gap permeance, the subscripts "max" and "min" of which denote the maximum and minimum value, respectively. p_m is the principal pole pairs of the PM array, which is half of the number of PMs. ϕ is the mechanical angle along the air-gap peripheral. ϕ_0 is the initial position from the reference axis. h is a positive integer. N_r is the number of rotor protrusions. ω_r is the mechanical rotor speed, and θ_{r0} the initial rotor position. t is time.

Equation (4.1) shows that there are three groups of flux density harmonics in the air gap when only the PMs are considered as the source, whose pole pairs are $(2h+1)p_m$, $(2h+1)p_m + N_r$ and $|(2h+1)p_m - N_r|$. In addition, their rotating speeds are different.

Similarly, the air-gap flux density distribution $B_{AR}(\phi, t)$ produced by the armature windings solely can also be obtained, as expressed by (4.2),

$$\begin{aligned}
B_{AR}(\phi, t) = \frac{3W_{max}I_m}{\pi}\Bigg\{ &\left(\frac{\Lambda_{max}+\Lambda_{min}}{2}\right)\cdot \\
&\sum_{n=3r+1=tp_a}^{\infty}\frac{1}{(n/p_a)}\sin n\left[\phi - \left(\frac{\omega}{n}\right)t - \left(\phi_{a0} - \frac{\varphi_a}{n}\right)\right] \\
&+\left(\frac{\Lambda_{max}-\Lambda_{min}}{4}\right)\sum_{n=3r+1=tp_a}^{\infty}\frac{1}{(n/p_a)}\sin\left(n+N_r\right)\cdot \\
&\left[\phi - \left(\frac{\omega - N_r\omega_r}{n+N_r}\right)t - \left(\frac{n\phi_{a0} + N_r\omega_r - \varphi_a}{n+N_r}\right)\right] \\
&+\left(\frac{\Lambda_{max}-\Lambda_{min}}{4}\right)\sum_{n=3r+1=tp_a}^{\infty}\frac{1}{(n/p_a)}\sin\left(n-N_r\right)\cdot \\
&\left[\phi - \left(\frac{\omega + N_r\omega_r}{n-N_r}\right)t - \left(\frac{n\phi_{a0} - N_r\omega_r - \varphi_a}{n-N_r}\right)\right]\Bigg\},
\end{aligned} \tag{4.2}$$

where $B_{AR}(\phi, t)$ is the air-gap flux density distribution produced by armature windings only. W_{max} is the peak value of the sawtooth-wave winding function and I_m the peak value of phase current. p_a is the principal pole pairs of the armature winding,

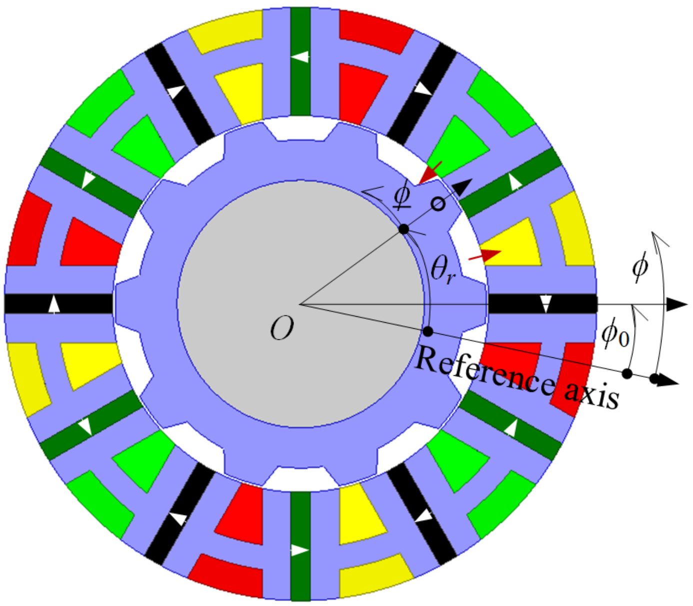

Figure 4.2: Cross-sectional view of the design with 10 rotor protrusions.

which is the same as the number of coils per phase. n, r, and t are positive integers. ω is the electrical frequency of winding currents, and φ_a the phase angle. ϕ_{a0} is the angle from the reference axis to the phase-A winding axis. There are also three groups of air-gap flux density harmonics, whose pole pairs are $n = 3r + 1 = tp_a$, $n + N_r$ and $|n - N_r|$.

With the closed-form analytical air-gap flux density distributions $B_{PM}(\phi, t)$ and $B_{AR}(\phi, t)$, the electromagnetic torque can be derived by using the principle of virtual work:

$$T_{em} = \frac{\partial W_{co}}{\partial \theta_r} = \frac{\partial}{\partial \theta_r} \int_V \frac{\{B_{PM}(\phi, t) + B_{AR}(\phi, t)\}^2}{2\mu_0} dV. \tag{4.3}$$

By applying the orthogonality relations of sine functions to (4.3), it can be drawn that only the flux density harmonics from the PM field and armature field of the same pole pairs will produce the non-zero average torque. As a result, the average electromagnetic torque of this motor is contributed by multiple dominating air-gap flux density harmonics, whose pole pairs of 4, 6, 8, 16, 18 and 28.

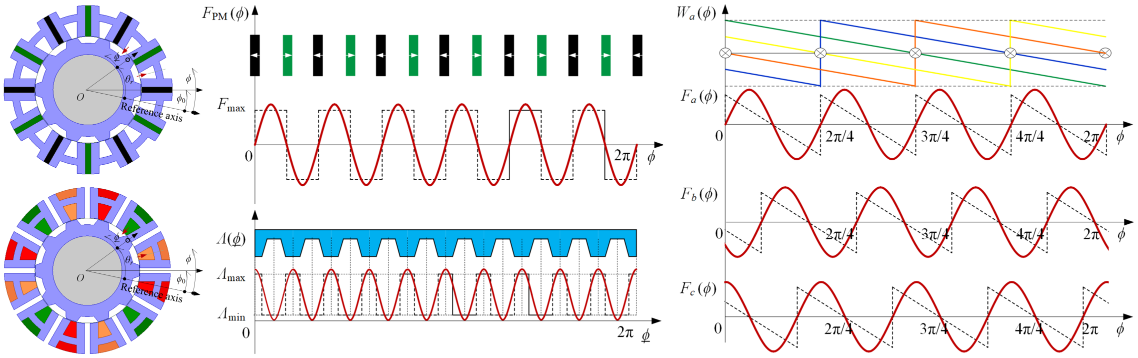

Figure 4.3: Simple MMF-permeance models for the proposed motor with PMs only and armature windings only. The fundamental components of the air-gap permeance function and winding functions of armature coils are used for derivation. The winding functions of the toroidal windings are sawtooth waves, which are very different from the conventional slot windings.

It is also revealed that there will be no torque, if one of the following is absent: stator PMs which are denoted by F_{PM} in (4.1), current in stator toroidal coils, or the rotor with protrusions denoted by Λ_{max} and Λ_{min}. The castellated reluctance rotor serves mainly as a modulator to couple PMs and armature windings through air-gap flux density harmonics and there is virtually no synchronous type reluctance torque, i.e., the torque component proportional to the product of d-axis and q-axis currents in conventional synchronous machines.

In addition, by examining terms in (4.3), the appropriate combinations of stator PMs, rotor protrusions, and stator winding layouts producing non-zero average torques can be readily identified. Typical topologies derived from this approach include the 5-protrusion (5-P) and 7-protrusion (7-P) designs for a stator with 6 PMs and 6 toroidal coils, and the 10-protrusion (10-P) and 14-protrusion (14-P) designs for a stator with 12 PMs and 12 toroidal coils.

Equations (4.1)-(4.3) well explain the operating principle and torque production mechanism of the proposed motor, but are not suitable for accurate force/torque computation. The Maxwell stress tensor method is used instead. The radial and tangential components of the electromagnetic stress in the airgap, f_r, and ,f_t, can be expressed by the following:

$$f_r(\phi, t) = \frac{B_r(\phi, t)^2 - B_t(\phi, t)^2}{\mu_o}, \tag{4.4}$$

$$f_t(\phi, t) = \frac{B_r(\phi, t)B_t(\phi, t)}{\mu_o}, \tag{4.5}$$

where $B_r(\phi, t)$ and $B_t(\phi, t)$ are the radial and tangential air-gap flux densities calculated by FEA. The radial and tangential force on the stator teeth and rotor protrusions can be obtained by integrating the corresponding stress component over circumferential intervals, as shown by the example in Fig. 4.4 and Fig. 4.5. Radial component of force density is substantially higher than tangential components. Radial force of stator tooth modules which is two stator teeth and magnet between them at given rotor position can be seen in Fig. 4.6. Torque contribution of each stator tooth module which is two stator teeth and magnet between them is different from each other, but half motor symmetry can be see in Fig. 4.7.

Average torque contributed by stator teeth, magnets, and coils are calculated for the studied machine from this approach. The produce majority of the torque is produced by the leading teeth located at the left-hand side of magnets when looking into the page. Torque produced by magnets and the tracking teeth located other side of the magnet almost cancel each other. The surface of coils facing the airgap contribute little torque.

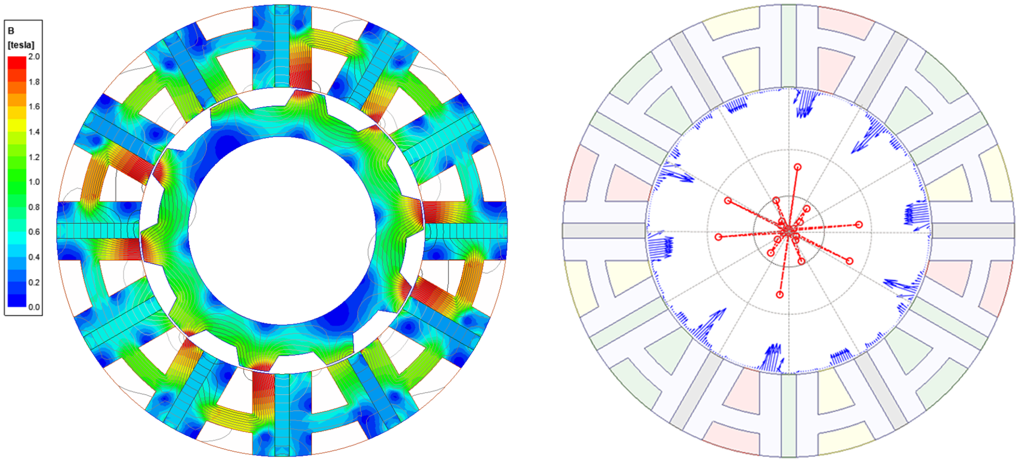

(a) (b)

Figure 4.4: FEA results of the proposed motor at rated load, (a) flux density distribution and flux pattern, (b) electromagnetic force on stator teeth. Blue arrows denote the distributed force vectors and red dots denote the resultant forces on teeth.

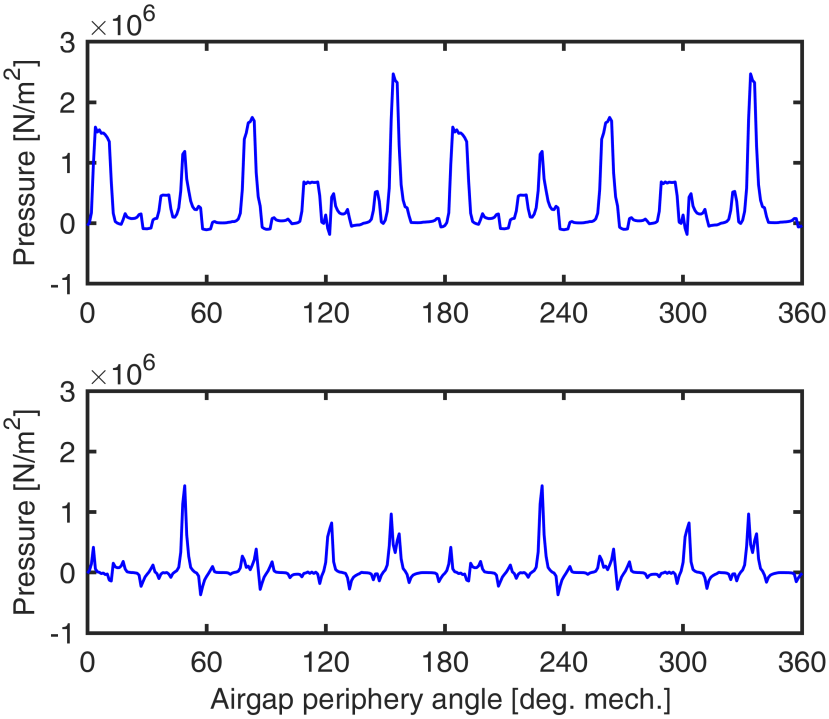

Figure 4.5: Air-gap stresses at rated load: radial component (top), (b) tangential component (bottom).

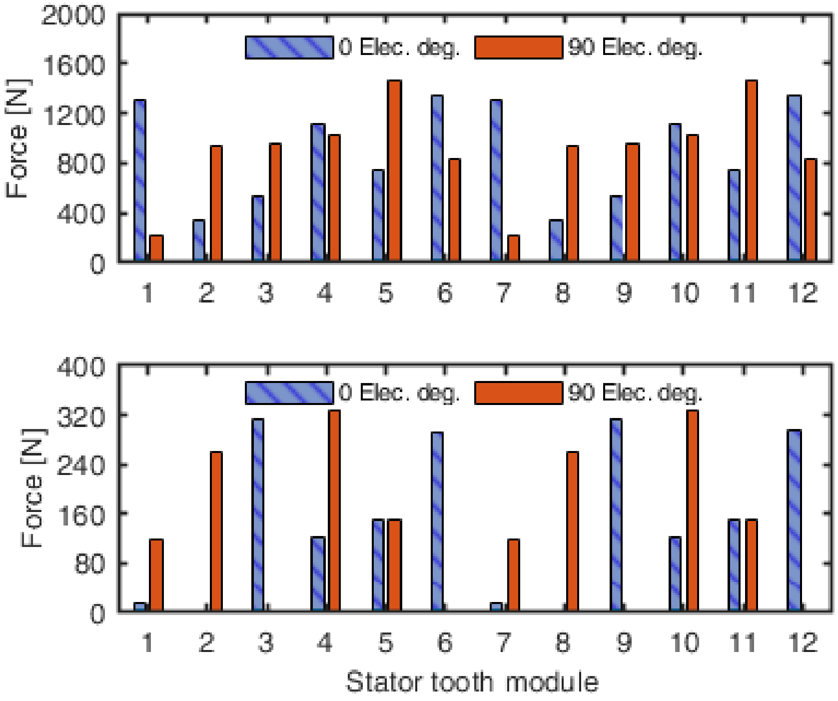

Figure 4.6: Radial (top) and tangential (bottom) force on the stator tooth module at different rotor position under rated-load.

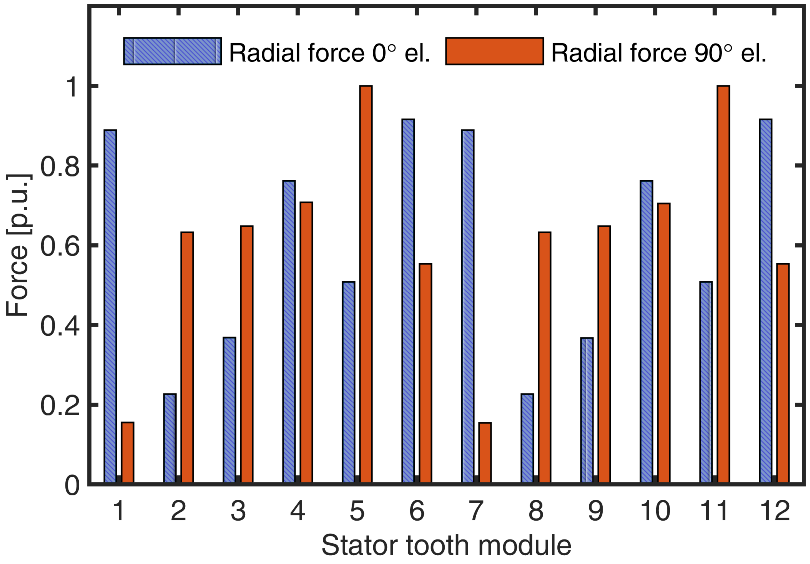

Figure 4.7: Electromagnetic torque contribution of each stator module at different rotor position under rated-load.

4.5 Multi-objective Design Optimization based on FEA

Parametric models for a number of motor topologies were developed following the derived combinations from Section 4.4. Based on the parametric electromagnetic FEA models for the 5-P, 7-P, 10-P and 14-P designs illustrated in Fig. 4.2 with 10 independent geometric and control variables, a large-scale design optimization was performed, following the optimization approach used in, for example, [53, 96]. The objectives were to maximize the volumetric power density with a 50kW/L target, efficiency and power factor, assuming an equivalent electric loading, i.e., the product of current density and copper slot fill factor, equal to 9.75A/mm^2 can be achieved by the cooling design and advanced winding technology. The results of optimization studies indicated that specific torque increases with number of rotor protrusions, and so do core losses, in line with expectations.

A systematic comparative study between two motor topologies was also carried out based on multi-objective design optimizations, one with 10-P and the other 14-P, as shown in Fig. 4.8. The three concurrent objectives were to maximize the power density, minimize the total loss, and maximize the power factor. The computational results show that, the optimal 14-P designs can achieve similar fundamental power factors as optimal 10-P designs. There are trade-offs between 10-P and 14-P designs in terms of the volumetric power density and total loss (Fig. 4.9).

Multiple design generations of the adopted differential evolution optimization yielded a satisfactory Pareto front. A number of candidate designs were identified, with estimated volumetric power density $\geq$ 50kW/L, as shown in Fig. 4.10. The

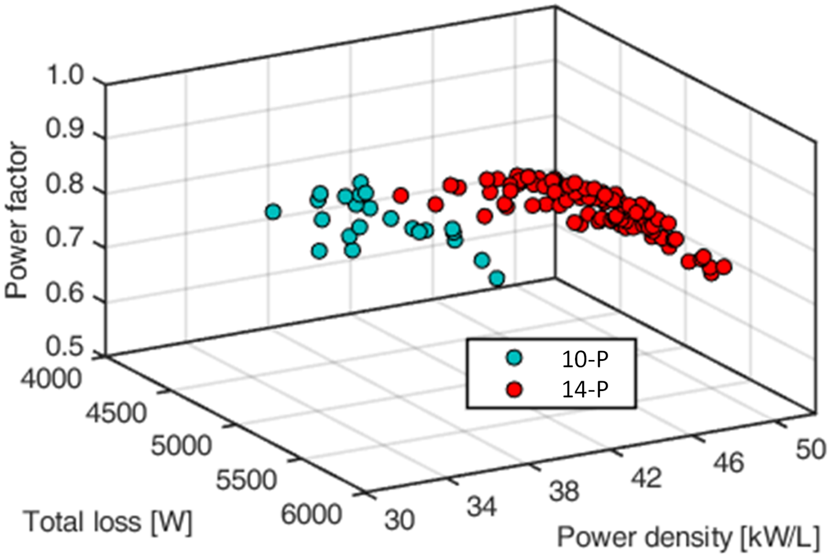

Figure 4.8: Optimization results: 3D Pareto front projection with objectives of total loss, power density, and power factor.

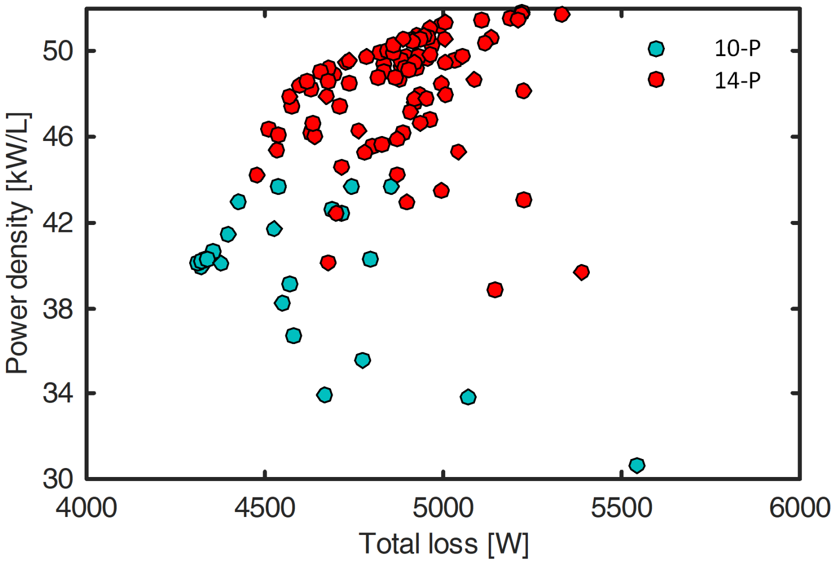

Figure 4.9: Optimization results projection in total loss - power density plane.

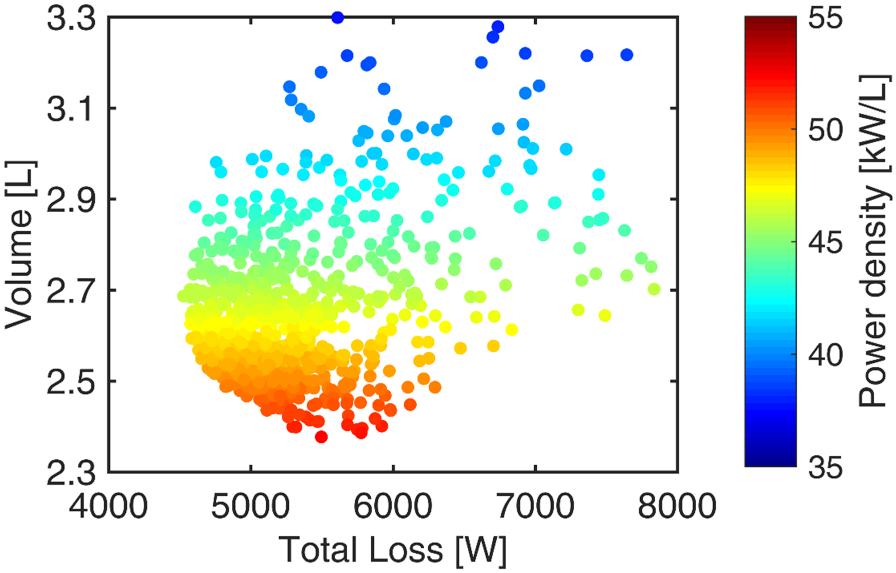

Figure 4.10: Optimization results: Pareto front of total loss and volume.

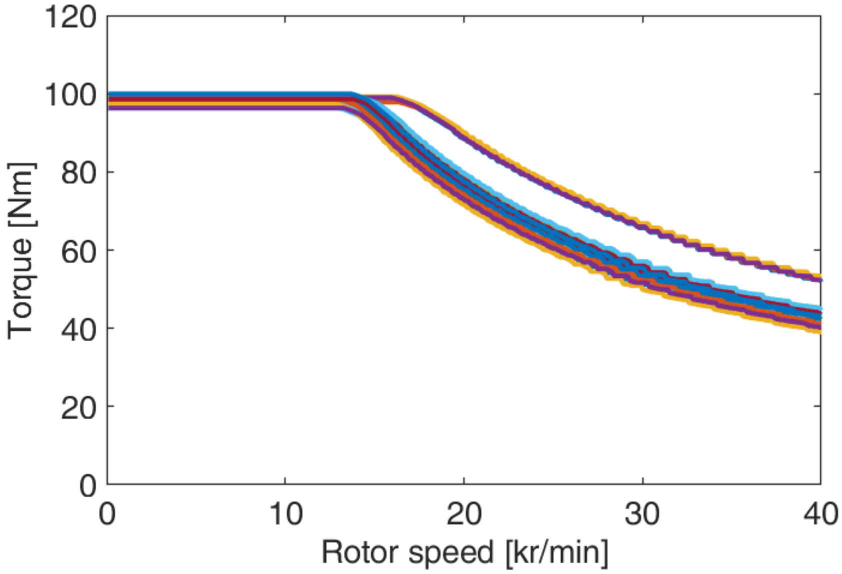

Figure 4.11: Torque-speed envelops of the Pareto front designs.

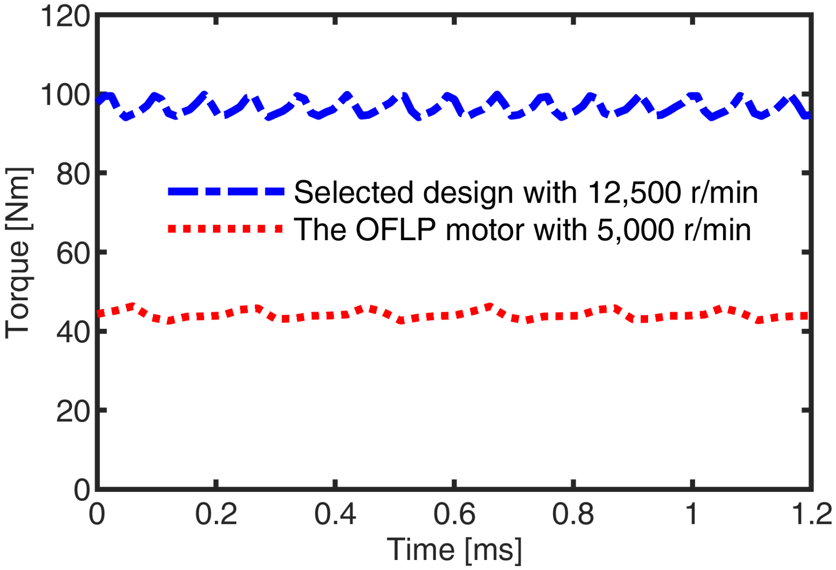

Figure 4.12: Torque waveform for high power density optimal design and its OFLP version. Low torque ripple is observed for both operation points.

torque-speed and efficiency maps have also been calculated based on 2D electromagnetic FEA, as plotted in Fig. 4.11, showing that the optimally designed motor can operate with a constant power of 125kW at up to 3 times the base speed, which is 12,500r/min. The selected optimal design for the proposed topology produces 96Nm at 12,500r/min. The waveform of the OFLP motor and the optimal design can be seen Fig. 4.12.

4.6 Prototype and Testing

To validate the proposed very high volumetric power density motor and the adopted design optimization approaches, as well as to identify the potential challenges in manufacturing and testing to achieve the final goal of 50kW/L, a 28hp OFLP motor rated at 40Nm and 5,000r/min was fabricated, as shown in Fig. 4.13, and tested.

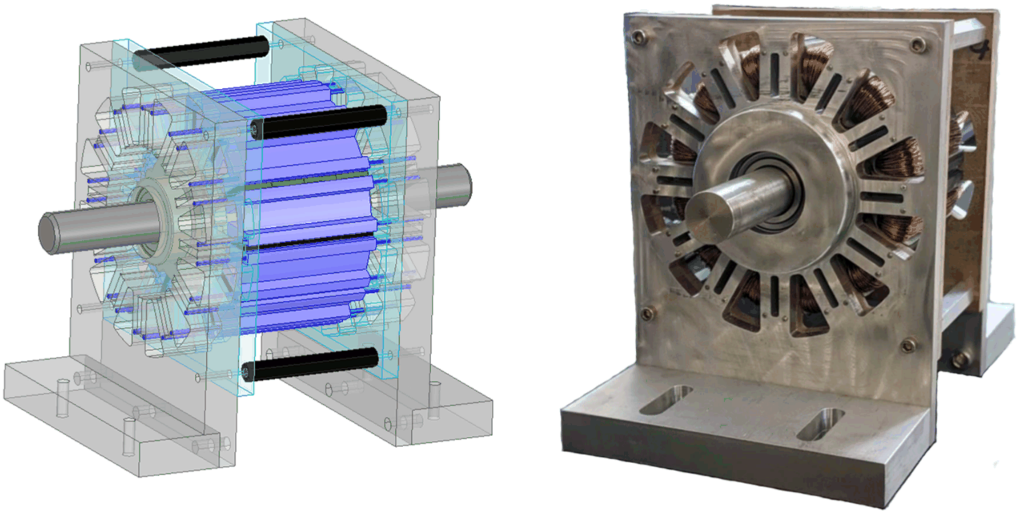

Figure 4.13: The CAD drawing and photo of the full assembly for the open frame lab prototype motor. Dowel pins were used in the laminated stator segments. PMs were segmented in both radial and axial directions to reduce the PM eddy current losses. All the coil terminals have been brought out for detailed testing purpose.

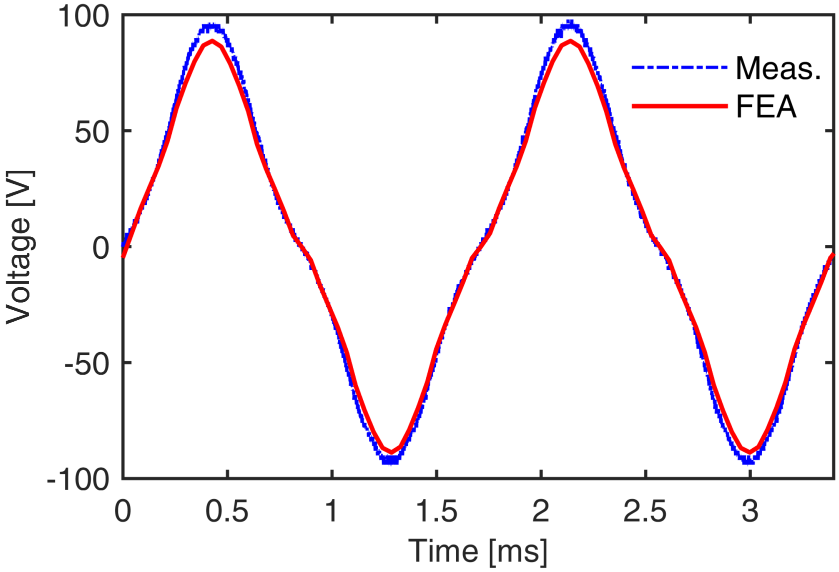

Figure 4.14: Simulated and experimental open-circuit back EMF for phase-A winding.

The experimental testing was conducted to measure the OC back-electromotive force (EMF) for a single phase with 4 coils connected in series, as plotted in Fig. 4.14, showing good agreement between the experimental measurements and 2D FEA calculations.

The static torques at different rotor positions were also measured when the phase-A winding was connected in series with the parallel of phase-B and phase-C windings. Each phase has 4 coils connected in series. It is shown that, within the expectation, the measured static torque has the same trend as the 2D FEA as seen in Figs 4.15 and 4.16. The deviation is approx. 10% and can be explained by the backlash of the locking device, especially at the high torque region, the temperature rise, the inaccuracies of material properties, etc.

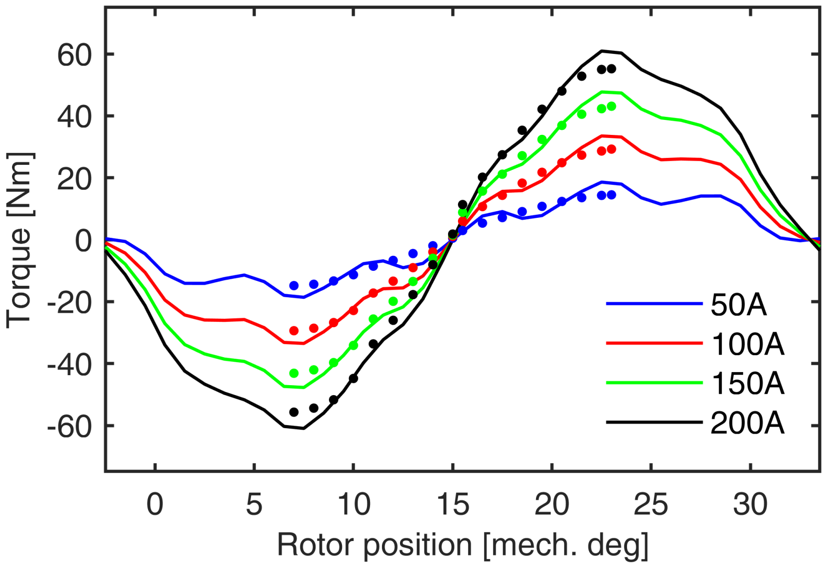

Figure 4.15: Testing results of torque measured static torque versus rotor positions (continuous lines – FEA results, dots – experimental measurements)

An additional experiment was performed to measure inductance and losses. The

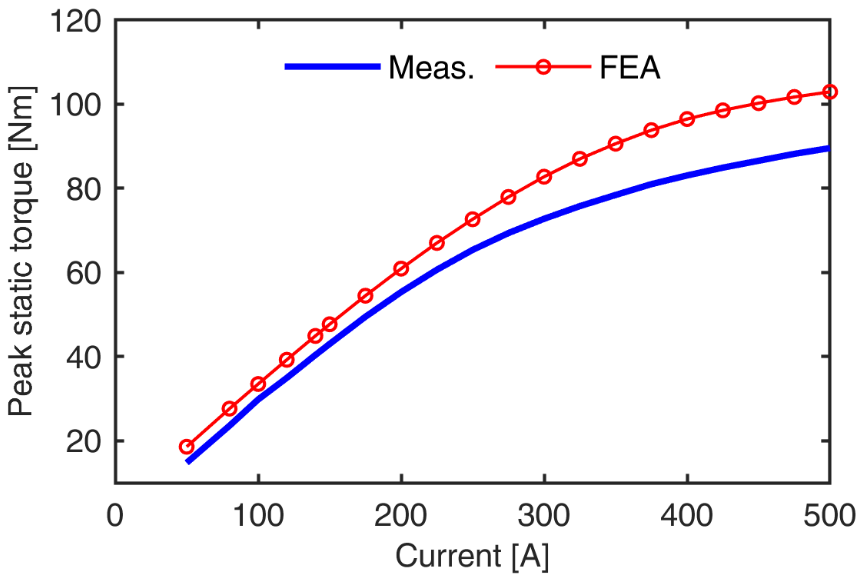

Figure 4.16: Testing and simulation results of peak torque versus different current values.

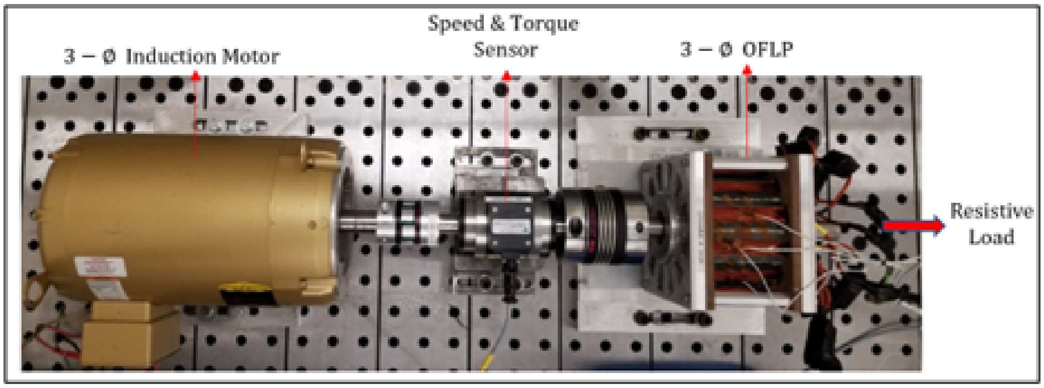

Figure 4.17: The experimental dyno test setup of the OFLP of the proposed special double salient machine operating as a generator at unity .

experimental setup consists of a three-phase AC/DC/AC drive, a three-phase induction motor, the OFLP of the proposed special machine, and a three-phase resistive load as in Fig. 4.17.

The UPF test has been implemented by operating the OFLP as a three-phase generator supplying power to a variable resistive load. The OLFP has been designed to run at a rated speed of 5,000r/min at 41Nm. The three-phase induction motor is being used as a prime mover has a rated speed of 3,525r/min at a load of 30Nm.

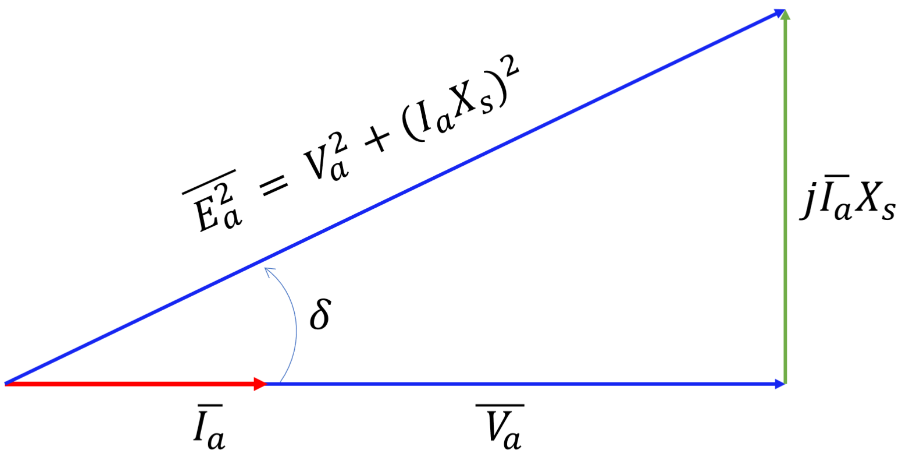

Figure 4.18: Schematic of per phase vector diagram of the OFLP as a generator driving a resistive load at unity power factor.

A speed & torque sensor coupler has been mounted between the prime mover and OFLP. The line-to-line voltages and three-phase currents are measured at the output terminal of the OFLP. The OFLP has been operated at four different speeds at variable loads of up to 30Nm. The experimental results have been used to determine the inductance and to evaluate the losses. The experimental data of induced emf, terminal voltage, and load current at different operating points have been used to plot the per phase vector diagram as shown in Fig. 4.18. and reported in 4.1

The per-phase vector diagram at unity power factor has been used to determine the inductance as shown in Fig. 4.18. Electromagnetic FEA simulations for this type of generator operation at 3,500r/min and 65A resulted in an induced voltage of 53.7V and, though combinations with open-circuit simulations, to an inductance of 130.2uH, indicating satisfactory agreement with measurements.

The 2D and 3D FEA simulations for the special machine have been performed at the identical operating points of the experimental tests to numerically separate the losses providing a basis for the ongoing optimization studies. The 2D FEA schematic of the special double salient machine showing the core losses and eddy current loss on winding is shown in Fig. 4.19 and 4.20.

The 3D FEA simulations have been performed to evaluate the core losses associated with the rotor, stator, and eddy current losses in the PMs. 2D FEA simulations have been performed to determine the eddy current losses in the windings. The conductors in the 2D schematic have been arranged in a specific sequence of series and parallel combinations in identical with the winding structure of the OFLP. The conductors nearby stator core segments experience higher skin effect due to more flux linkages and hence higher inductance. Skin effect is less dominant in the conductors nearby airgap and hence distribution of current improves. The loss components at different operating points have been reported in Table 4.2 and 4.3, ploted in Fig. 4.21.

Table 4.1: Experimental data from a unity power factor generator test, employed for inductance identification, showed that the average inductance value satisfactorily compares with the value estimated based on FEA simulations.

Speed (RPM)	3500	3000	2400	2000
Frequency (Hz)	588	499	400	332
Load Current (A)	65	60	52	45
Terminal voltage per phase: V_a (V)	41.3	36.12	29.9	27.76
Induced voltage per phase: E_a (V)	52.3	43.6	34.8	30.1
Reactance per phase: $X_s = X_d = X_q$ (Ω)	0.493	0.406	0.324	0.264
Inductance per phase: $L_s = L_d = L_q$ (μH)	133.61	129.80	129.18	126.68

Table 4.2: Torque and loss results by experimental tests

Operating Points		**Experimental Test Results**		
Speed [RPM]	Current [A]	T_m [Nm]	P_{load} [W]	Joule Losses [W]
3500	65	26.7	8075	191
3000	60	25.3	6988	163
2400	52	21.8	4652	121
2000	45	20	3657	92

Table 4.3: Torque and loss results by FEA

Operating Points		**FEA Simulation Results**			
Speed [RPM]	Current [A]	T_m [Nm]	Core loss [W]	PM loss [W]	Wdg. Eddy Current Loss [W]
3500	65	30.5	282	50	171
3000	60	28.3	212	35	143
2400	52	24.5	121	22	102
2000	45	21.4	92	14	75

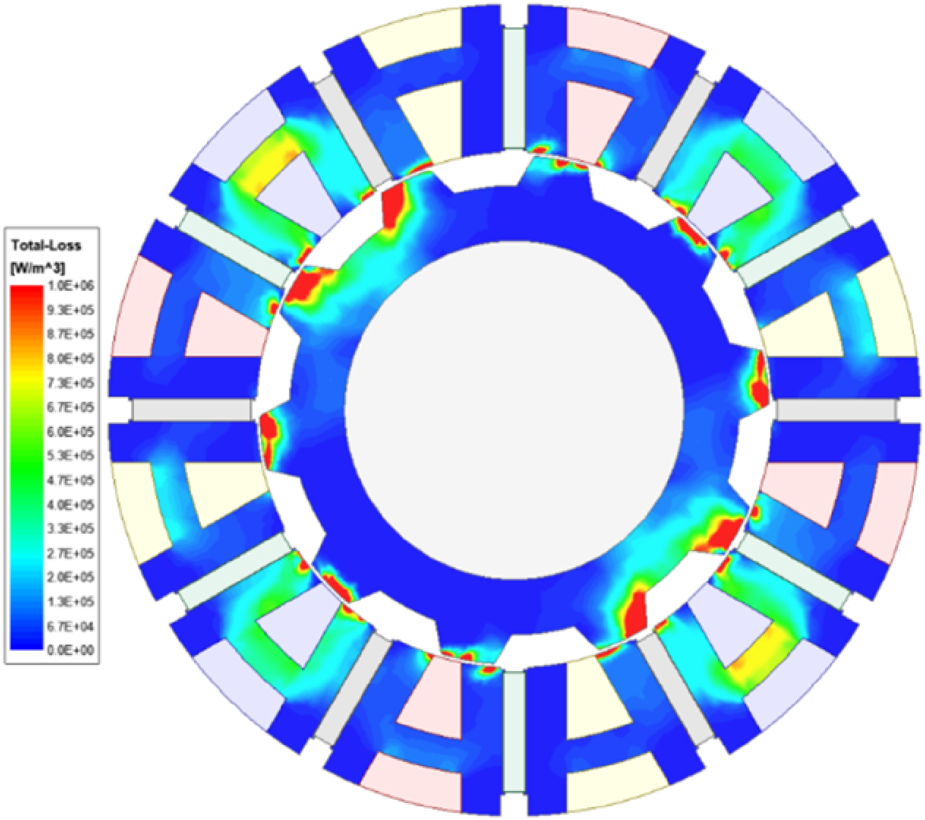

Figure 4.19: Electromagnetic 2D FEA plot of the proposed special machine showing core losses in the modular stator and reluctance rotor.

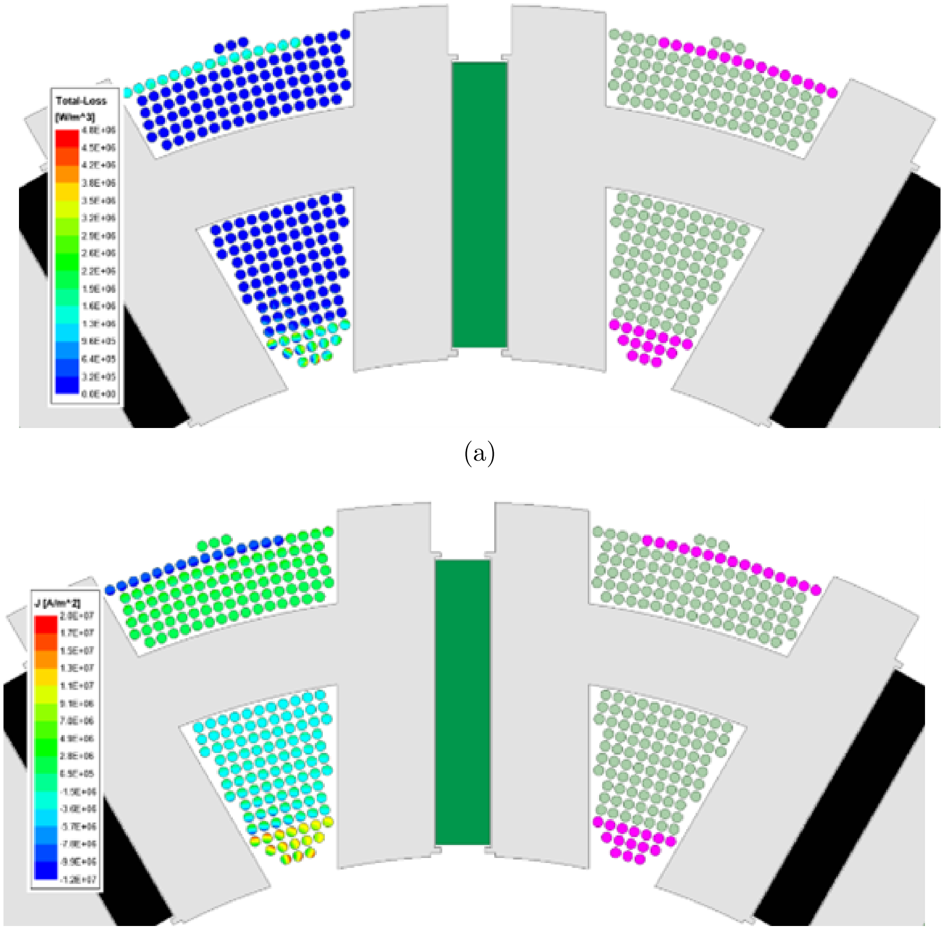

(a)

(b)

Figure 4.20: 2D FEA detailed winding model: (a)Supplementary eddy current specific losses and (b) distribution in the stator winding conductors simulated.

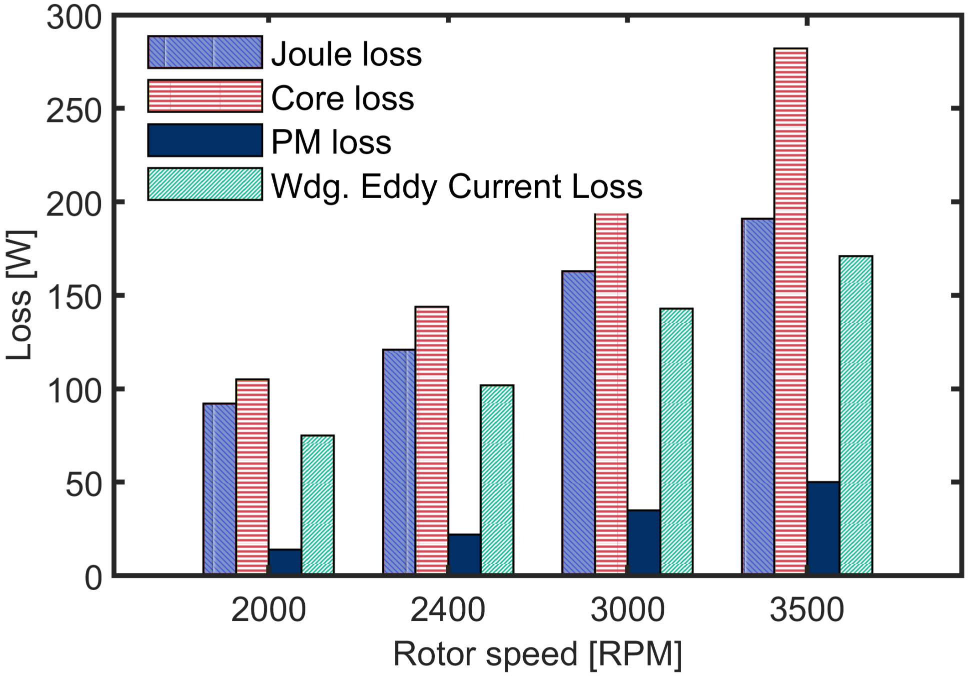

Figure 4.21: Loss components calculated by 3D and 2D FEA.

4.7 Conclusion

The OFLP motor achieves a volumetric power density of 8.4kW/L at 5,000r/min with an open housing for air cooling. The reduced power density is attributed to the low copper slot fill of 0.41 achieved by hand wound wired coils, the reduced speed due to the limitations of current testing facilities, and the reduced current density to prevent overheating with the air cooling. The 50kW/L target is anticipated to be achieved by improving the copper slot fill to 0.75-0.8 by advanced winding technologies, for example, the additively manufactured coils [97], and increasing the current density to produce higher torque enabled by the advanced cooling technologies, such as the one presented in [98], and operate the motor at the designed rated speed of 12,500r/min.

In the meantime, reducing the losses, mainly the core losses, by reducing the number of rotor protrusions and therefore the fundamental driving frequency is underway to simplify the cooling design. Reducing the fundamental frequency will also benefit the control system and reduce the switching frequency.

The proposed motor has numerous advantages for high power density designs, such as the high-speed operation capability, better cooling design, compact winding structure, modularized manufacturing of the stator, and an inherent wide speed range with a constant power speed ratio of at least 3:1. Appropriate combinations of stator PMs, stator windings, and rotor protrusions are required to produce high torque. The electromagnetic performance trade-offs mainly lie between the power density and efficiency, and large-scale design optimizations are required to achieve the optimal designs in the sense of multiple objectives. Advanced winding technologies that can substantially increase the copper slot fill and cooling techniques that can effectively dissipate the heat generated by losses in the stator are two enabling technologies to achieve the 50kW/L target for the proposed topology.

Chapter 5 Conclusion

5.1 Summary and Conclusions

The essential aspects of developing coreless AFPM machines, such as utilizing specialized construction techniques such as Litz wires and PCB windings, particularly at high frequencies, are discussed in Chapter 2. Coreless AFPM machines can achieve high efficiency through design optimization and the use of Litz wire or PCB windings since there are no geometrical constraints caused by teeth and slots. Flywheels made from composite materials with high tensile strength and low mass density can be employed for energy storage in various applications, particularly in microgrid and utility grid systems that incorporate renewable energy sources. High-speed AFPM machines demonstrate the feasibility of high energy density and specific power in FESS, and the adjustable airgap length can aid in reducing self-discharge during standby mode. The disk-like shape of the rotor of axial-flux PM motor/generator enables integration with the flywheel rotor. The study performed in this paper opens up new opportunities for AFPM machines in the integration of renewable energy sources into the grid.

Chapter 3 introduces a new topology of an axial-flux vernier-type machine known as the MAGNUS motor. This topology has 40 spoke rotor poles and only six coils for the 3-phase stator. The rotor is of the spoke type and is positioned between one wound stator and one profiled stator without windings. A large-scale multi-objective optimization study with 3D finite element analysis has been conducted to minimize material cost and maximize electromagnetic efficiency for this topology. Design optimization for its counterpart with two wound stators has also been carried out, revealing that the topology with one wound stator and one profiled stator has lower total loss and cost than the two wound stator counterpart.

The proposed design has two auxiliary teeth on each main stator tooth, which amplifies the high-polarity aspect of the stator magnetomotive force that interacts with the rotor to generate net torque. The presence of these auxiliary teeth increases the torque output by approximately 61%, demonstrating their significant impact on the machine's performance. The selected optimal design from the Pareto front has been prototyped, and tested.

In Chapter 4, a new topology of a double salient machine was proposed to achieve high volumetric power density. Comprehensive design optimization was conducted on a large scale, considering maximum efficiency and power factor. The operating principle and torque production mechanism based on the air-gap flux density waveforms were analyzed with the optimal design. The optimal design was prototyped and tested, resulting in an OFLP motor that achieves a volumetric power density of 8.4kW/L at 5,000r/min with an open housing for air cooling. With advanced winding and cooling techniques, the design has the potential to achieve the 50 kW/L target.

5.2 Original Contributions

The original contributions of the dissertation are summarized as:

- Developed a procedure of optimizing an electric machine based on finite element analyses and employing differential evolution. The method has been demonstrated on an axial flux permanent magnet machine (Chapter 2).
- The axial-flux vernier type machines of the MAGNUS type motor of new topology has been introduced. Its working principle has been analyzed and feasible slot-pole combinations for 2-phase and 3-phase versions have been established. Which these topologies demonstrate a high level of demagnetizing fault tolerance due to their lack of coupling between phases (Chapter 3).
- A large-scale multi-objective optimization study has been conducted for axial-flux vernier-type PM machine with 3-dimensional (3D) finite element analysis (FEA) to minimize the material cost and maximize the electromagnetic efficiency. A detailed study for torque contribution has indicated that auxiliary teeth on each stator main teeth amplify net torque production. A prototype of optimal design has been built and tested (Chapter 3).
- A new topology of a double salient machine has been proposed to achieve high volumetric power density. The PMs are placed in the stator yoke and teeth, which reduces the risk of demagnetization by armature field. The rotors are simple reluctance structures, such machines are very suitable for high-speed

operation and thus high power density design. Theoretical analysis and experimental study of a reluctance machine with both PMs and armature windings on the stator(Chapter 4).

- Comprehensive design optimization at a large scale has been conducted with maximum efficiency and power factor. The optimal design can achieve the 50 kW/L target with advanced winding and cooling techniques (Chapter 4).

5.3 Recommendations for Future Work

- To validate the design further, additional experimentation is necessary. Detailed measurements of parameters, such as inductance and phase resistance, should be performed. Static and cogging torque measurements should also be conducted to obtain a comprehensive understanding of the machine's behavior.

- The prototype should be tested in both generating and motoring situations under various speed, load, and operating conditions to thoroughly evaluate its performance and loss separation. Some experimental tests should be conducted to identify the impact of saturation on the prototype, especially for high-power density motors. Additionally, the no-load test can help to determine the machine's losses and efficiency.

- To determine the fault tolerance and reliability of the prototype, some experimental tests can be conducted such as locked-rotor and insulation resistance tests.

Chapter 5 References

[1] V. A. Boicea, "Energy storage technologies: The past and the present," *Proceedings of the IEEE*, vol. 102, no. 11, pp. 1777–1794, Nov 2014.

[2] S. Vazquez, S. M. Lukic, E. Galvan, L. G. Franquelo, and J. M. Carrasco, "Energy storage systems for transport and grid applications," *IEEE Transactions on Industrial Electronics*, vol. 57, no. 12, pp. 3881–3895, Dec 2010.

[3] F. Blaabjerg and D. M. Ionel, *Renewable Energy Devices and Systems with Simulations in MATLAB®and ANSYS®*. CRC Press, May 2017.

[4] N. Taran, V. Rallabandi, G. Heins, and D. M. Ionel, "Coreless and conventional axial flux permanent magnet motors for solar cars," *IEEE Trans. Ind. App.*, vol. 54, no. 6, pp. 5907–5917, Nov 2018.

[5] V. Rallabandi, N. Taran, and D. M. Ionel, "Multilayer concentrated windings for axial flux pm machines," *IEEE Trans. on Magn.*, vol. 53, no. 6, pp. 1–4, 2017.

[6] V. Rallabandi, N. Taran, D. M. Ionel, and J. F. Eastham, "Coreless multidisc axial flux pm machine with carbon nanotube windings," *IEEE Trans. Magn.*, vol. 53, no. 6, pp. 1–4, 2017.

[7] N. Taran, V. Rallabandi, and D. M. Ionel, "Waved: A coreless axial flux pm motor for drive systems with constant power operation," in *2019 IEEE Trans. Electric Mach. Conf. and Expo (ITEC)*, 2019, pp. 1–6.

[8] M. G. Kesgin, P. Han, N. Taran, and D. M. Ionel, "Overview of flywheel systems for renewable energy storage with a design study for high-speed axial-flux

permanent-magnet machines," in *2019 8th Int. Conf. Renew. Ener. Research and App. (ICRERA)*, 2019, pp. 1026–1031.

[9] Z. Zhang, A. Matveev, R. Nilssen, and A. Nysveen, "Ironless permanent-magnet generators for offshore wind turbines," *IEEE Trans. Ind. Appl.*, vol. 50, no. 3, pp. 1835–1846, 2014.

[10] B. Xia, J. Shen, P. C. Luk, and W. Fei, "Comparative study of air-cored axial-flux permanent-magnet machines with different stator winding configurations," *IEEE Trans. Ind. Electron.*, vol. 62, no. 2, pp. 846–856, 2015.

[11] Y. Liu, Z. Zhang, C. Wang, W. Geng, and T. Yang, "Design and analysis of oil-immersed cooling stator with non-overlapping concentrated winding for high-power ironless stator AFPM machines," *IEEE Trans. Ind. Electron.*, Mar. 2020, DOI: 10.1109/TIE.2020.2978694.

[12] N. Taran, V. Rallabandi, D. M. Ionel, G. Heins, and D. Patterson, "A comparative study of methods for calculating ac winding losses in permanent magnet machines," in *2019 IEEE Int. Electric Mach. Drives Conf. (IEMDC)*, 2019, pp. 2265–2271.

[13] N. Taran and D. M. Ionel, "A hybrid analytical and fe-based method for calculating ac eddy current winding losses taking 3d effects into account," in *2019 IEEE Energy Conv. Cong. and Expo. (ECCE)*, 2019, pp. 4867–4872.

[14] C. Zwyssig, S. D. Round, and J. W. Kolar, "An ultrahigh-speed, low power electrical drive system," *IEEE Trans. Ind. Electr .*, vol. 55, no. 2, pp. 577–585, 2008.

[15] H. Hämäläinen, J. Pyrhönen, J. Nerg, and J. Talvitie, "AC resistance factor of Litz-wire windings used in low-voltage high-power generators," *IEEE Trans. Ind. Electron.*, vol. 61, no. 2, pp. 693–700, 2014.

[16] F. Marignetti, G. Volpe, S. M. Mirimani, and C. Cecati, "Electromagnetic design

and modeling of a two-phase axial-flux printed circuit board motor," *IEEE Trans. Ind. Electron.*, vol. 65, no. 1, pp. 67–76, 2018.

[17] X. Wang, C. Li, and F. Lou, "Geometry optimize of printed circuit board stator winding in coreless axial field permanent magnet motor," in *IEEE Veh. Power Prop. Conf. (VPPC)*, 2016, pp. 1–6.

[18] ActivePower. [Online]. Available: http://www.activepower.com/en-GB/downloads

[19] Calnetix Technologies, LLC. [Online]. Available: https://www.calnet-ix.com/powerflux-active-magnetic-bearings

[20] PowerThru. [Online]. Available: http://www.power-thru.com/

[21] J. G. R. Hansen and D. U. O'Kain, "An assessment of flywheel high power energy storage technology for hybrid vehicles," Tech. Rep., Dec. 2011, ORNL/TM-2010/280.

[22] M. Andriollo, F. Graziottin, and A. Tortella, "Contact-less electromagnetic recharging system for heavy-duty bus flywheel storage," in *2015 International Conference on Renewable Energy Research and Applications (ICRERA)*, Nov 2015, pp. 232–237.

[23] PUNCH Flybrid. [Online]. Available: https://punchflybrid.com/appl-ications/

[24] M. M. Flynn, P. McMullen, and O. Solis, "High-speed flywheel and motor drive operation for energy recovery in a mobile gantry crane," in *APEC 07 - Twenty-Second Annual IEEE Applied Power Electronics Conference and Exposition*, Feb 2007, pp. 1151–1157.

[25] ABB, "Powerstore - renewable microgrid stabilization," Nov. 2017.

[26] S. Sanders, M. Senesky, M. He, and E. Chiao, "Low-cost flywheel energy storage demonstration," Tech. Rep., 2015. Publication number: CEC-500-2015-089.

[27] Beacon Power, LLC. [Online]. Available: https://beaconpower.com/

[28] M. R. Doyle, D. J. Samuel, T. Conway, and R. R. Klimowski, “Electromagnetic aircraft launch system-EMALS,” *IEEE Transactions on Magnetics*, vol. 31, no. 1, pp. 528–533, Jan 1995.

[29] Kinetic Traction Systems, Inc. [Online]. Available: https://kinetic-traction.com/flywheel-energy-storage-applications/

[30] Ricardo PLC. [Online]. Available: https://ricardo.com/news-and-media/news-and-press/flybus-to-start-testing-first-flywheel-hybrid-bus

[31] Temporal power. [Online]. Available: http://temporalpower.ca/

[32] J. Itoh, T. Masuda, D. Sato, T. Nagano, T. Suzuki, and N. Yamada, “Development of magnetic assist system in flywheel energy storage system for power load-leveling,” in *2016 IEEE International Conference on Renewable Energy Research and Applications (ICRERA)*, Nov 2016, pp. 198–203.

[33] M. Strasik, J. R. Hull, J. A. Mittleider, J. F. Gonder, P. E. Johnson, and K. E. McCrary, *et al.*, “An overview of boeing flywheel energy storage systems with high-temperature superconducting bearings,” *Superconductor Science and Technology*, vol. 23, no. 3, p. 034021, Feb 2010.

[34] X. Li, B. Anvari, A. Palazzolo, Z. Wang, and H. Toliyat, “A utility-scale flywheel energy storage system with a shaftless, hubless, high-strength steel rotor,” *IEEE Transactions on Industrial Electronics*, vol. 65, no. 8, pp. 6667–6675, Aug 2018.

[35] F. Thoolen, “Development of an advanced high speed flywheel energy storage system,” Ph.D. dissertation, Technische Universiteit Eindhoven, Eindhoven, January 1993.

[36] D. R. Conover, S. R. Ferreira, A. J. Crawford, D. A. Schoenwald, J. Fuller, and D. M. R. S. N. Gourisetti, *et al.*, “Protocol for uniformly measuring and expressing the performance,” Tech. Rep., Apr. 2016. PNNL-22010 Rev 2 / SAND2016-3078 R.

[37] S. Sabihuddin, A. Kiprakis, and M. Mueller, “A numerical and graphical review of energy storage technologies,” *Energies*, vol. 8, no. 1, pp. 172–216, Dec 2014.

[38] P. Yulong, A. Cavagnino, S. Vaschetto, Chai Feng, and A. Tenconi, “Flywheel energy storage systems for power systems application,” in *2017 6th International Conference on Clean Electrical Power (ICCEP)*, June 2017, pp. 492–501.

[39] S. Mousavi G, F. Faraji, A. Majazi, and K. Al-Haddad, “A comprehensive review of flywheel energy storage system technology,” *Renewable and Sustainable Energy Reviews*, vol. 67, pp. 477 – 490, 2017.

[40] P. Tsao, M. Senesky, and S. R. Sanders, “An integrated flywheel energy storage system with homopolar inductor motor/generator and high-frequency drive,” *IEEE Transactions on Industry Applications*, vol. 39, no. 6, pp. 1710–1725, Nov 2003.

[41] E. Severson, R. Nilssen, T. Undeland, and N. Mohan, “Magnetic equivalent circuit modeling of the ac homopolar machine for flywheel energy storage,” *IEEE Transactions on Energy Conversion*, vol. 30, no. 4, pp. 1670–1678, Dec 2015.

[42] M. Andriollo, F. Bortot, and A. Tortella, “Disc-type pm machine for the electromagnetic conversion/suspension of a flywheel system,” in *2015 International Conference on Renewable Energy Research and Applications (ICRERA)*, Nov 2015, pp. 739–744.

[43] C. Ye, J. Yang, F. Xiong, and Z. Q. Zhu, “Relationship between homopolar inductor machine and wound-field synchronous machine,” *IEEE Transactions on Industrial Electronics*, 2019, doi: 10.1109/TIE.2019.2898577.

[44] M. Garcia-Gracia, M. A. Cova, M. T. Villen, and A. Uson, “Novel modular and retractable permanent magnet motor/generator for flywheel applications with reduced iron losses in stand-by mode,” *IET Renewable Power Generation*, vol. 8, no. 5, pp. 551–557, July 2014.

[45] J. G. Bitterly and S. E. Bitterly, “Flywheel based energy storage system,” U.S. Patent 5 614 777, Mar. 1997.

[46] S. R. Holm, “Modeling and optimization of a permanent magnet machine in a flywheel,” Ph.D. dissertation, Technische Universiteit Delft, Delft, Nov 2003.

[47] T. D. Nguyen, K. Tseng, S. Zhang, and H. T. Nguyen, “A novel axial flux permanent-magnet machine for flywheel energy storage system: Design and analysis,” *IEEE Transactions on Industrial Electronics*, vol. 58, no. 9, pp. 3784–3794, Sep. 2011.

[48] J. eun Yi, K. W. Lee, B. Kim, J. Ko, S. Jeong, and M. D. Noh, *et al.*, “Micro-flywheel energy storage system with axial flux machine,” in *2007 IEEE/ASME international conference on advanced intelligent mechatronics*, Sep. 2007, pp. 1–6.

[49] Elektrisola, [Online]. Available: https://www.elektrisola.com/en/hf-litz-wire-litz/products/terminology-basics/selection-of-litz-wire -parameters.html.

[50] D. Gambetta and A. Ahfock, “Designing printed circuit stators for brushless permanent magnet motors,” *IET Electr. Power Appl.*, vol. 3, no. 5, pp. 482–490, 2009.

[51] N. S., S. P. Nikam, S. Singh, S. Pal, A. K. Wankhede, and B. G. Fernandes, “High-speed coreless axial-flux permanent-magnet motor with printed circuit board winding,” *IEEE Trans. Ind. Appl.*, vol. 55, no. 2, pp. 1954–1962, 2019.

[52] P. P. Silvester and R. L. Ferrari, *Finite Elements for Electrical Engineers.* Cambridge University Press, 1982.

[53] M. Rosu, P. Zhou, D. Lin, D. M. Ionel, M. Popescu, F. Blaabjerg, V. Rallabandi, and D. Staton, *Multiphysics Simulation by Design for Electrical Machines, Power Electronics and Drives.* Wiley-IEEE Press, 201.

[54] T. Guillod, J. Huber, F. Krismer, and J. W. Kolar, “Litz wire losses: Effects of twisting imperfections,” in *IEEE Workshop Contr. Modeling Power Electron. (COMPEL)*, 2017, pp. 1–8.

[55] C. R. Sullivan, “Computationally efficient winding loss calculation with multiple windings, arbitrary waveforms, and two-dimensional or three-dimensional field geometry,” *IEEE Trans. Power Electron.*, vol. 16, no. 1, pp. 142–150, 2001.

[56] X. Wang, W. Pang, P. Gao, and X. Zhao, “Electromagnetic design and analysis of axial flux permanent magnet generator with unequal-width PCB winding,” *IEEE Access*, vol. 7, pp. 164 696–164 707, 2019.

[57] A. Cavagnino, M. Lazzari, F. Profumo, and A. Tenconi, “A comparison between the axial flux and the radial flux structures for PM synchronous motors,” *IEEE Transactions on Industry Applications*, vol. 38, no. 6, pp. 1517–1524, Nov 2002.

[58] N. Taran, D. M. Ionel, and D. G. Dorrell, “Two-level surrogate-assisted differential evolution multi-objective optimization of electric machines using 3-D FEA,” *IEEE Trans. Magn.*, vol. 54, no. 11, pp. 1–5, Nov 2018.

[59] I. Boldea, L. Tutelea, and M. Topor, “Theoretical characterization of three phase flux reversal machine with rotor-pm flux concentration,” in *2012 13th International Conference on Optimization of Electrical and Electronic Equipment (OPTIM)*. IEEE, 2012, pp. 472–476.

[60] Y. Liu, H. Li, and Z. Zhu, “A high-power factor vernier machine with coil pitch of two slot pitches,” *IEEE Transactions on Magnetics*, vol. 54, no. 11, pp. 1–5, 2018.

[61] R. Zhang, J. Li, R. Qu, and D. Li, “Analysis and design of triple-rotor axial-flux spoke-array vernier permanent magnet machines,” *IEEE Transactions on Industry Applications*, vol. 54, no. 1, pp. 244–253, 2017.

[62] P. M. Tlali, R. Wang, and S. Gerber, "Comparison of PM vernier and conventional synchronous 15 kW wind generators," in *Proc. Int. Conf. Electr. Mach. (ICEM)*, Sep. 2018, pp. 2065–2071.

[63] R. Zhang, J. Li, R. Qu, and D. Li, "Analysis and design of triple-rotor axial-flux spoke-array vernier permanent magnet machines," *IEEE Trans. Ind. Appl.*, vol. 54, no. 1, pp. 244–253, Jan 2018.

[64] H. Fujinaka, "Brush-less motor using vernier structure," Patent US 7,064,468, Jun., 2006.

[65] F. Zhao, T. A. Lipo, and B. I. Kwon, "A novel dual-stator axial-flux spoke-type permanent magnet vernier machine for direct-drive applications," *IEEE Transactions on Magnetics*, vol. 50, no. 11, pp. 1–4, Nov 2014.

[66] D. Li, R. Qu, and T. A. Lipo, "High-power-factor vernier permanent-magnet machines," *IEEE Transactions on Industry Applications*, vol. 50, no. 6, pp. 3664–3674, Nov 2014.

[67] L. Xu, G. Liu, W. Zhao, X. Yang, and R. Cheng, "Hybrid stator design of fault-tolerant permanent-magnet vernier machines for direct-drive applications," *IEEE Transactions on Industrial Electronics*, vol. 64, no. 1, pp. 179–190, Jan 2017.

[68] K. Okada, N. Niguchi, and K. Hirata, "Analysis of a vernier motor with concentrated windings," *IEEE Transactions on Magnetics*, vol. 49, no. 5, pp. 2241–2244, May 2013.

[69] J. Li, K. T. Chau, J. Z. Jiang, C. Liu, and W. Li, "A new efficient permanent-magnet vernier machine for wind power generation," *IEEE Transactions on Magnetics*, vol. 46, no. 6, pp. 1475–1478, June 2010.

[70] D. Li, R. Qu, J. Li, L. Xiao, L. Wu, and W. Xu, "Analysis of torque capability and quality in vernier permanent-magnet machines," *IEEE Transactions on Industry Applications*, vol. 52, no. 1, pp. 125–135, Jan 2016.

[71] I. Boldea, L. Tutelea, and M. Topor, “Theoretical characterization of three phase flux reversal machine with rotor-pm flux concentration,” in *2012 13th International Conference on Optimization of Electrical and Electronic Equipment (OPTIM)*, May 2012, pp. 472–476.

[72] R. Zhang, J. Li, R. Qu, and D. Li, “Analysis and design of triple-rotor axial-flux spoke-array vernier permanent magnet machines,” *IEEE Transactions on Industry Applications*, vol. 54, no. 1, pp. 244–253, 2018.

[73] V. Rallabandi, N. Taran, D. M. Ionel, and I. G. Boldea, “Magnus—an ultra-high specific torque pm axial flux type motor with flux focusing and modulation,” in *2017 IEEE Energy Conversion Congress and Exposition (ECCE)*. IEEE, 2017, pp. 1234–1239.

[74] ——, “Axial-flux pm synchronous machines with air-gap profiling and very high ratio of spoke rotor poles to stator concentrated coils,” in *2017 IEEE International Electric Machines and Drives Conference (IEMDC)*. IEEE, 2017, pp. 1–7.

[75] I. Boldea, J. Zhang, and S. A. Nasar, “Theoretical characterization of flux reversal machine in low-speed servo drives-the pole-pm configuration,” *IEEE Transactions on Industry Applications*, vol. 38, no. 6, pp. 1549–1557, Nov 2002.

[76] J. Biela, M. Schweizer, S. Waffler, and J. W. Kolar, “SiC versus Si; evaluation of potentials for performance improvement of inverter and DC DC converter systems by SiC power semiconductors,” *IEEE Transactions on Industrial Electronics*, vol. 58, no. 7, pp. 2872–2882, July 2011.

[77] D. Li, R. Qu, and T. A. Lipo, “High-power-factor vernier permanent-magnet machines,” *IEEE transactions on industry applications*, vol. 50, no. 6, pp. 3664–3674, 2014.

[78] N. Taran, V. Rallabandi, G. Heins, and D. M. Ionel, “A comparative study of conventional and coreless axial flux permanent magnet synchronous motors for

solar cars," in *2017 IEEE International Electric Machines and Drives Conference (IEMDC).* IEEE, 2017, pp. 1–7.

[79] V. Rallabandi, P. Han, M. G. Kesgin, N. Taran, and D. M. Ionel, "Axial-field vernier-type flux modulation machines for low-speed direct-drive applications," in *Proc. IEEE Energy Convers. Congr. Expo. (ECCE)*, Sep. 2019, pp. 3123–3128.

[80] I. Boldea, L. Tutelea, and M. Topor, "Theoretical characterization of three phase flux reversal machine with rotor-pm flux concentration," in *2012 13th Int. Conf. Opt. of Electric. and Electron. Equipment (OPTIM)*, 2012, pp. 472–476.

[81] V. Rallabandi, N. Taran, D. M. Ionel, and I. G. Boldea, "MAGNUS — an ultra-high specific torque PM axial flux type motor with flux focusing and modulation," in *IEEE Energy Convers. Congr. Expo. (ECCE)*, 2017, pp. 1234–1239.

[82] "U.S. drive electrical and electronics technical team roadmap," Oct. 2017. [Online]. Available: https://www.energy.gov/eere/vehicles/downloads/us-drive-electrical-and-electronics-technical-team-roadmap

[83] I. Husain, B. Ozpineci, M. S. Islam, E. Gurpinar, G. J. Su, W. Yu, S. Chowdhury, L. Xue, D. Rahman, and R. Sahu, "Electric drive technology trends, challenges, and opportunities for future electric vehicles," *Proc. IEEE*, pp. 1–21, 2021.

[84] D. Ionel, J. Eastham, and T. Betzer, "Finite element analysis of a novel brushless dc motor with flux barriers," *IEEE Transactions on Magnetics*, vol. 31, no. 6, pp. 3749–3751, 1995.

[85] M. G. Kesgin, P. Han, D. Lawhorn, and D. M. Ionel, "Analysis of torque production in axial-flux vernier pm machines of the MAGNUS type," in *2021 IEEE International Electric Machines Drives Conference (IEMDC)*, 2021, pp. 1–5.

[86] A. Fatemi, D. M. Ionel, M. Popescu, Y. C. Chong, and N. A. O. Demerdash, "Design optimization of a high torque density spoke-type pm motor for a formula e race drive cycle," *IEEE Transactions on Industry Applications*, vol. 54, no. 5, pp. 4343–4354, 2018.

[87] S. Choi, M. S. Haque, M. T. B. Tarek, V. Mulpuri, Y. Duan, S. Das, V. Garg, D. M. Ionel, M. A. Masrur, B. Mirafzal, and H. A. Toliyat, "Fault diagnosis techniques for permanent magnet ac machine and drives—a review of current state of the art," *IEEE Trans. Transport. Electrif.*, vol. 4, no. 2, pp. 444–463, 2018.

[88] Y. Liao, F. Liang, and T. Lipo, "A novel permanent magnet motor with doubly salient structure," *IEEE Trans. Ind. Appl.*, vol. 31, no. 5, pp. 1069–1078, 1995.

[89] R. Deodhar, S. Andersson, I. Boldea, and T. Miller, "The flux-reversal machine: a new brushless doubly-salient permanent-magnet machine," *IEEE Trans. Ind. Appl.*, vol. 33, no. 4, pp. 925–934, 1997.

[90] A. S. Thomas, Z. Q. Zhu, R. L. Owen, G. W. Jewell, and D. Howe, "Multiphase flux-switching permanent-magnet brushless machine for aerospace application," *IEEE Trans. Ind. Appl.*, vol. 45, no. 6, pp. 1971–1981, 2009.

[91] T. Raminosoa, A. M. El-Refaie, D. Pan, K.-K. Huh, J. P. Alexander, K. Grace, S. Grubic, S. Galioto, P. B. Reddy, and X. Shen, "Reduced rare-earth flux-switching machines for traction applications," *IEEE Trans. Ind. Appl.*, vol. 51, no. 4, pp. 2959–2971, 2015.

[92] S. Ullah, S. McDonald, R. Martin, and G. Atkinson, "A permanent magnet assisted switched reluctance machine for more electric aircraft," in *Proc. Int. Conf. Electr. Mach. (ICEM)*, 2016, pp. 79–85.

[93] C. S. Goli, S. Essakiappan, P. Sahu, M. Manjrekar, and N. Shah, "Review of recent trends in design of traction inverters for electric vehicle applications," in *2021 IEEE 12th International Symposium on Power Electronics for Distributed Generation Systems (PEDG)*, 2021, pp. 1–6.

[94] C. J. Flynn, "Parallel magnetic circuit motor," U.S. Patent 20110089775 A1, Apr. 2011.

[95] ——, "Hybrid permanent magnet motor," U.S. Patent 7898135 B2, Mar. 2011.

[96] V. Rallabandi, P. Han, J. Wu, A. M. Cramer, D. M. Ionel, and P. Zhou, "Design optimization and comparison of direct-drive outer-rotor SRMs based on fast current profile estimation and transient FEA," *IEEE Trans. Ind. Appl.*, vol. 57, no. 1, pp. 236–245, 2021.

[97] N. Simpson, C. Tighe, and P. Mellor, "Design of high performance shaped profile windings for additive manufacture," in *IEEE Energy Convers. Congr. Expo. (ECCE)*, 2019, pp. 761–768.

[98] S. A. Semidey and J. R. Mayor, "Experimentation of an electric machine technology demonstrator incorporating direct winding heat exchangers," *IEEE Trans. Ind. Electron.*, vol. 61, no. 10, pp. 5771–5778, 2014.

Vita

Murat Gurhan Kesgin, PhD Candidate

Department of Electrical and Computer Engineering, University of Kentucky

Murat Gurhan Kesgin is a Ph.D. candidate in the SPARK Laboratory, Electrical and Computer Department at University of Kentucky (UK). He started his graduate studies at UK in 2015 on a scholarship supported by the Turkish Government and received his M.S. degree in Electrical Engineering in 2017 with research on the design and simulation of a photovoltaic-based charging station for electric vehicles. At UK, he has been working as a Research Assistant on multiple projects sponsored by NSF and industrial companies with emphasis on the large-scale design optimization of special electric machines for high-speed and low-speed direct drive applications. Murat received a Best Poster Paper Award at the 2019 IEEE International Conference on Renewable Energy Research and Applications (ICRERA) with a paper on axial-flux permanent-magnet machines for renewable energy storage flywheel systems. He was a selected speaker for memory session of Dr. Thomas Lipo in ECCE 2021. His current research focuses on advanced electromagnetic FEA, electric machines and power electronic drives, and design optimization.